

cy.1

**ARCHIVE COPY
DO NOT LOAN**



THE AFFDL-NIELSEN FLOW-FIELD STUDY

**VON KÁRMÁN GAS DYNAMICS FACILITY
ARNOLD ENGINEERING DEVELOPMENT CENTER
AIR FORCE SYSTEMS COMMAND
ARNOLD AIR FORCE STATION, TENNESSEE 37389**

April 1976

Final Report for Period June 25 – July 10, 1975

Approved for public release; distribution unlimited.

Proposed by: U. S. Air Force
AFRL-TR-76-0001

Prepared for

**AIR FORCE FLIGHT DYNAMICS LABORATORY (FXG)
WRIGHT-PATTERSON AFB, OHIO 45433**

AEDC TECHNICAL LIBRARY



5 0720 00063 3083

NOTICES

When U. S. Government drawings specifications, or other data are used for any purpose other than a definitely related Government procurement operation, the Government thereby incurs no responsibility nor any obligation whatsoever, and the fact that the Government may have formulated, furnished, or in any way supplied the said drawings, specifications, or other data, is not to be regarded by implication or otherwise, or in any manner licensing the holder or any other person or corporation, or conveying any rights or permission to manufacture, use, or sell any patented invention that may in any way be related thereto.

Qualified users may obtain copies of this report from the Defense Documentation Center.

References to named commercial products in this report are not to be considered in any sense as an endorsement of the product by the United States Air Force or the Government.

This report has been reviewed by the Information Office (OI) and is releasable to the National Technical Information Service (NTIS). At NTIS, it will be available to the general public, including foreign nations.

APPROVAL STATEMENT

This technical report has been reviewed and is approved for publication.

FOR THE COMMANDER



CARL J. SCHULZE
Major, USAF
Chief Air Force Test Director, VKF
Directorate of Test



CRAIG E. MAHAFFY
Colonel, USAF
Director of Test

ERRATA

AEDC-TR-76-18, April 1976
(UNCLASSIFIED REPORT)

THE AFFDL-NIELSEN FLOW-FIELD STUDY

W. T. Strike, Jr., Terry R. Penney, and
John H. Porter, ARO, Inc.

Arnold Engineering Development Center
Air Force Systems Command
Arnold Air Force Station, Tennessee

Uncertainties tabulations, bottom of page 8 and top of page 9, of subject report have been revised and are reproduced, respectively, on the reverse side of this page.

<u>Component</u>	<u>Balance Design Loads</u>	<u>Calibration Load Range</u>	<u>Range of Check Loads</u>	<u>Measurement Uncertainty</u>
Normal Force, lb	10	4	±2.5	±0.025
Pitching Moment,* in.-lb	20	10	±1.6	±0.050
Side Force, lb	10	4	±1.0	±0.025
Yawing Moment,* in.-lb	20	10	±0.6	±0.050
Rolling Moment, in.-lb	2.25	0.9	±0.45	±0.006
Axial Force, lb	6	3	0-1.5	±0.015

* About balance forward moment bridge

Absolute Uncertainty

Near Balance Minimum Load, ±, (Body Axes)

<u>M_∞</u>	<u>C_N</u>	<u>C_m</u>	<u>C_Y</u>	<u>C_n</u>	<u>C_l</u>	<u>C_A</u>	<u>C_{AT}</u>
1.51	0.010	0.028	0.010	0.028	0.006	0.016	0.006
2.01	0.010	0.028	0.010	0.028	0.006	0.016	0.006
2.50	0.010	0.028	0.010	0.028	0.006	0.016	0.006

UNCLASSIFIED

REPORT DOCUMENTATION PAGE		READ INSTRUCTIONS BEFORE COMPLETING FORM
1 REPORT NUMBER AEDC-TR-76-18	2 GOVT ACCESSION NO.	3 RECIPIENT'S CATALOG NUMBER
4 TITLE (and Subtitle) THE AFFDL-NIELSEN FLOW-FIELD STUDY		5 TYPE OF REPORT & PERIOD COVERED Final Report-June 25 - July 10, 1975
		6. PERFORMING ORG. REPORT NUMBER
7. AUTHOR(s) William T. Strike, Jr., Terry R. Penney, and John H. Porter, ARO, Inc.		8 CONTRACT OR GRANT NUMBER(s)
9 PERFORMING ORGANIZATION NAME AND ADDRESS Arnold Engineering Development Center (XO) Air Force Systems Command Arnold Air Force Station, Tennessee 37389		10 PROGRAM ELEMENT, PROJECT, TASK AREA & WORK UNIT NUMBERS Program Element 62201F Project 8219
11 CONTROLLING OFFICE NAME AND ADDRESS Air Force Flight Dynamics Laboratory (FXG) Wright-Patterson AFB, Ohio 45433		12. REPORT DATE April 1976
		13. NUMBER OF PAGES 87
14 MONITORING AGENCY NAME & ADDRESS (if different from Controlling Office)		15 SECURITY CLASS. (of this report) UNCLASSIFIED
		15a. DECLASSIFICATION/DOWNGRADING SCHEDULE N/A
16 DISTRIBUTION STATEMENT (of this Report) Approved for public release; distribution unlimited.		
17 DISTRIBUTION STATEMENT (of the abstract entered in Block 20, if different from Report) <i>1. Stores - Separation 2. Stores - Pressure distribution 3. " " Flow fields 4. Fuel tanks " " "</i>		
18 SUPPLEMENTARY NOTES Available in DDC		
19 KEY WORDS (Continue on reverse side if necessary and identify by block number) <div style="display: flex; justify-content: space-between;"> <div> flow fields test methods aircraft angles of attack </div> <div> velocity pressure Reynolds number Mach numbers </div> </div>		
20 ABSTRACT (Continue on reverse side if necessary and identify by block number) <p>This test was conducted in support of a program to develop a generalized analytical method for predicting the separation characteristics of stores from a high-speed aircraft (parent body). The tests were conducted in the von Kármán Gas Dynamics Facility (VKF), Tunnel A, at nominal Mach numbers of 1.5, 1.76, 2.0, and 2.5 at a nominal free-stream Reynolds number of</p>		

UNCLASSIFIED

UNCLASSIFIED

20. ABSTRACT (Continued)

4×10^6 per foot. The test program involved three phases, namely flow-field surveys using a cone probe rake to determine local flow-field angles and velocity, pressure distributions on the store as it separated from a parent body, and six-component force and moment data on the store. The tests were conducted at angles of attack of zero and five degrees. This document contains a detailed description of the calibration procedure for the 20-deg half-angle cone probes and the method used to evaluate the local flow-field properties from the cone probe surface pressure and pitot pressure measurements. Also included is a comparison of integrated pressure data with the force and moment data obtained on the storebody by a balance.

UNCLASSIFIED

PREFACE

The work presented herein was conducted by the Arnold Engineering Development Center (AEDC), Air Force Systems Command (AFSC), for the Nielsen Engineering and Research, Inc., Mountain View, California, at the request of the Air Force Flight Dynamics Laboratory (AFFDL/AFSC), Wright-Patterson Air Force Base, under Program Element 62201F. The test results were obtained by ARO, Inc. (a subsidiary of Sverdrup & Parcel and Associates, Inc.), contract operator of AEDC, AFSC, Arnold Air Force Station, Tennessee. The test program was conducted under ARO Project number V41A-B4A, and the final data package was completed September 10, 1975. The authors of this report were William T. Strike, Jr., Terry R. Penney, and John H. Porter, ARO, Inc. The manuscript (ARO Control No. ARO-VKF-TR-75-164) was submitted for publication on November 19, 1975.

The authors would like to express their appreciation for the engineering support provided by R. H. Burt and J. T. Best, the theoretical results provided by Dr. A. W. Mayne and E. O. Marchand, and the programming of the data reduction requirements provided by J. L. Roberson and G. R. Cook which greatly accelerated our evaluation of the test results.

CONTENTS

	<u>Page</u>
1.0 INTRODUCTION	5
2.0 APPARATUS	
2.1 Wind Tunnel	5
2.2 Flow-Field Probes and Models	6
2.3 Instrumentation and Data Uncertainties	6
2.4 Data Reduction Procedures	9
3.0 TEST PROCEDURES	
3.1 Test Conditions	12
3.2 Test Procedure	14
4.0 RESULTS	
4.1 Flow-Field Probe Calibration	15
4.2 Flow-Field Surveys	20
4.3 Storebody Pressure and Force Data	22
5.0 SUMMARY OF RESULTS	25
REFERENCES	25

ILLUSTRATIONS

Figure

1. Model Installations	27
2. Flow-Field Probe	28
3. Installation Photographs	29
4. Pressure Distribution Model	32
5. Ogive-Cylinder Force and Moment Storebodies	33
6. Wing/Fuselage Parent Model	34
7. Coordinate System Showing Positive Vector Directions	35
8. Mach Number Calibration of Flow-Field Probes, $Re/ft = 4 \times 10^6$	36
9. Total Angle-of-Attack Effect on the Uncorrected Indicated Cone Probe Mach Number at $M_\infty = 2.5$	37
10. Total Angle-of-Attack Correction on the Indicated Cone Probe Mach Number at $M_\infty = 2.5$	38
11. Cone Probe Calibration for Flow Angularity (Probe No. 1)	39
12. Summary of the Linear Flow Angularity Factor (η/\bar{p}) for a 20-deg Half-Angle Cone as a Function of Free-Stream Mach Number	40
13. The Residual Error in the Flow-Field Angularity Computation Based on a Linear Calibration Factor, η/\bar{p}	41

<u>Figure</u>	<u>Page</u>
14. Reduced Residual Error in the Flow-Field Angularity Computation Containing a Correction for Nonlinearity in the Calibration Factor	42
15. Final Residual Error in the Present Flow-Field Angularity Computations with All Corrections Incorporated in the Calibration	43
16. Comparison of the Present Empty Tunnel Flow-Field Survey Results with Tunnel A Calibration Data	44
17. Comparison of Flow-Field Survey Data Obtained at $M_\infty = 2$ Over Similar Parent Bodies	45
18. Local Flow-Field Properties over the Parent Body without Pylons, $\alpha = 0$, $M_\infty = 1.5$, $Re/ft = 4 \times 10^6$	46
19. Local Flow-Field Properties over the Parent Body with the Pylon Attached, $\alpha = 0$, $M_\infty = 1.5$, $Re/ft = 4 \times 10^6$	49
20. Local Flow-Field Properties over the Parent Body with the Pylon Attached, $\alpha = 5$ deg, $M_\infty = 1.5$, $Re/ft = 4 \times 10^6$	52
21. Example of Free-Stream Mach Number Effects on the Local Flow-Field Properties over the Parent Body with the Pylon Attached, $\alpha = 0$, $\Delta z = 0$	55
22. Storebody Pressure Distributions, $\alpha = 0$	58
23. Uncertainties in the Integrated Forebody Pressure Drag Coefficients (Isolated Storebody at $\alpha = 0$, $M_\infty = 1.5$ and 2.5)	59
24. Local Aerodynamic Loading on the Store Center Pylon Station, $\Delta y = 0$, $\alpha = 0$, $M_\infty = 1.5$, $Re/ft = 4 \times 10^6$	60
25. Free-Stream Mach Number Effects on the Local Aerodynamic Loading of the Store in the Presence of the Parent Body with the Center Pylon, $\alpha = 0$, $\Delta y = 0$, $\Delta z = 0.47$ in.	62
26. Comparison of Isolated Storebody Force and Integrated Pressure Data ($Re/ft = 4 \times 10^6$)	63
27. Comparison of Force/Moment Data, Integrated Surface Pressure Data, and Predicted Static Stability and Axial-Force Coefficients of the Isolated Storebody	66
28. Variation of the Storebody Static Stability Coefficients with Vertical Displacement from the Parent Body with and without the Pylon at $\alpha = 0$, $M_\infty = 1.5$, $Re/ft = 4 \times 10^6$	67
29. Variation of the Storebody Static Stability Coefficients with Vertical Displacement from the Parent Body with and without the Pylon at $\alpha = 5$ deg, $M_\infty = 1.5$, $Re/ft = 4 \times 10^6$	73
30. Mach Number Effects on the Variation of the Storebody (SLFN) Static Stability Coefficients with Vertical Displacement from the Parent Body with the Pylon, $\alpha = 0$, $Re/ft = 4 \times 10^6$	79
NOMENCLATURE	85

1.0 INTRODUCTION

This investigation was conducted in the von Kármán Gas Dynamics Facility (VKF) Supersonic Wind Tunnel (A) for Nielsen Engineering and Research, Inc. (NEAR) who is under contract with the Air Force Flight Dynamics Laboratory (AFFDL/FXG) for the development of a generalized, theoretical method for predicting separation characteristics of stores from high-speed aircraft.

Three types of data were obtained in the interference flow field of a generalized aircraft shape with and without pylons. The test program was divided into three phases which consisted of (1) flow field surveys, using a cone probe rake to determine the local velocity field; (2) pressure distributions on a store model; and (3) force and moment data on a store model. In addition, free-stream (interference-free) data were obtained with the probe rake and on the force and pressure store models.

The probe rake was calibrated at nominal Mach numbers of 1.5, 1.76, 2.0 and 2.5. The major portion of the test program was accomplished at Mach numbers 1.5, 2.0, and 2.5 at a nominal Reynolds number of 4 million per foot and at parent-body angles of attack of 0 and 5 deg.

This report contains a discussion of the data reduction, an analysis of the flow-field probe calibration data, and a brief evaluation of a selected sample of the test results. A complete analysis and publication of the test results will be forthcoming from Nielsen Engineering and Research, Inc., Mountain View, California.

2.0 APPARATUS

2.1 WIND TUNNEL

Tunnel A is a continuous, closed-circuit, variable density wind tunnel with an automatically driven flexible-plate-type nozzle and a 40- by 40-in. test section. The tunnel can be operated at Mach numbers from 1.5 to 6 at maximum stagnation pressures from 29 to 200 psia, respectively, and stagnation temperatures up to 750°R ($M_{\infty} = 6$). Minimum operating pressures range from about one-tenth to one-twentieth of the maximum at each Mach number. The tunnel is equipped with a model injection system which allows removal of the model from the test section while the tunnel remains in operation.

2.2 FLOW-FIELD PROBES AND MODELS

The model installations used in each phase of the test program are shown in Fig. 1. The sector-supported parent body remained the same for each phase. The parent-aircraft model, installed in an inverted position on the main strut support system, consisted of a symmetrical swept-wing and fuselage combination with pylon locations on the fuselage centerline and at the 1/3- and 2/3-wing-semispan stations. The store models were two-caliber tangent ogive cylinders and were tested with and without fins during the force phase. The store models and the flow-field probe rake were all supported from the VKF Captive Trajectory System (CTS).

A three-probe rake was used to obtain the flow-field survey data. The three conical probes with 20-deg semi-apex angles were spaced 1.5 in. apart in the vertical plane. There were four static pressure orifices on the surface of each cone (equally spaced 90 deg apart) and a total-pressure orifice at the apex of the cone. Details and dimensions of the probe are shown in Fig. 2, and model installation photographs of the probe with the parent body are presented in Figs. 3a and 3b. The installation of the pressure model (phase II) on the CTS in a stored position on the 2/3-pylon wing station of the parent body is shown in Fig. 3c. Details and dimensions of the pressure model including the location of the pressure taps are shown in Fig. 4. One pressure tap was located in the model nose to provide a pitot pressure measurement. The finless (S_{LFN}) force model, which was identical to the pressure model (except that the pressure model nose was slightly blunted by the presence of the pitot pressure tap), is shown in Fig. 5 along with the fin (S_{LFF}) force model.

Details and dimensions of the parent-aircraft model are given in Fig. 6. The fuselage consisted of a tangent ogival nose section, a cylindrical center section, and a truncated tail cone. The wing had an NACA65A006 airfoil section with the quarter-chord line swept 45 deg, an aspect ratio of 4, and a taper ratio of 0.3. Coordinates of the parent body and airfoil sections are tabulated in Fig. 6.

The model had provisions for mounting pylons at the fuselage centerline and on the left wing at the 1/3- and 2/3-wing semispan stations. Details of the pylons are included in Fig. 6. The pylons were identical except for the contour of the pylon-aircraft contact surface. Touch wires (electrical grounding system) on the pylons provided a location reference check between the store model and the pylon surface.

2.3 INSTRUMENTATION AND DATA UNCERTAINTIES

Tunnel A stilling chamber pressure was measured with a 15- or a 60-psid transducer referenced to a near vacuum. Based on periodic comparisons with secondary standards,

the uncertainty (a two-standard deviation bandwidth which includes 95 percent of the residuals) of these transducers is estimated to be within ± 0.2 percent of reading or ± 0.015 psia, whichever is greater. Stilling chamber temperature is measured with a copper-constantan thermocouple with an uncertainty of $\pm 3^\circ\text{F}$ based on repeat calibrations.

These uncertainties in the basic tunnel parameters, p_o and T_o , and the two-sigma variation in Mach number distribution determined from test section flow calibrations were used to estimate uncertainties in the other free-stream properties, using the Taylor series method of error propagation.

Test Conditions

Uncertainty (\pm), percent						
M_∞	M_∞	p_o	T_o	p_∞	q_∞	Re/ft
1.505	1.3	0.2	0.5	2.9	0.3	0.8
1.756	1.1	↓	↓	3.0	0.8	1.0
2.005	1.0	↓	↓	↓	1.1	1.1
2.503	0.8	↓	↓	↓	1.5	1.3

The cone probe and model pressures were measured with 15-psid transducers with a variable reference. The variable reference was also measured with another 15-psid transducer referenced to a near vacuum. These transducers were calibrated daily over a range of 0.3 to 12.0 psia using an air dead weight tester. Least squares straight line curve fits through these data points were used in determining a single scale factor for the 15-psid range of each transducer. The measurement precision is estimated to be 0.05 percent of reading.

This uncertainty in the pressure measurements was used to estimate the corresponding uncertainty that may exist in the cone probe calibration data and in the flow-field survey results presented in this report. The Taylor series method of error propagation was used in this analysis.

Model Pressures

Uncertainty (\pm), percent				
M_∞	p	p/p_∞	p'_o	p/p'_o
1.51	0.05	3.0	0.1	0.3
1.76	↓	↓	↓	0.3
2.01	↓	↓	↓	0.4
2.50	↓	↓	↓	0.5

Local Mach Number Evaluations

Uncertainty (\pm), absolute

<u>M_∞</u>	<u>\bar{p}/p_o'</u>	<u>M_θ</u>
1.51	0.0012	0.004
1.76	0.0012	0.006
2.01	0.0012	0.006
2.50	0.0026	0.026

Flow Angularity Parameters

Uncertainty (\pm), absolute

<u>M_∞</u>	<u>$\Delta p_{1,3}/\bar{p}$ and $\Delta p_{2,4}/\bar{p}$</u>	<u>η/\bar{p}</u>	<u>$\sigma_\theta, a_\theta,$ deg</u>
1.51	0.003	0.0003	0.2
1.76	0.003	0.0004	
2.01	0.004	0.0005	
2.50	0.006	0.0007	

Model forces and moments were measured with a six-component, moment type, strain-gage balance (PWT 6-40-010-40M-G) calibrated by VKF. Prior to the test, static loads in each plane and combined static loads were applied to the balance to simulate the range of loads and center of pressure locations anticipated during the test. The following uncertainties represent the bands which enclose 95 percent of the measured residuals, based on differences between the applied loads and the corresponding values calculated from the balance calibration equations included in the final data reduction.

<u>Component</u>	<u>Balance Design Loads</u>	<u>Calibration Load Range</u>	<u>Range of Check Loads</u>	<u>Measurement Uncertainty</u>
Normal force, lb	10	4	± 2.5	± 0.050
Pitching moment,* in.-lb	20	10	± 1.6	± 0.100
Side force, lb	10	4	± 1.0	± 0.050
Yawing moment,* in.-lb	20	10	± 0.6	± 0.100
Rolling moment, in.-lb	2.25	0.9	± 0.45	± 0.011
Axial force, lb	6	3	0-1.5	± 0.03

*About balance forward moment bridge

The transfer distance from the balance forward moment bridge to the model moment reference location was measured to an estimated precision of ± 0.005 in.

The balance and base pressure uncertainties were combined with uncertainties in the tunnel parameters, using the Taylor series method of error propagation, to estimate the uncertainty of the aerodynamic coefficients which are presented below.

Absolute Uncertainty (\pm)

M_∞	C_N	C_m	C_Y	C_n	C_l	C_A	C_{AT}
1.51	0.0012	0.007	0.0012	0.007	0.004	0.0055	0.0019
2.01	0.0012	0.013	0.0012	0.006	0.003	0.0043	0.0019
2.50	0.0013	0.010	0.0013	0.006	0.003	0.0034	0.0021

The CTS six degrees of freedom are sensed by potentiometers and read by a multiplexed analog-to-digital converter. The uncertainty in these measurements are summarized below. This estimate was made using the uncertainties quoted for each degree of freedom and the equations of motion.

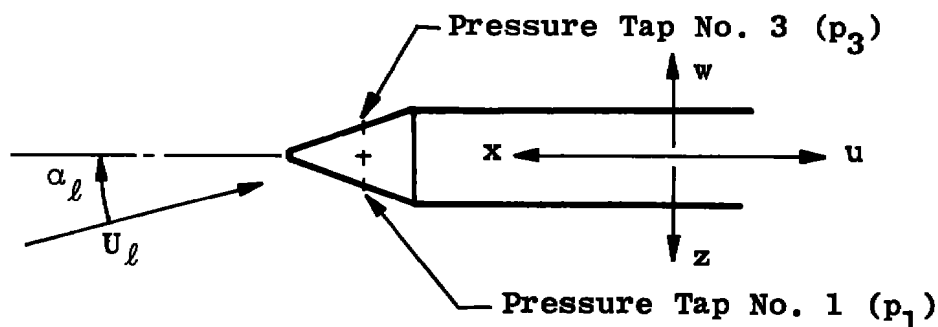
CTS Attitude and Position Uncertainties

<u>Motion</u>	<u>Drive System Uncertainty</u>	<u>Model Attitude and Position Uncertainty</u>
x	± 0.005 in.	± 0.050 in.
y	—	± 0.080 in.
z	± 0.005 in.	± 0.060 in.
α_{CTS}	± 0.05 deg	± 0.10 deg
ψ_{CTS}^*	± 0.10 deg	± 0.10 deg
η_{CTS}	± 0.03 deg	—

*The yaw angles ψ_{CTS} and η_{CTS} are used to obtain both yaw angle and lateral displacement.

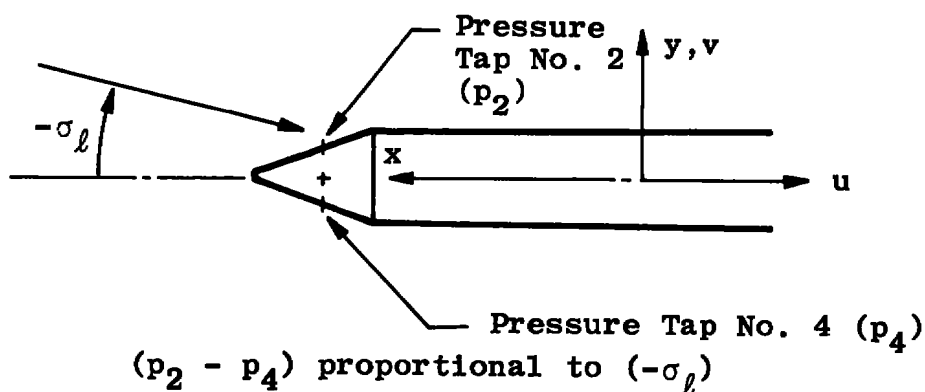
2.4 DATA REDUCTION PROCEDURES

The probe calibrations were conducted such that a positive pressure differential across the probe in the pitch plane corresponded to a positive local flow angle as indicated below.



Flow-Field Coordinates in the Pitch (Downwash) Plane

In the yaw plane, the probe calibrations were performed so that a positive pressure differential across the probe in the yaw plane occurred with the probe yawed in the negative direction or with a negative local sidewash angle as shown below.



Flow-Field Coordinates in Yaw (Sidewash) Plane

A complete description of the data reduction employed to deduce the local Mach number and flow-field angle from the cone probe calibration data is presented in Section 4.1.

The numerical scheme employed to evaluate the local loading coefficients on the storebody from the model surface pressure data is summarized below so that the local and resultant loading coefficients presented in the figures of this report are clearly defined. At each point in the test grid consisting of a fixed angle of attack and position in the flow field, the storebody was rolled 360 deg in 10-deg increments while surface pressure

data along one ray of the storebody was recorded. These pressure data were integrated as a function of roll angle to define the local force and moment coefficients per unit length (per inch).

The local normal-force coefficient and the local pitching-moment coefficient attributed to the normal force loading per inch at model station x_n is

$$c_{N_n} = -K \int_{-\pi}^{\pi} (p/p_{\infty})_n r_n \cos \phi d\phi \quad (1)$$

where

$$K = 2/(\gamma\pi M_{\infty}^2 r_b^2)$$

$$cm_n = -c_{N_n} (x_n - 3.188)/(2r_b) \quad (2)$$

Similarly, the local side-force and yawing-moment coefficients per inch were defined as follows:

$$C_{Y_n} = -K \int_{-\pi}^{\pi} (p/p_{\infty})_n r_n \sin \phi d\phi \quad (3)$$

and

$$c_{\eta_n} = -c_{Y_n} (x_n - 3.188)/(2r_b) \quad (4)$$

The local axial-force coefficient per unit length of the storebody (i.e., per inch) was defined as follows:

$$c_A = k \int_{-\pi}^{\pi} (p/p_{\infty} - 1)_n (r_n \tan \delta_n) d\phi \quad (5)$$

where r_n is the local storebody radius and δ_n the local slope of the storebody contour.

The resultant aerodynamic coefficients were evaluated as follows:

$$C_n = \int_0^{\ell} c_{N_n} dx_n \quad (6)$$

$$C_m = \int_0^{\ell} cm_n dx_n - \int_0^{1.5} r_n \tan \delta_n c_{N_n} dx_n / (2r_b) \quad (7)$$

The second integral term used in evaluating the pitching-moment coefficient corresponds to the moment produced by the axial-force component of the surface loading on the storebody.

$$C_Y = \int_0^{\ell} c_{Y_n} dx_n \quad (8)$$

$$C_{\eta} = \int_0^{\ell} c_{\eta n} dx_n - \int_0^{1.5} r_n \tan \delta_n c_{\gamma n} dx_n / (2r_b) \quad (9)$$

The resultant pressure drag coefficient of the storebody is defined as follows:

$$C_{Ap} = \int_0^{1.5} c_{An} dx_n \quad (10)$$

The numerical procedure for evaluating these integrals consisted of curve fitting three consecutive points in the distribution with a quadratic expression and then integrating this expression to define the magnitude of the integrant between two of the three consecutive points in the distribution. These integrants were then summed to ultimately define a particular coefficient.

3.0 PROCEDURE

3.1 TEST CONDITIONS

The test was conducted at Mach numbers 1.5, 1.76, 2.0, and 2.5. The free-stream Reynolds number was nominally 4 million per foot. A summary of the test conditions at each Mach number is given below.

<u>M_∞</u>	<u>p_o, psia</u>	<u>T_o, °F</u>	<u>q_∞, psia</u>	<u>p_∞, psia</u>	<u>Re/ft x 10⁻⁶</u>
1.5	13.8	100	5.9	3.7	3.9
1.76*	14.9	↓	6.0	2.8	↓
2.0	16.4	↓	5.9	2.1	↓
2.5	20.9	↓	5.4	1.2	↓

*Probe calibrations only.

As previously noted, the test program was conducted in three phases. The first phase consisted of calibration of the cone probes and then using these probes to define the variation in local stream velocity and flow direction in the vicinity of the pylons on the parent body. The probe calibrations covered a range of combined angles of attack and yaw from -10 to 10 deg. A summary of the flow-field survey data is given below.

Flow-Field Survey Data
at Mach No. 1.5, 2.0, and 2.5

Pylon Attached

z, in./ y, in.	Center Pylon			1/3-Station Pylon			2/3-Station Pylon		
	0.5	0	-0.5	-3.5	-4.0	-4.5	-7.5	-8.0	-8.5
3.58	x	x	x	x	x	x	x	x	x
2.83	x	x	x	x	x	x	x	x	x
Pylon Removed									
3.58	—	x	—	—	x	x*	—	x	—
2.83	—	x	—	—	x	x*	—	x	—

*This condition was not run at Mach number 2.0.

Flow-field surveys were also made in the absence of the parent body to define the undisturbed flow conditions existing in the tunnel region occupied by the models.

The second phase of the test program consisted of obtaining pressure distributions on the storebody without fins. The third phase consisted of measuring the forces and moments on the finless store. A summary of test phases II and III is given below.

Pressure and Force Test Schedule
Mach Number 1.5, 2.0, and 2.5
Pylon Attached and Removed
($\alpha = 0$ and 5 deg)

z, in.	Center Pylon	1/3-Station Pylon	2/3-Station Pylon
0	P	P	P*
0.37	P	P	P*
0.75	P	P	P*
0 to 45	F	F	F

*No pressure data were obtained with the pylon removed at Mach number 1.5 at this pylon station.

"P" represents data obtained with the pressure model, while "F" represents data obtained with the finless force model.

The finless storebody pressure and force models were also tested at Mach numbers 1.5, 2.0, and 2.5 at angles of attack up to 10 deg in the free-stream flow (parent body removed). Some store force data with fins attached were also obtained at Mach number 1.5, at the center pylon, and 1/3-pylon stations.

3.2 TEST PROCEDURE

Two separate and independent systems were used to support the models during the test. The parent model was inverted in the test section with a coordinate system as shown in Fig. 7 and supported on an offset sting and strut attached to the tunnel pitch support (see Fig. 1). Although the parent model had several pitch adjustments available, only the 0- and 5-deg parent angles of attack were tested. The flow-field probes and the storebody pressure and force models were supported on the CTS. The standard CTS grid program was used for data acquisition and model attitude positioning.

The VKF-CTS is a six-degree-of-freedom model support system with electromechanical drive units. The axial and vertical movements are obtained with linear drive units while lateral movement is obtained by rotating the roll-pitch-yaw support arm about the vertical support axis of the CTS and compensating the resulting yaw position with counter rotation of a forward yaw joint. Pitch motions are obtained through a forward knuckle joint which is oriented 90 deg from the forward yaw knuckle joint. The most forward component of the CTS is the roll mechanism capable of rolling ± 180 deg. The translational and rotational envelopes and rates of travel of the CTS drives in Tunnel A are as follows:

Nominal CTS Motion Capabilities in Tunnel A*

Motion	Travel Limits	Maximum Rate of Travel***
Axial (x)	40 in.	1 in./sec
Vertical (z)	± 15 in.**	1 in./sec
Lateral (y)	± 15 in.**	2 in./sec
Pitch (α) _{CTS}	± 14.8 deg	10 deg/sec
Yaw (ψ) _{CTS}	± 30 deg	10 deg/sec
Roll (ϕ) _{CTS}	± 180 deg	20 deg/sec

*All travel limits are set up as a function of model size, sting geometry, and model center of rotation.

**Measured from tunnel centerline.

***Rates are continuously variable up to the rates shown above.

The CTS was used to position the stores and probe rake relative to the parent aircraft through a prescribed grid matrix. Each grid was selected and loaded into the VKF CDC 1604B computer and the positioning of the store model was controlled by the computer which automatically recorded all the data inputs at each grid point location. At the start of each grid, the store model or probe was driven to a "touch point" (electrical contact point between the CTS model and the parent-body pylon). The CTS model was then moved to an initial starting position using the CTS drive system, and the resulting displacement between the initial starting position and the "touch point" were optically checked. In all cases, the reference check fell within the CTS positioning uncertainty. During all tests, the probe rake and store models were aligned parallel with the parent-body axes.

Model flow-field photographs were obtained on several configurations at selected model attitudes and test conditions. Numerous shadowgraphs, still photographs, and color schlieren movies were taken to assist in evaluating the effects of flow-field shocks on the aerodynamic loading imposed on the store model.

4.0 RESULTS

4.1 FLOW-FIELD PROBE CALIBRATION

As noted previously (Section 2.2), the flow-field probes consisted of 20-deg half-angle cones mounted on a cylindrical shaft. Four static pressure taps were located in a plane 0.165 in. from the cone nose at intervals of 90 deg around the circumference of the cone (see Fig. 2). The second-order approximations for relating cone surface pressure to cone total angle of attack as formulated in the Zdenek Kopal tables (Ref. 1) provide the following relationship for cone surface pressures.

$$p = \bar{p} - a_T \eta \cos \phi + a_T^2 (\bar{P}_0 + \bar{P}_2 \cos 2\phi) \quad (11)$$

The perturbation parameters η , \bar{P}_0 and \bar{P}_2 are assumed to be independent of the cone angle of attack and roll position and only a function of the cone angle (θ) and the local stream Mach number (M_∞) approaching the cone. Since the actual cone angles (θ) cannot be measured precisely and since the cones were blunted by the addition of a pitot pressure tap, a probe calibration was required. The cone nose bluntness ratio was nominally 0.07 (cone nose diameter to base diameter). The interpretation of the cone probe calibration was based on the previous relationship (Eq. (11)).

The following formulations were used to define the cone parameters η/\bar{p} and the average cone static pressure, \bar{p} , at zero angle of attack. (Note, at $a_T = 0$, theoretically $p = \bar{p}$.) The pressure taps were numbered consecutively around the cone as shown in sketches of Section 2.4. At angle of attack, the cone surface pressure at the n^{th} tap can be analytically defined as

$$p_n = \bar{p} - a_T \eta \cos(\phi + \phi_n) + a_T^2 (\bar{P}_0 + \bar{P}_2 \cos 2(\phi + \phi_n)) \quad (12)$$

The sum of the four static pressure measurements would theoretically yield the following result:

$$\bar{p} = \left(\frac{1}{4}\right) \sum_{n=1}^4 p_n \quad (13)$$

Therefore, at angle of attack, the average of these four cone surface pressure taps provides an estimate of the cone surface pressure at zero angle of attack. This average cone surface pressure, \bar{p} , and the pitot pressure (p_5) were used to calculate the local Mach number. A comparison of the experimental and analytically defined relationship of the average free-stream Mach number values (from tunnel calibrations) as a function of \bar{p}/p'_0 is shown in Fig. 8. In general, the measured average cone surface pressure ratio was greater than the predicted value by one to two percent. A curve fit of the experimental data provided the following relationship for defining the local stream Mach number upstream of the cone in terms of the pressure ratio \bar{p}/p'_0 .

$$\text{Mach Number Coefficient, } A$$

$$M_Q = \sqrt{1 + \left(\sum_{n=0}^5 A_n (\bar{p}/p'_0)^n \right)^{-3}} \quad (14)$$

	<u>Probe No. 1</u>	<u>Probe Nos. 2 and 3</u>
A ₀	3.35933	2.57318
A ₁	-47.9986	-37.6524
A ₂	293.596	241.392
A ₃	-835.398	-709.356
A ₄	1142.53	997.148
A ₅	-600.20	-536.021

In the Mach number range from about 1.4 to 3.0, there was good agreement between the data and this semi-empirical curve fit (Fig. 8). Outside this Mach number range, the curve fit was unreliable.

The results in Fig. 9 for $M_\infty = 2.5$ show that the Mach number calibration, that is, the average cone surface pressure ratio, was influenced by the cone probe angle of attack, and particularly at this Mach number. At the other free-stream Mach numbers, not shown, the angle-of-attack effect on the average cone surface pressures, \bar{p} , resulted in a nominal variation of 0.02 in the indicated cone probe Mach number over the total angle-of-attack range of ± 15 deg.

An iteration scheme was employed to correct this angle-of-attack effect on the cone probe indication of the local stream Mach number, M_ℓ .

$$M_\ell = M_\ell (\text{initial value}) / (1 - \Delta M) \quad (15a)$$

$$\Delta M = m \cdot a_T^{1.7} \quad (15b)$$

where

$$m = -1.5118 \times 10^{-4} + 2.0946 \times 10^{-5} M_\ell^{3.5} \quad (15c)$$

The correction produced by this iteration is shown by comparing Fig. 9 with Fig. 10 for $M_\infty = 2.5$ where the maximum error occurred. Although not shown, at the lower free-stream Mach numbers ($M \leq 2.0$), the angle-of-attack effect, after this correction was made, was nominally less than 0.01 in Mach number.

The probe total pitch angle (resultant flow angle) can be related to the cone surface pressure differentials in the following manner.

$$\Delta p_{1,3} = p_1 - p_3 = -2a_T \eta \cos \phi \quad (16a)$$

$$\Delta p_{2,4} = p_2 - p_4 = 2a_T \eta \sin \phi \quad (16b)$$

In general, the effective roll position (ϕ) of the probe was not zero, because the probe was calibrated by pitching the probes through an angle-of-attack range at various constant angles of yaw (ψ).

$$\phi = \tan^{-1} (-\tan \psi / \tan \alpha) + 90 (1 - \tan \alpha / |\tan \alpha|) \quad (17)$$

and the total angle of attack was defined as follows:

$$a_T = \tan^{-1} \sqrt{\tan^2 \alpha + \tan^2 \psi} \quad (18)$$

Actually, the value of the roll angle (ϕ) was not required to define the linearity factor, η , relating cone pressure differential $\Delta p_{1,3}$ or $\Delta p_{2,4}$ to a_T near $a_T = 0$.

$$\eta/\bar{p} = \left\{ \sqrt{(\Delta p_{1,3}/\bar{p})^2 + (\Delta p_{2,4}/\bar{p})^2} / (2 a_T) \right\}_{a_T \cong 0} \quad (19)$$

The linear characteristics of this flow-field calibration of local flow angle as a function of the square root of the sum of the squares of the pressure differentials, hereafter designated as DPSQ, is shown in Fig. 11 for probe No. 1 at $M_\infty = 1.5$ and 2.5. Similar results were obtained for the other two probes and at other Mach numbers. The linear portion of this relationship near $a_T = 0$ defines the value η/\bar{p} and it is evident (Fig.

11) that the relationship is nonlinear at the higher angles of attack. The factor η/\bar{p} is presented as a function of the free-stream Mach number in Fig. 12 and in general the experimental values fell four to six percent below the predicted values for a 20-deg sharp nose cone.

A curve fit of the experimental values of η/\bar{p} , as a function of the local stream Mach number (in this case M_∞) was defined as follows:

$$\eta/\bar{p} = \sum_{n=0}^3 E_n M_\infty^{5n/3} \quad (20)$$

where

$$E_0 = -1.5944 \times 10^{-3}$$

$$E_1 = 11.4102 \times 10^{-3}$$

$$E_2 = -0.56243 \times 10^{-3}$$

As seen in Fig. 12, this empirical expression provides a good fit of the data and is considered satisfactory over the Mach number range from about $M_\infty = 1.25$ to 3.5.

The nonlinearity at the higher total angles of attack of the differential pressure term noted in Fig. 11 is again clearly shown in Fig. 13 which is a plot of the error in the indicated probe angle of attack based on the linear factor $\bar{\eta}/p$ versus the actual angle of attack of the probe. The error in the indicated angle of attack is about 1.6 deg at a nominal total angle of attack of 12 deg at Mach number 1.5. The magnitude of this error in the indicated probe angle diminished with increasing free-stream Mach number.

An empirical correction was formulated from the experimental data to account for this nonlinearity. The form of the correction is as follows:

$$\Delta\alpha \text{ (DPSQ)} = c \cdot |\text{DPSQ}|^{2.5} \quad (21)$$

where

$$c = 318.5 \text{ Mg}^{-5}$$

This correction reduced the error in the indicated cone probe angle of attack to less than ± 0.4 deg as is shown in Fig. 14.

A second correction to the indicated probe angle of attack was formulated as a function of indicated probe roll angle. This correction was deduced by plotting $\Delta\alpha_T''$ of Fig. 14 as a function of the probe roll angle. This correction has the form given by Eq. (22),

$$\Delta a(\phi) = \sum_{n=0}^5 C_n (\cos \phi)^n \quad (22)$$

Coefficients

$$\begin{aligned} C_0 &= 0.0640565 & C_3 &= -0.970705 \\ C_1 &= -0.256300 & C_4 &= 0.211107 \\ C_2 &= -0.197904 & C_5 &= 1.45475 \end{aligned}$$

The resulting error in the computed cone probe angle of attack for probe No. 1 at each calibrated free-stream Mach number is shown in Fig. 15. In most cases of combined cone probe pitch and yaw, the indicated cone probe total angle (resultant flow angle) based on $\Delta p_{1,2}$ and $\Delta p_{2,4}$ agreed to within ± 0.2 deg. As noted previously, a Taylor series error propagation analysis has indicated that the error in measuring the cone surface pressure differential could cause an error of ± 0.2 deg in flow angle (see Section 2.3).

Finally, a correction had to be made to the cone probes calculated local pitch and yaw angles to account for the misalignment of each cone nose axis with the probe axis (i.e., the axis of the cylindrical shaft supporting the instrumented cone nose, which could be aligned accurately with the tunnel axes). The cone probe tips were very small, and it was believed that any misalignment of the probe nose could not be accurately assessed with conventional physical measurements. Therefore, the misalignment of the cone nose was deduced from the probe calibration data. The calibration data obtained at all Mach numbers was examined and an average angle (Δa_m or $\Delta \psi_m$) was selected which would most consistently shift the pressure differential curves ($\Delta p_{1,3}/\bar{p}$ vs α or $\Delta p_{2,4}/\bar{p}$ vs ψ) so that a zero angle occurred when the pressure differential was zero. Although the local tunnel flow angularity is different for each Mach number and the probe misalignment is independent of Mach number, this use of the probe calibration data obtained at all Mach numbers provided the best estimate of the probable probe misalignment. The results of this evaluation are summarized as follows:

Estimated Probe Misalignment

Probe No.	Δa_m , deg	$\Delta \psi_m$, deg
1	-0.63	0.60
2	-0.20	-0.43
3	-0.38	0.09

The procedure adopted for calculating local flow angles involved first an evaluation of the total roll angle and angle of attack sensed by the cone probe. Two corrections defined earlier were made to the total angle of attack as indicated in Eq. (23).

$$a_T = (1/2)(DPSQ)/(\eta/p) - \Delta a(DPSQ) - \Delta a(\phi) \quad (23)$$

where

$$\phi = \tan^{-1} \left(\frac{-\Delta p_{1,2}}{\Delta p_{1,3}} \right) + 90 \left(1 - \frac{|\Delta p_{1,3}|}{\Delta p_{1,3}} \right)$$

The corrected angle of attack was used to evaluate the local downwash and sidewash angles (α_l and σ_l , respectively) corrected for the probe misalignment in pitch and yaw. That is

$$\alpha_l = \tan^{-1} (\tan a_T \cdot \cos \phi + \Delta a_m) \quad (24)$$

$$\sigma_l = \tan^{-1} (\tan a_T \cdot \sin \phi + \Delta \psi_m) \quad (25)$$

At this point, the total angle of attack and roll were reevaluated in terms of the corrected downwash and sidewash angles. These corrected total angles of attack, a_T , and roll, ϕ , were then used to evaluate the local stream velocities as follows:

$$u/U_\infty = U_l/U_\infty \cos a_T \quad (26a)$$

$$w/U_\infty = U_l/U_\infty \sin a_T \cos \phi \quad (26b)$$

and

$$v/U_\infty = U_l/U_\infty \sin a_T \sin \phi. \quad (26c)$$

where

$$U_l/U_\infty = M_l/M_\infty (\sqrt{T_l/T_\infty}) \quad (27)$$

and

$$T_l/T_\infty = (1 + 0.2M_\infty^2)/(1 + 0.2M_l^2)$$

4.2 FLOW-FIELD SURVEYS

Cone probe rake surveys were made in the tunnel test section, with the parent body removed, at lateral (y) positions corresponding to each of the pylon stations on the parent body. The surveys made along the tunnel centerline at $z = 0.6$ at $M_\infty = 2.0$ and 2.5 are presented in Fig. 16 and compared with results from previous tunnel calibration data

for $z = 0$. The existing tunnel flow angle data were obtained with 3.1-in.-diam, 30-deg, half-angle cone probes and the Mach numbers were computed from the ratio of probe pitot to tunnel stilling chamber pressure. Considering that the survey probe Mach numbers were based on the average cone surface pressure ratioed to the cone pitot pressure, the difference in the probe sizes, and the difference in the vertical (z) location of the two sets of data there is good agreement between the tunnel calibration data and the survey probe data. The favorable comparison of flow-field results such as those presented in Fig. 16 provides assurance that the present cone probe calibration and data reduction procedures were acceptable.

In general, the flow-field angularity variations from the survey probe in the pitch plane were approximately ± 0.3 deg at Mach number 1.5 and decreased to about ± 0.2 deg at Mach numbers 2.0 and 2.5. The flow-field angularity in the yaw plane was significantly smaller at all test Mach numbers.

A comparison of the stream properties (local Mach number and flow angularity) obtained in this test with results from Ref. 2 which used a similar parent body is presented in Fig. 17. The parent bodies in both tests had identical wing geometry but slightly different center bodies. In the earlier tests (Ref. 2), the center body was longer and smaller in diameter than the present parent body. In spite of these differences, the agreement between the two data sets is very good. Apparently, the local flow field produced by the wing at this outboard wing station of 6.6 in. is not greatly influenced by the relatively small difference in the fuselage body geometry.

Examples of the type of flow-field data obtained in this study are presented in Figs. 18 through 21. Most of the results presented were obtained at a free-stream Mach number of 1.5. In these figures, both the survey probes and the parent body were at zero angle of attack. The abscissa (x) in these figures represents the distance downstream from the parent-body nose and (z) represents the vertical distance of the survey probe centerline from a horizontal (x, y) plane passing through the axis of the parent body (see Fig. 7).

The local stream properties over the parent center body and wing surfaces without pylons at $\alpha = 0$ are shown in Fig. 18. Figure 18a shows that the flow in the lateral plane along the centerline pylon location as reflected by the sidewash angle, σ_2 , was fairly uniform and nominally 0.3 deg or less. At the 1/3- and 2/3-wing pylon station, the flow-field distribution has the classical form reflecting the abrupt compression then expansion over the wing to the trailing-edge shock or compression wave, where the flow abruptly returns toward the free-stream condition. The overall length of these "N-shaped pressure wave" signatures depends primarily on the length of the wing chord, the local compression angle at wing leading-edge surface, and the vertical (z) displacement of the

survey from the wing chord. Also, a comparison of Figs. 18b and c shows an overall steeper signature (greater expansion) at the outboard 2/3- wing station than at the 1/3-wing station.

The effects on the local flow-field properties of adding pylons to the parent body at $\alpha = 0$ are shown in Fig. 19. The 2.66-in.-long pylons produced disturbances that are clearly seen when compared to data in Fig. 18. The addition of the pylons did not, however, grossly affect the sidewash angle distribution. A comparison of the sidewash angle distributions of Figs. 18 and 19 shows that on the average the distributions were nominally within one degree of each other.

The local stream properties over the parent body with pylons at the centerline location only, at 5-deg angle of attack, are shown in Fig. 20. It should be noted again that the survey probes were at 5-deg angle of attack along an axis parallel to the parent-body axes. A comparison of these results with those of Fig. 19b shows that angle of attack affects primarily the local downwash angles.

The effects of varying free-stream Mach number on the flow field over the parent body with pylons, at $\alpha = 0$, are shown in Fig. 21. In general, these data show, as expected, that parent-body flow-field disturbances are displaced further downstream as Mach number increases. This is clearly seen in the wing leading-edge shock location in the surveys over the wing but is not so evident in the centerline station survey. As a matter of interest, therefore, the location of the disturbances from the wing leading-edge body juncture was estimated (using the assumption of a Mach wave propagation downstream) and is shown on the M_∞ plot of Fig. 21a. The location of this disturbance was also identified and confirmed by schlieren photographs of the flow field. The location of the wing leading-edge shock disturbances in Figs. 21b and 21c indicates that the shock wave at Mach number 1.5 was most likely detached.

4.3 STOREBODY PRESSURE AND FORCE RESULTS

The zero angle-of-attack storebody surface pressure distributions presented in Fig. 22 were obtained with the parent body removed. The data at Mach numbers 2.0 and 2.5 are compared to the predicted distribution based on an analysis described in Ref. 3. There was about a five-percent difference between the predicted and experimental results. The analysis of Ref. 3 could not be used to predict the pressure distribution of the Mach number 1.5 condition because the programmed analysis is only valid for supersonic speeds, and the local stream velocity over the storebody at the nose was subsonic.

These free-stream pressure distributions were integrated circumferentially to determine the local pressure drag coefficient distributions (i.e., C_{A_p} versus x) and these are shown

in Fig. 23 for Mach numbers 1.5 and 2.5 along with the integrated total drag coefficient C_{Ap} . The results from the programmed numerical integration scheme previously described in Section 2.4 are compared in this figure with both local and total drag coefficients obtained from a graphical technique involving the fairing of the experimental data following theoretical distribution shown previously in Fig. 22. As noted in the figure, the graphical integration technique gave total pressure drag coefficients C_{Ap} which were six percent higher. At Mach number 2.5, the theoretical pressure drag coefficient (Ref. 3) was five percent below the programmed numerical integration value.

The influence of the parent-body flow field on the local aerodynamic loading of the store over the center pylon station is shown in Figs. 24 and 25. These results were selected to illustrate pylon and Mach number effects.

The results in Fig. 24 for $M_\infty = 1.5$ show the downstream movement of the local normal-force loading patterns with increase in separation distance between the store and parent body, and the significant increase in the normal-force loading distribution produced by the presence of the pylon. Although the flow field should be symmetrical in the lateral plane, a small side-force loading distribution was obtained, but this loading was not influenced to any extent by either separation distance or the addition of the pylons.

Free-stream Mach number effects on the interference loading on the storebody are illustrated in Fig. 25. The distributions of c_y versus x/l again indicate some asymmetry in the local flow field over the center section of the parent body at Mach numbers 1.5 and 2.0. The local flow-field surveys (shown in Fig. 21) also showed that the sidewash angles were greater at these two Mach numbers.

A comparison of the integrated pressure data and the measured forces and moments on the isolated storebody at several angles of attack is shown in Fig. 26. Except for the pitching-moment coefficients obtained at high angles of attack at Mach numbers 2.0 and 2.5, there was good agreement between the integrated pressure data and the static stability data from the force model. The integrated pressure drag coefficient, C_{Ap} , fell significantly below the forebody axial-force coefficient, C_A , from the force model. The difference between C_A and C_{Ap} could be accounted for by the addition of a friction drag increment as noted below.

A summary of the free-stream integrated pressure data and the force/moment data as a function of free-stream Mach number is given in Fig. 27. The predicted variations in $C_{N,a}$, $(C_{m,a}/C_{N,a})$ and C_{Ap} with Mach number estimated from the USAF Stability and Control Datacom (Ref. 4), and the pressure drag coefficient as predicted by the analysis of Ref. 3 for Mach numbers 1.76 and 2.5 are included in the figure. The stability parameters

are in reasonable agreement with predicted values considering the estimated measurement uncertainties. The agreement between integrated pressure values and force model data is very good. The pressure drag coefficient is also in good agreement with the inviscid analysis of Ref. 3. The difference between C_{Ap} and C_A can be accounted for by a skin-friction drag coefficient produced by assuming a laminar boundary-layer flow over the first two-thirds of the body and a turbulent flow over the remaining length. Fully turbulent boundary-layer flow over the entire body would produce a friction drag coefficient of nearly 0.10 which is 43 percent greater than the difference between C_A and C_{Ap} at Mach number 2.0.

The variation in the store static stability and axial-force coefficients as the store was displaced from the parent body is shown in Figs. 28, 29, and 30. The integrated pressure static stability coefficients of the finless store are included in these figures as solid symbols and, as will be seen, compare well with the force data. Also, for clarity, a solid line is faired through the results obtained with the pylons on. It should be noted that during these Δz traverses only the pylon at the traverse location was attached to the parent body. Also, the midpoint of the store remained in line with the vertical centerline of the pylon.

The results in Fig. 28 for $M_\infty = 1.5$ and $\alpha = 0$ show, in general, that the addition of the pylon and the addition of fins to the store increased the overall variation of the storebody normal-force and pitching-moment coefficient with displacement distance. At the center pylon station (Fig. 28a) the small asymmetry in the flow field, noted earlier, is evident in the lateral plane coefficients, particularly on the store with fins. The addition of fins to the storebody more than doubled the forebody axial-force coefficient which showed only small variation with separation distance.

At the 1/3- and 2/3-pylon wing stations (Figs. 28b and c), the store side-force and yawing-moment coefficients were significant, particularly when the store was in close proximity to the parent body. On the store with fins, the rolling-moment variation generally decreased with separation distance. At the wing pylon stations, there was a marked decrease in C_A with separation distance increase.

Similar results for the store and parent body at 5-deg angle of attack are shown in Fig. 29. At the center body location, the aerodynamic coefficients of the store models approached the characteristics of the isolated store (at 5-deg angle of attack) because at $\Delta z = 5$ in. the store had penetrated the nose shock from the parent body. At the pylon wing stations, the store was still under the influence of the parent-body flow field at the maximum Δz position.

Free-stream Mach number effects on the aerodynamic characteristics of the finless store during separation from the parent body are illustrated in Fig. 30. An increase in free-stream Mach number generally tended to decrease the overall variation in the aerodynamic coefficients with displacement distance.

5.0 SUMMARY OF RESULTS

An investigation was conducted to obtain experimental data to aid in the development of a generalized theoretical method for predicting separation characteristics of stores from high-speed aircraft. The tests were made at Mach numbers 1.5, 2.0, and 2.5 at parent and store model angles of attack of zero and 5 deg, and at a nominal Reynolds number of 4 million per foot. Results of the test are summarized as follows:

1. The 20-deg cone probe Mach number calibration results agree to within two percent with sharp cone theory.
2. The final residual errors in the flow-field angularity measurements are within ± 0.2 deg at all free-stream Mach numbers from 1.5 to 2.5.
3. The cone static probe calibration results are in reasonable agreement with previous Tunnel A calibration data.
4. The store pressure distribution results show good agreement with inviscid theory.
5. In general, the normal-force and pitching-moment coefficients resulting from the integrated pressure data on the storebody agreed with results from the force and moment balance data.
6. Differences between the integrated pressure drag coefficient, C_{Ap} , and the drag coefficient C_A from the force tests can be accounted for by a skin-friction drag increment based on turbulent boundary-layer flow over the aft one-third of the store.

6.0 REFERENCES

1. Staff of the Computing Section Center of Analysis (Under the Direction of Zdenek Kopal). "Tables of Supersonic Flow Around Yawing Cones." MIT TR 3, 1947; and "Tables of Supersonic Flow Around Cones of Large Yaw." MIT TR 5, 1949, Massachusetts Institute of Technology, Cambridge, Massachusetts.

2. Carlson, H. W. "Measurements of Flow Properties in the Vicinity of Three Wing-Fuselage Combinations at Mach Numbers of 1.61 and 2.01." NASA TM X-64, October 1959.
3. Inouye, M., Rakich, J. V., and Lomax, H. "A Description of Numerical Methods and Computer Programs for Two-Dimensional and Axisymmetric Supersonic Flow Over Blunt-Nosed and Flared Bodies." NASA TN D-2970, Ames Research Center, Moffett Field, California, August 1965.
4. USAF Stability and Control Datcom. Prepared by McDonnell Douglas Corporation, Douglas Aircraft Division, under Contract F33615-74-C-3021, January 1975, (Revised).

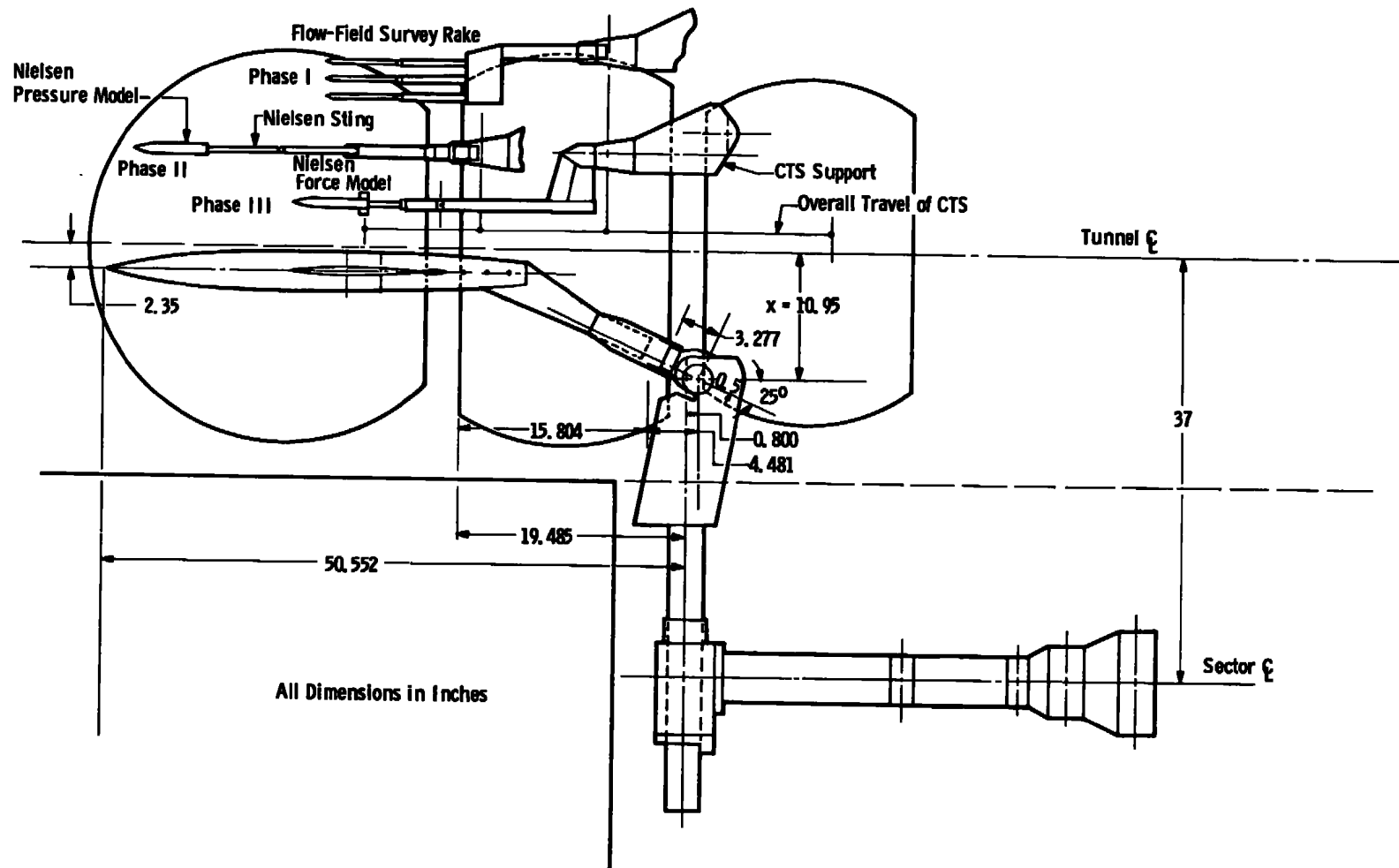


Figure 1. Model installations.

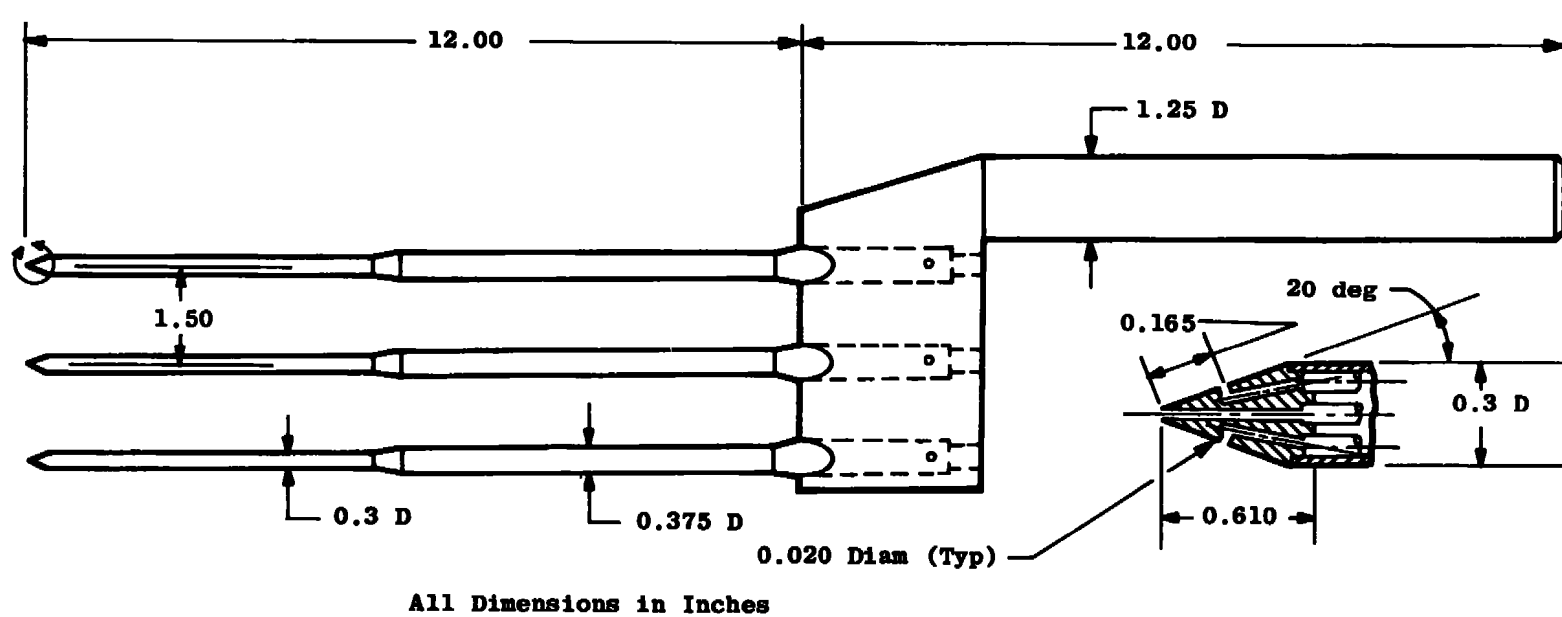
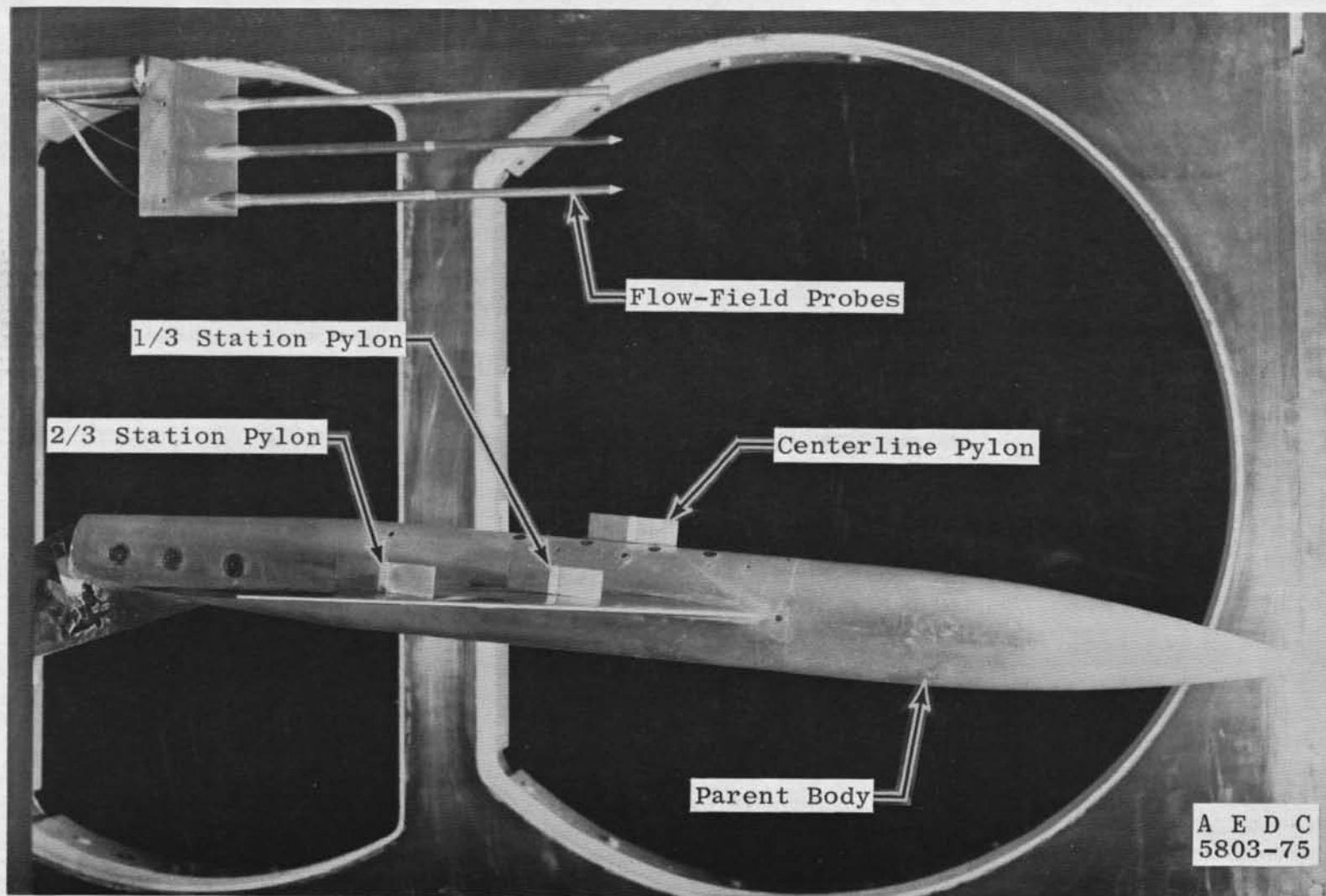
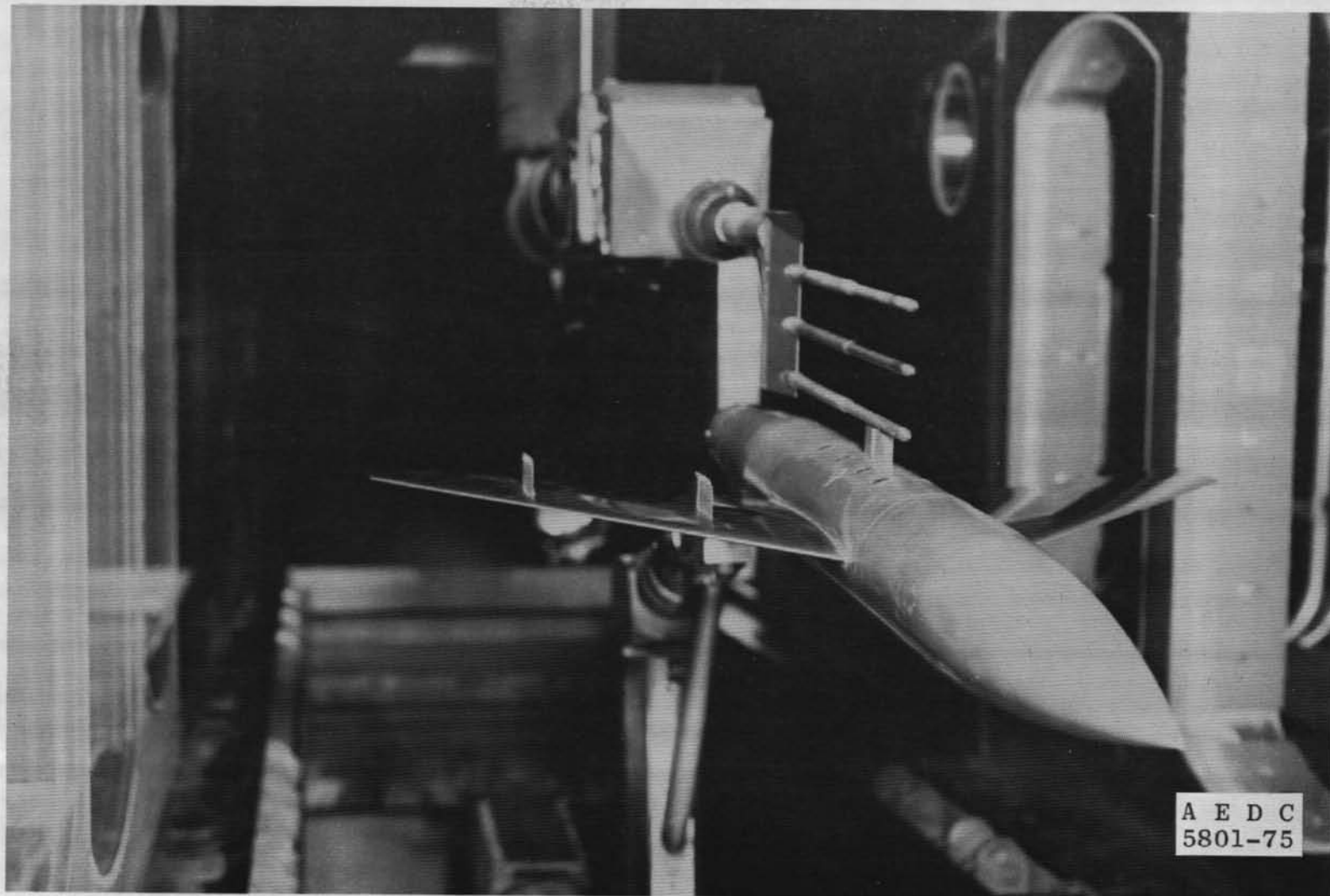


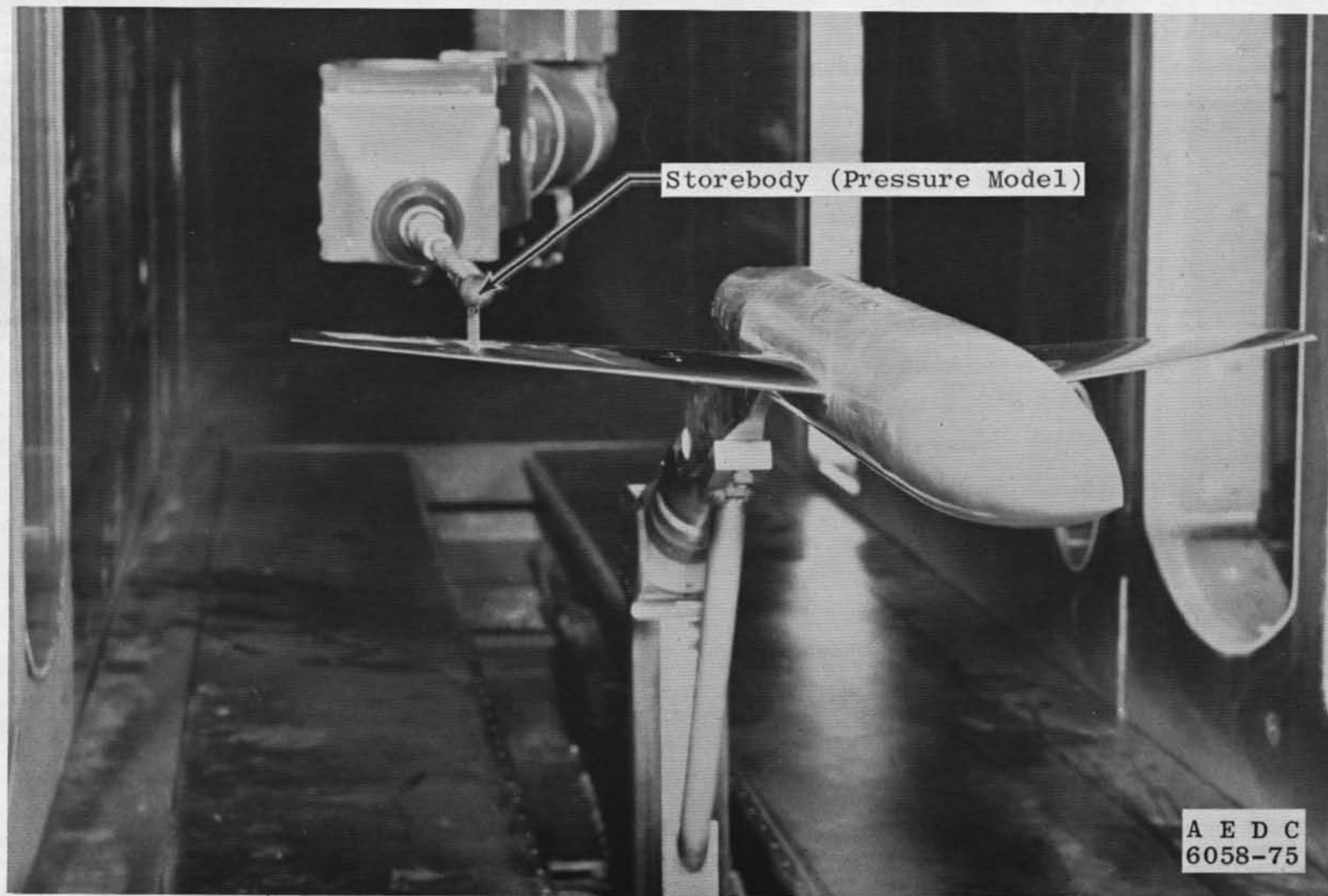
Figure 2. Flow-field probe.



a. Flow-field probes and parent body
Figure 3. Installation photographs.



b. Flow field probes on parent body centerline pylon station
Figure 3. Continued.



c. Pressure model on parent body 2/3-pylon station
Figure 3. Concluded.

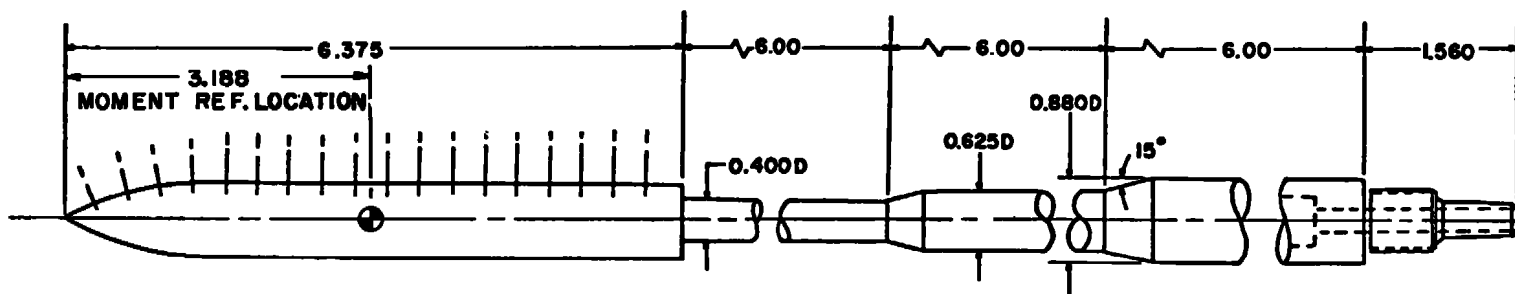
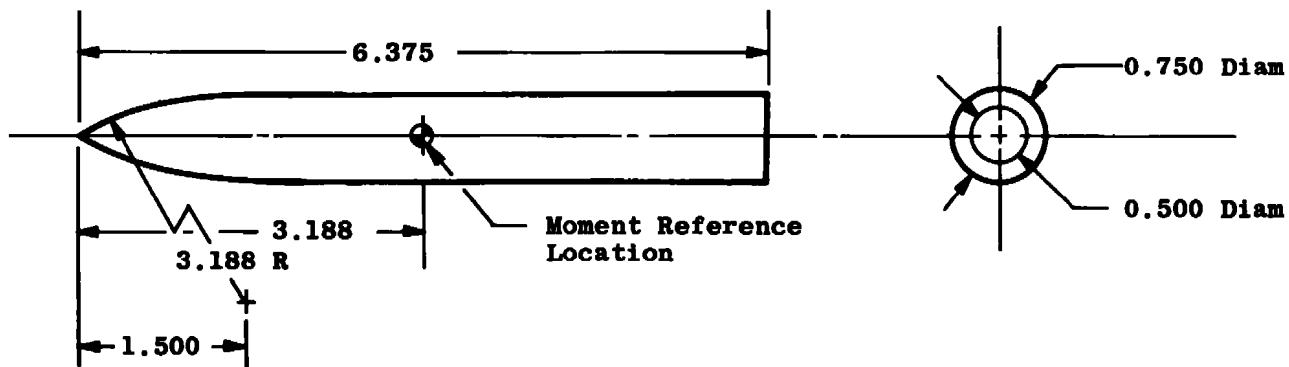
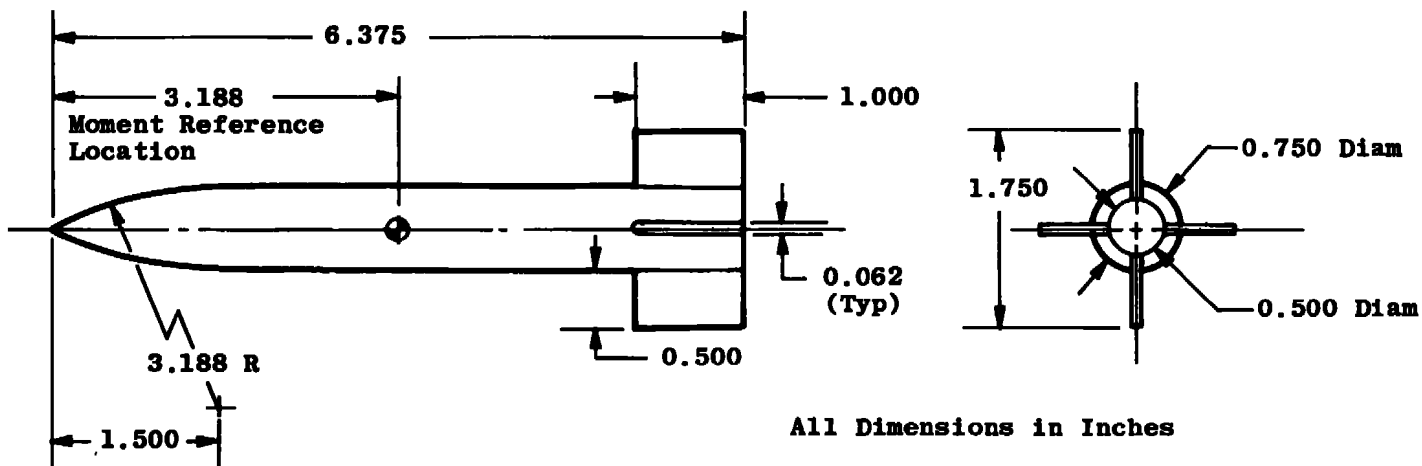


Figure 4. Pressure distribution model.



a. $S_{L FN}$, finless configuration



All Dimensions in Inches

b. $S_{L FF}$, finned configuration

Figure 5. Ogive-cylinder force and moment storebodies.

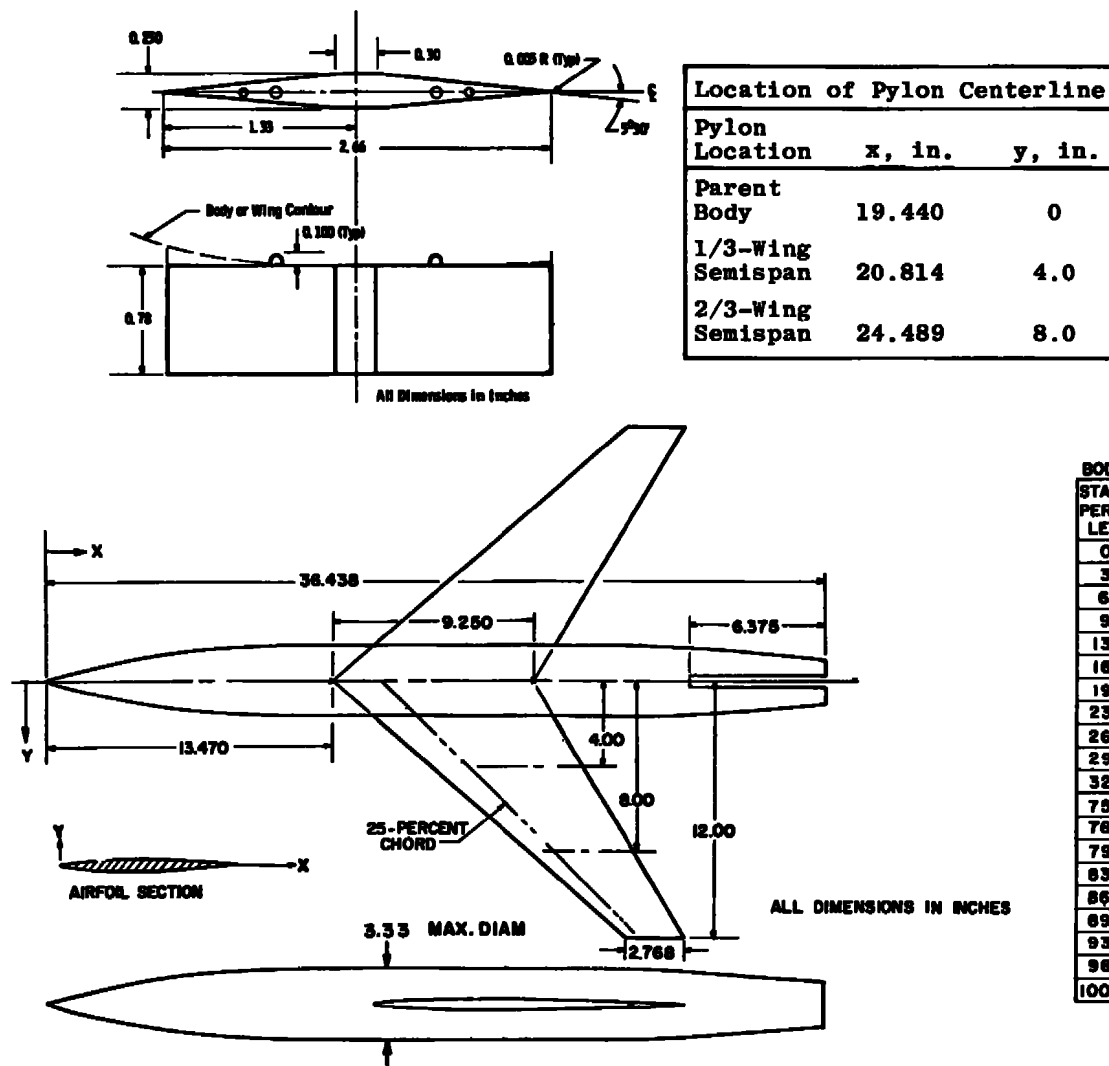


Figure 6. Wing/fuselage parent model.

BODY COORDINATES

STATION PERCENT LENGTH	RADIUS PERCENT LENGTH
0.00	0.00
3.28	0.91
6.57	1.71
9.86	2.41
13.15	3.00
16.43	3.50
19.72	3.90
23.01	4.21
26.29	4.43
29.58	4.53
32.00	4.57
75.34	4.57
76.69	4.54
79.98	4.38
83.26	4.18
86.55	3.95
89.84	3.72
93.13	3.49
96.41	3.26
100.00	3.02

AIRFOIL COORDINATES

X, % CHORD SEE SEC.	Y, % CHORD SEE SEC.
0.00	0.000
0.50	0.464
0.75	0.563
1.25	0.718
2.50	0.981
5.00	1.313
7.50	1.591
10.00	1.824
15.00	2.194
20.00	2.474
25.00	2.687
30.00	2.842
35.00	2.945
40.00	2.998
45.00	2.992
50.00	2.925
55.00	2.793
60.00	2.602
65.00	2.364
70.00	2.087
75.00	1.775
80.00	1.437
85.00	1.083
90.00	0.727
95.00	0.370
100.00	0.013
L.E. RADIUS 0.229% CHD.	
T.E. RADIUS 0.014% CHD.	

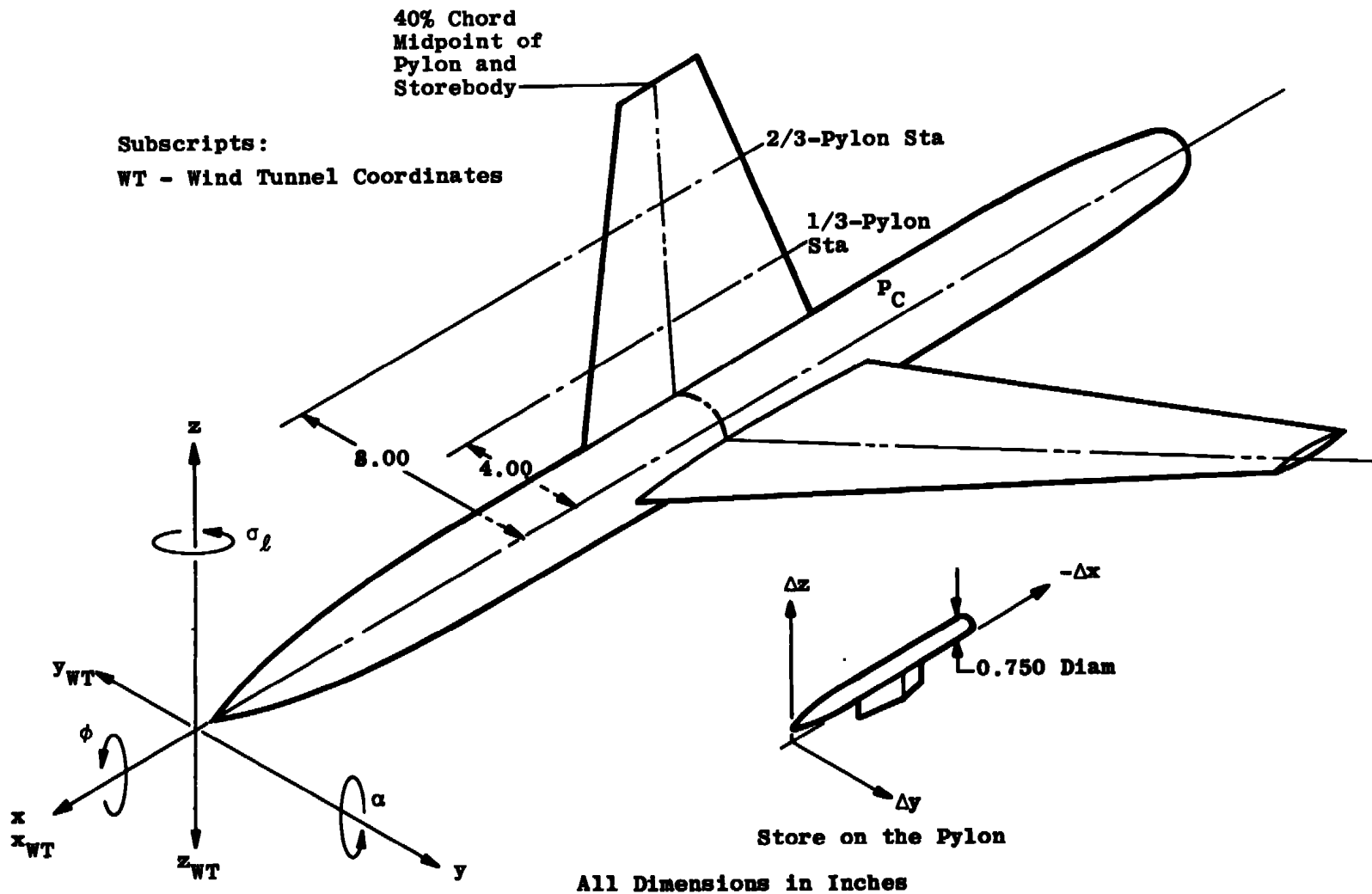


Figure 7. Coordinate system showing positive vector directions.

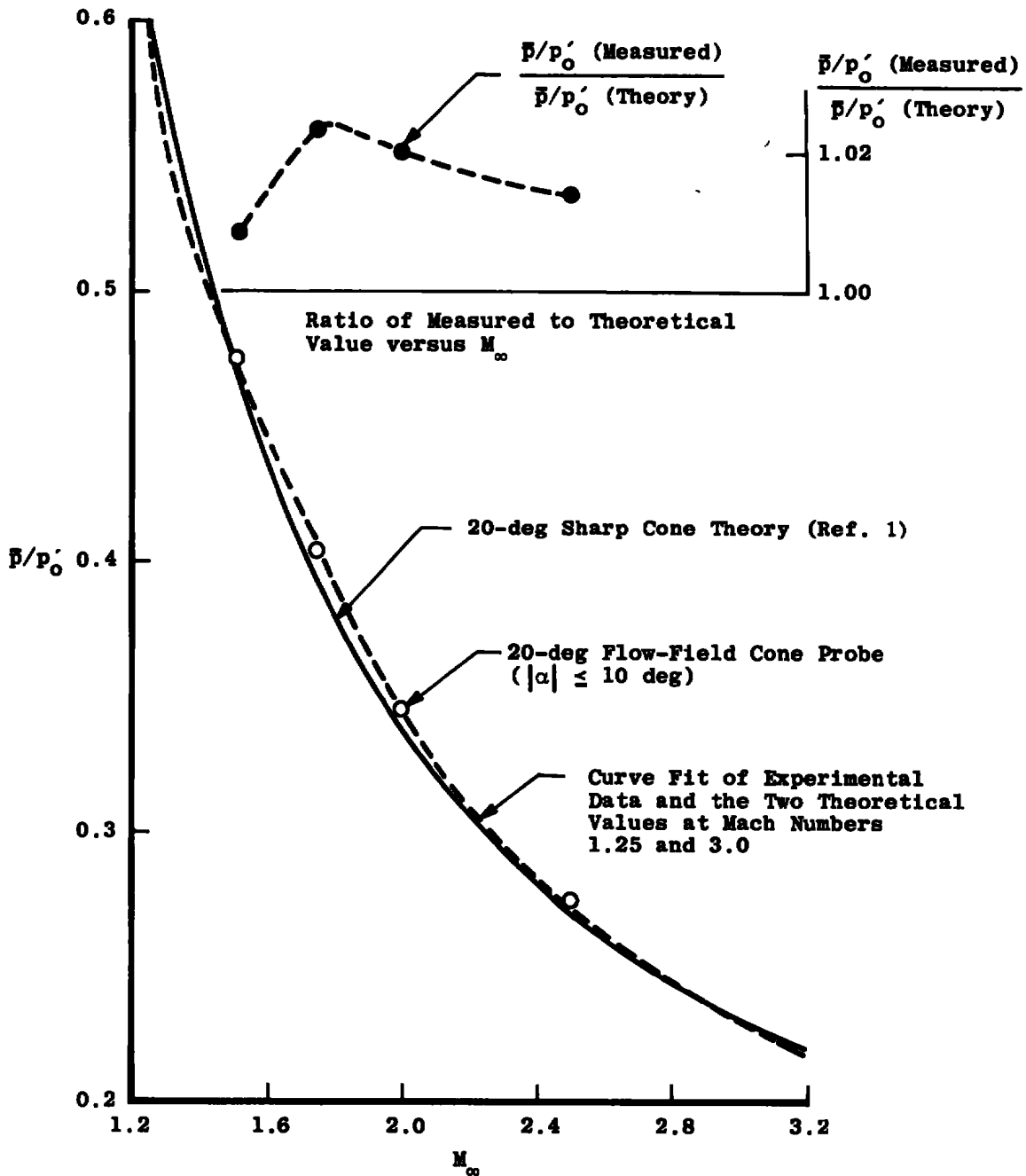


Figure 8. Mach number calibration of flow-field probes, $Re/ft = 4 \times 10^6$.

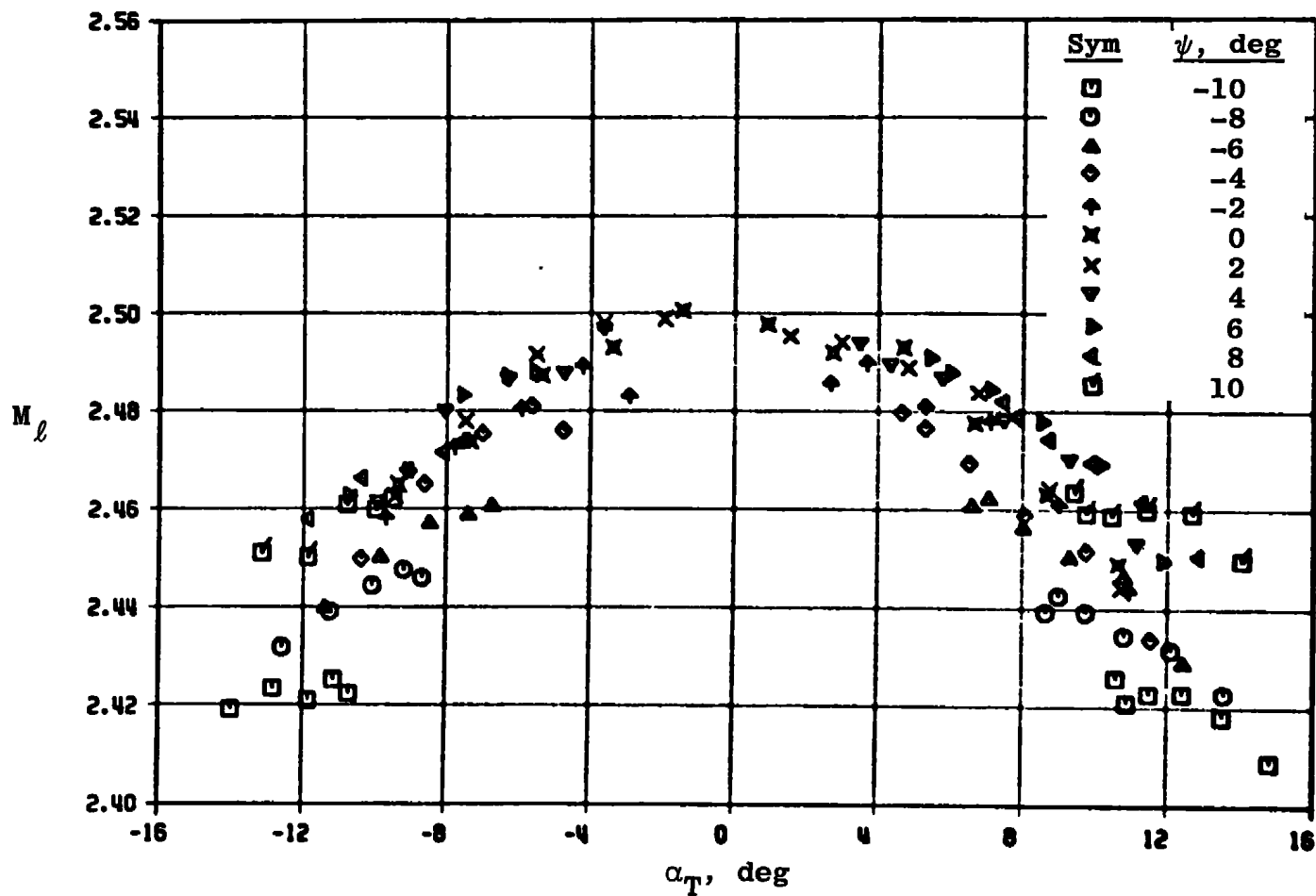


Figure 9. Total angle-of-attack effect on the uncorrected indicated cone probe Mach number at $M_\infty = 2.5$.

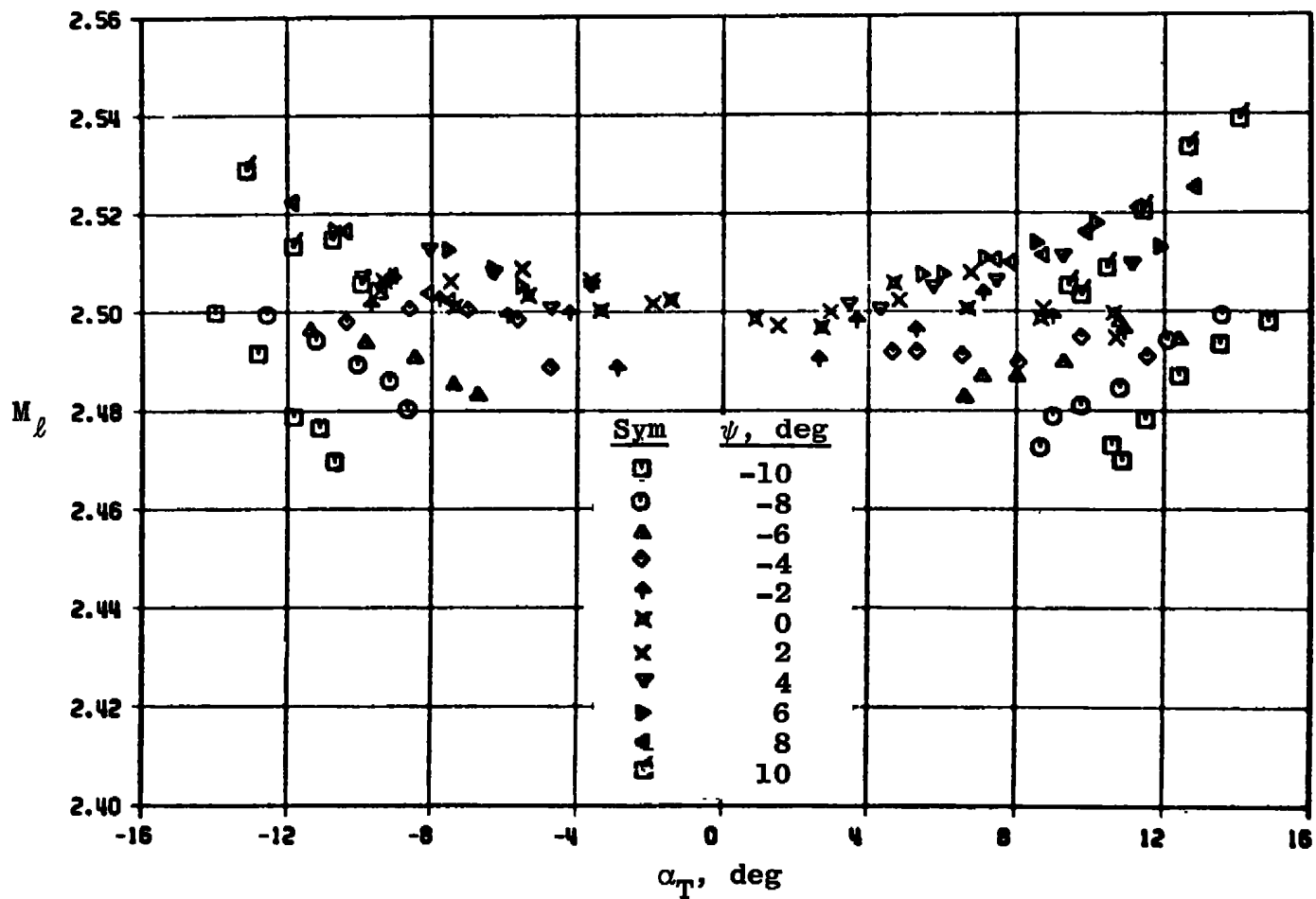


Figure 10. Total angle-of-attack correction on the indicated cone probe Mach number at $M_\infty = 2.5$.

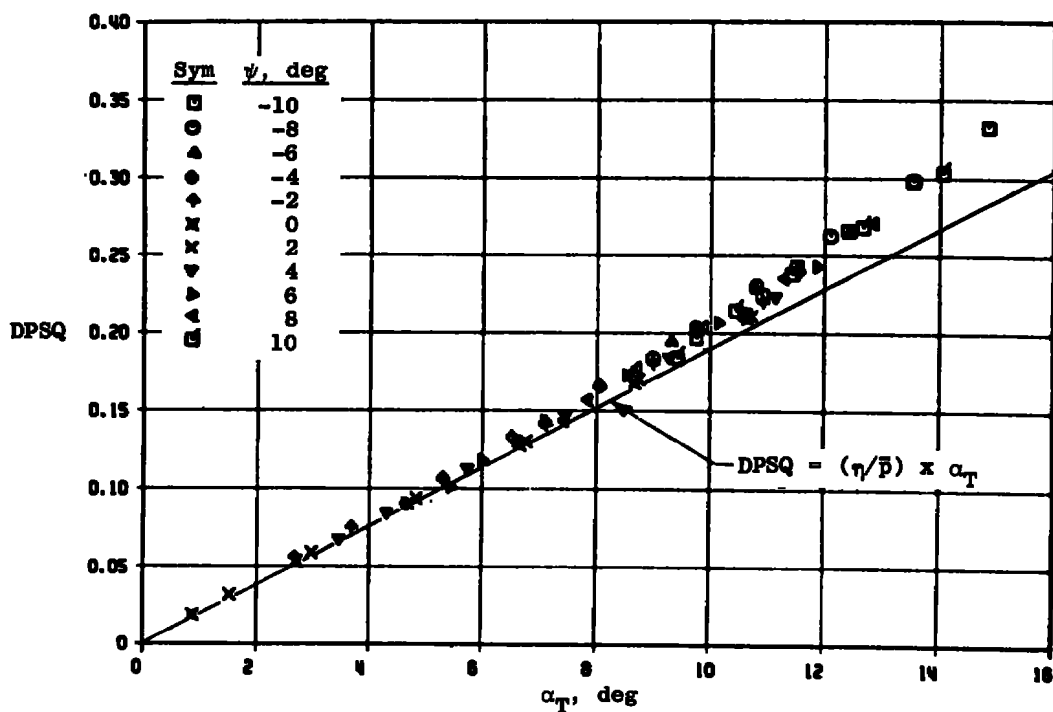
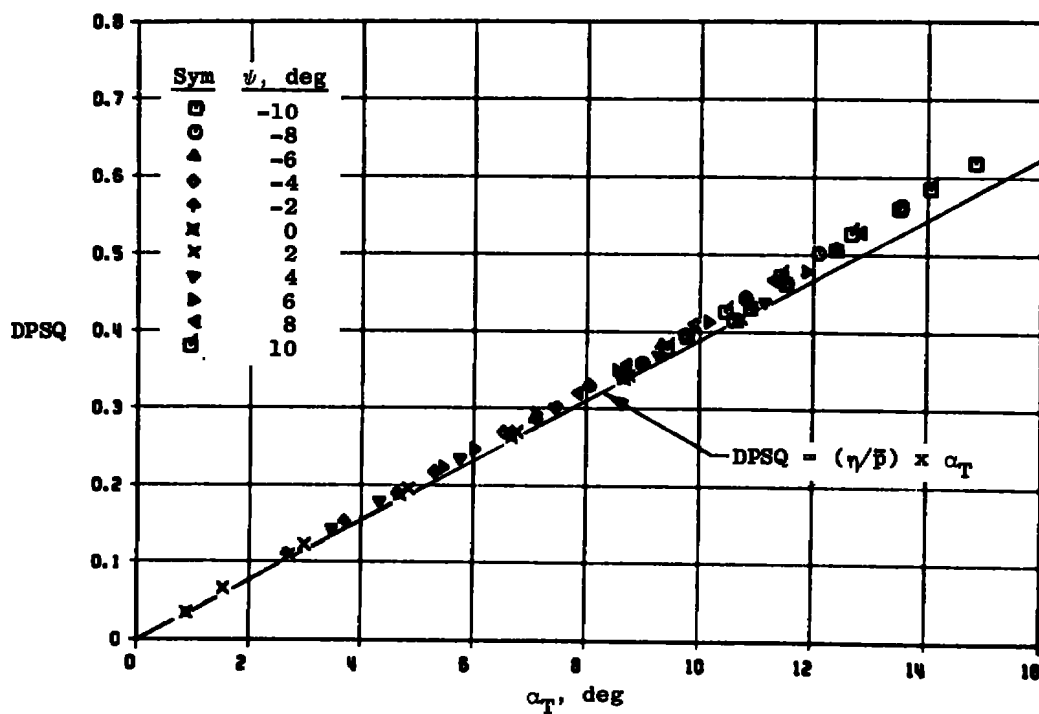
a. $M_\infty = 1.50$ b. $M_\infty = 2.50$

Figure 11. Cone probe calibration for flow angularity (probe No. 1).

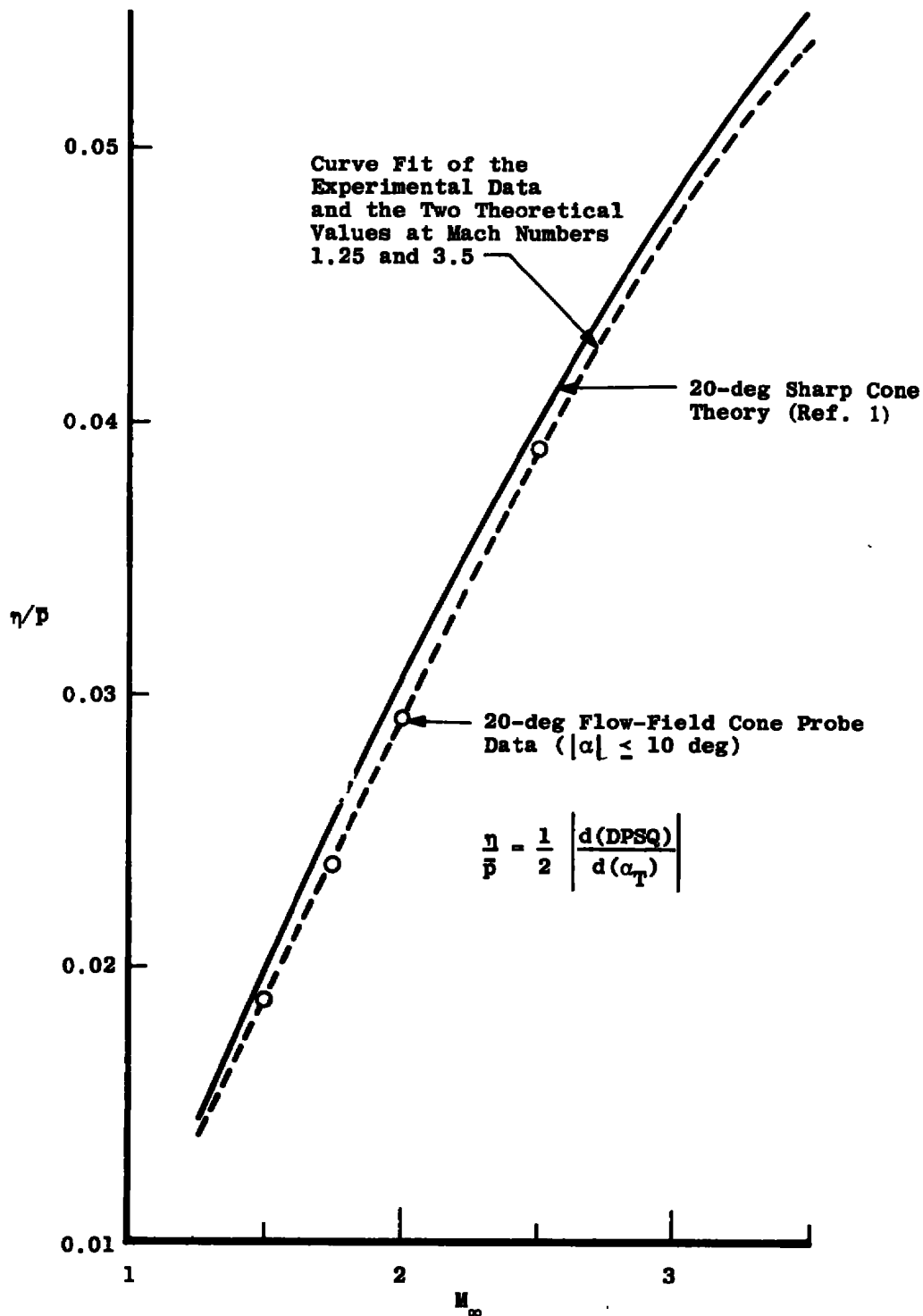


Figure 12. Summary of the linear flow angularity factor (η/\bar{p}) for a 20-deg half-angle cone as a function of free-stream Mach number.

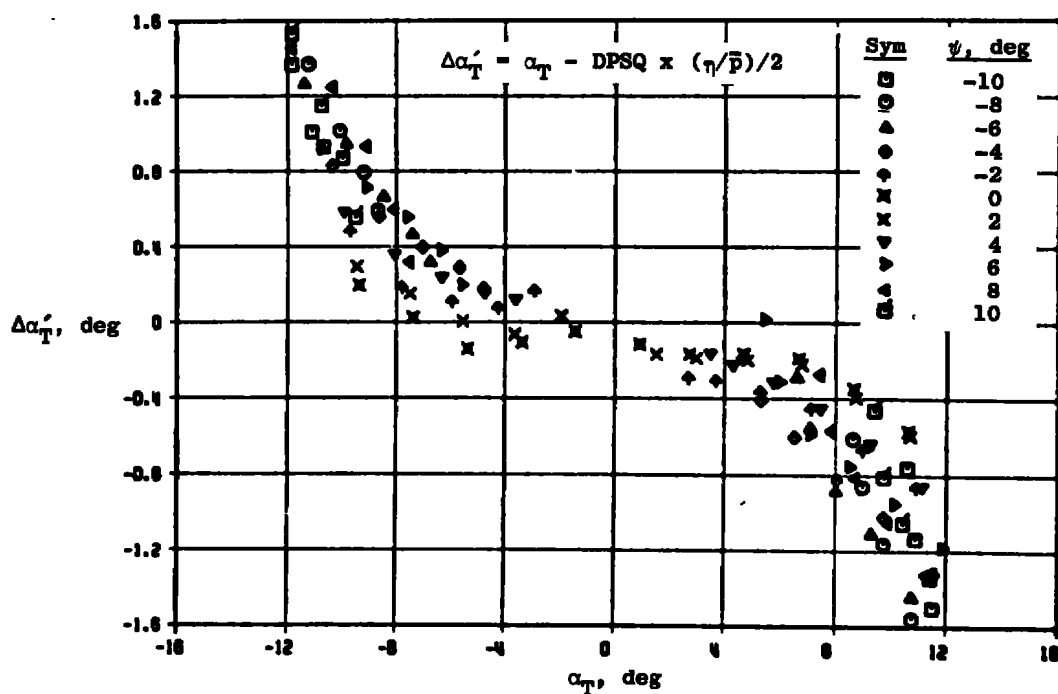
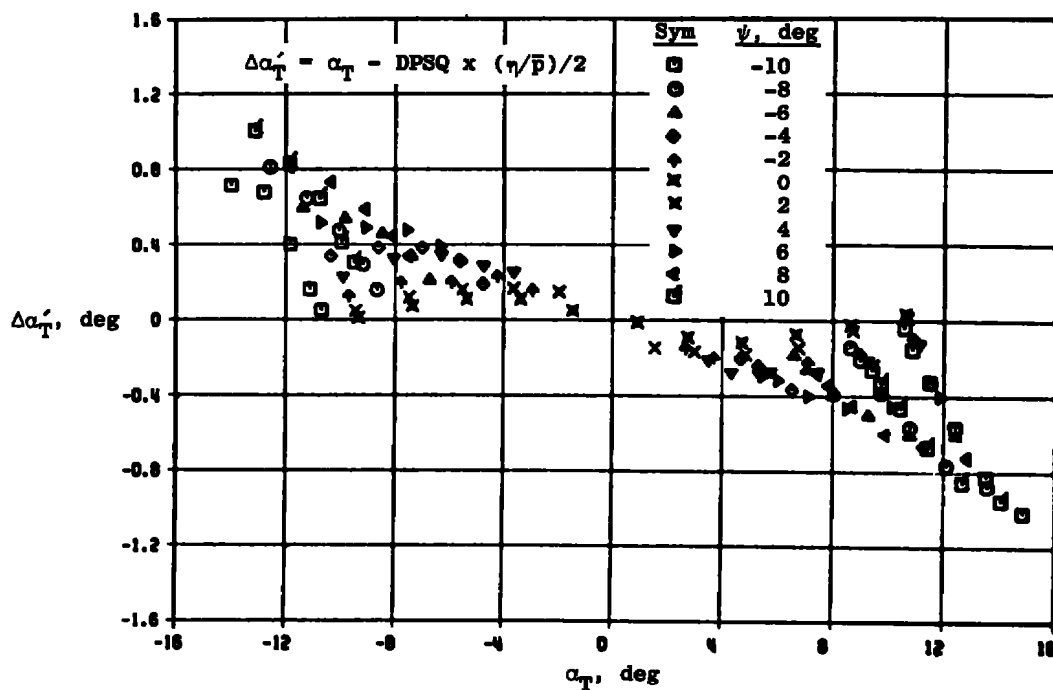
a. $M_\infty = 1.50$ b. $M_\infty = 2.50$

Figure 13. The residual error in the flow-field angularity computation based on a linear calibration factor, η/\bar{p} .

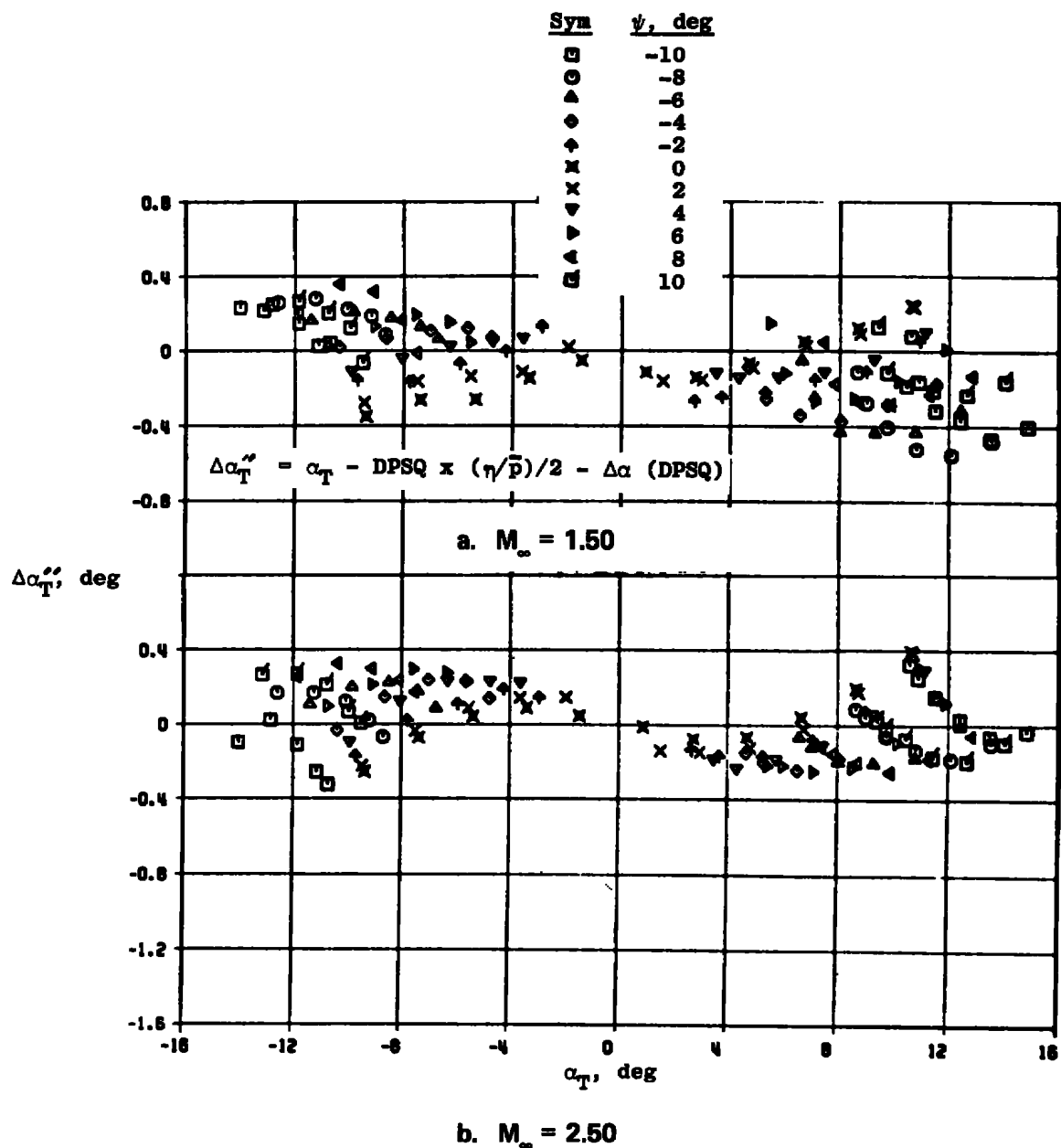


Figure 14. Reduced residual error in the flow-field angularity computation containing a correction for nonlinearity in the calibration factor.

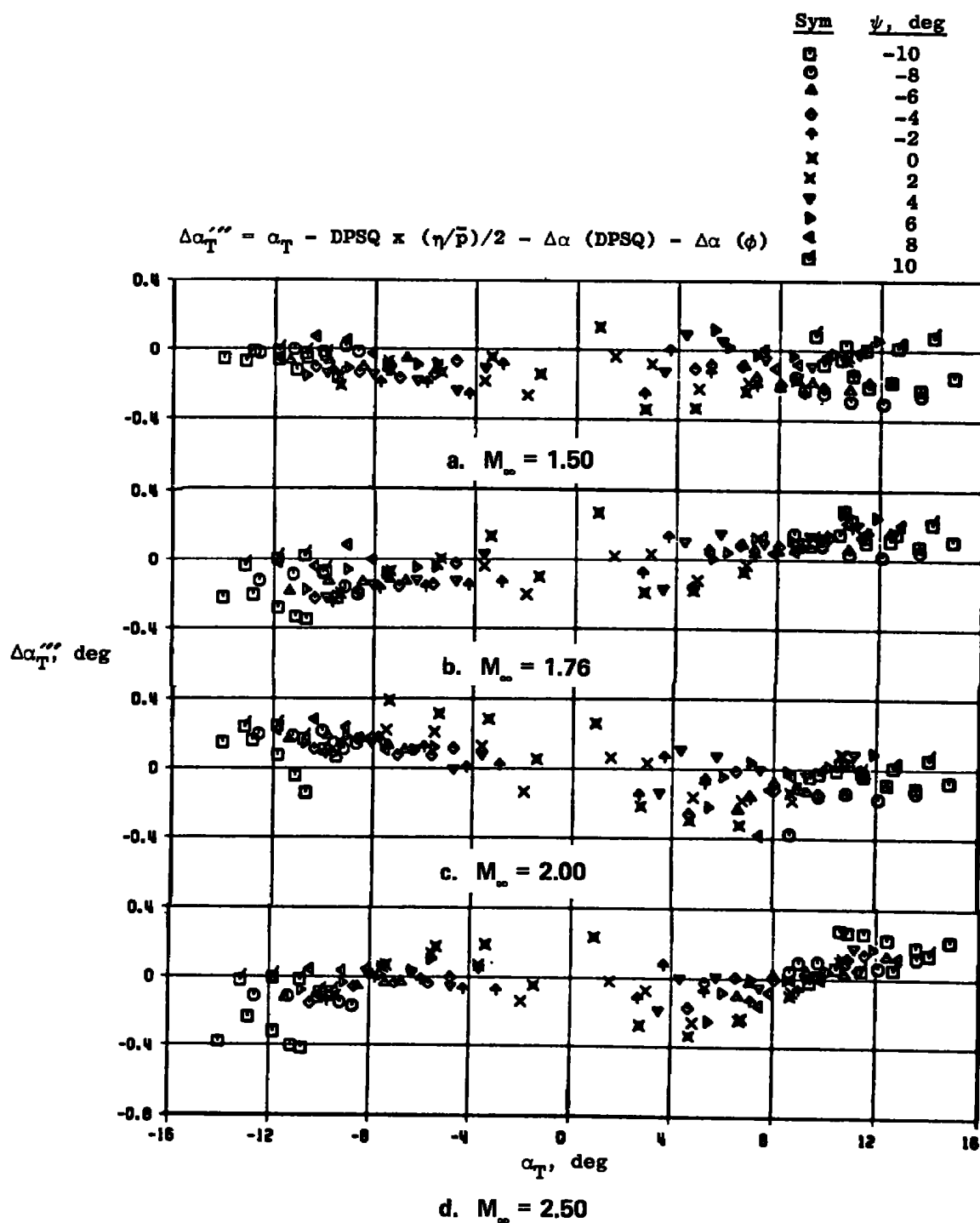


Figure 15. Final residual error in the present flow-field angularity computations with all corrections incorporated in the calibration.

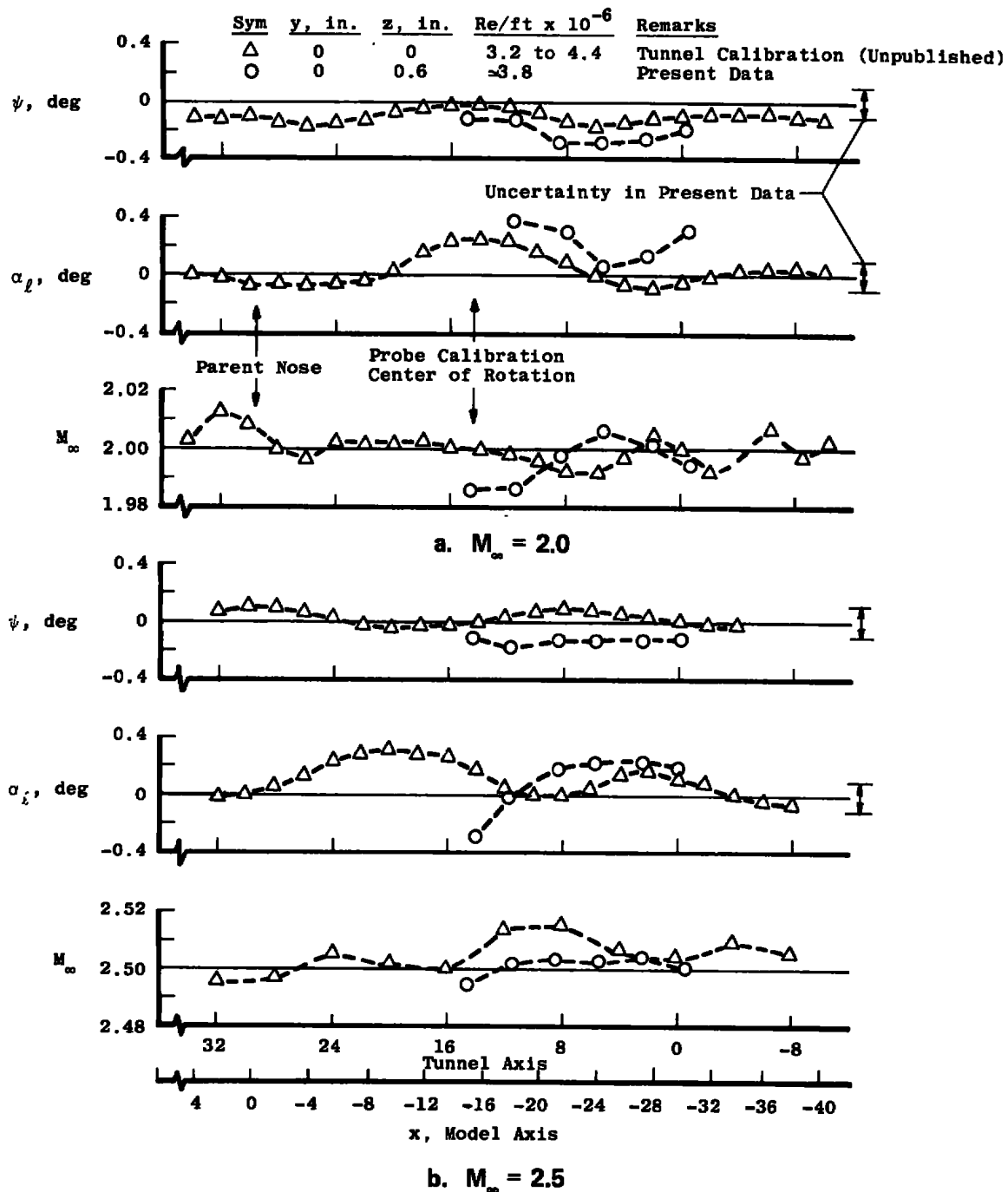


Figure 16. Comparison of the present empty tunnel flow-field survey results with Tunnel A calibration data.

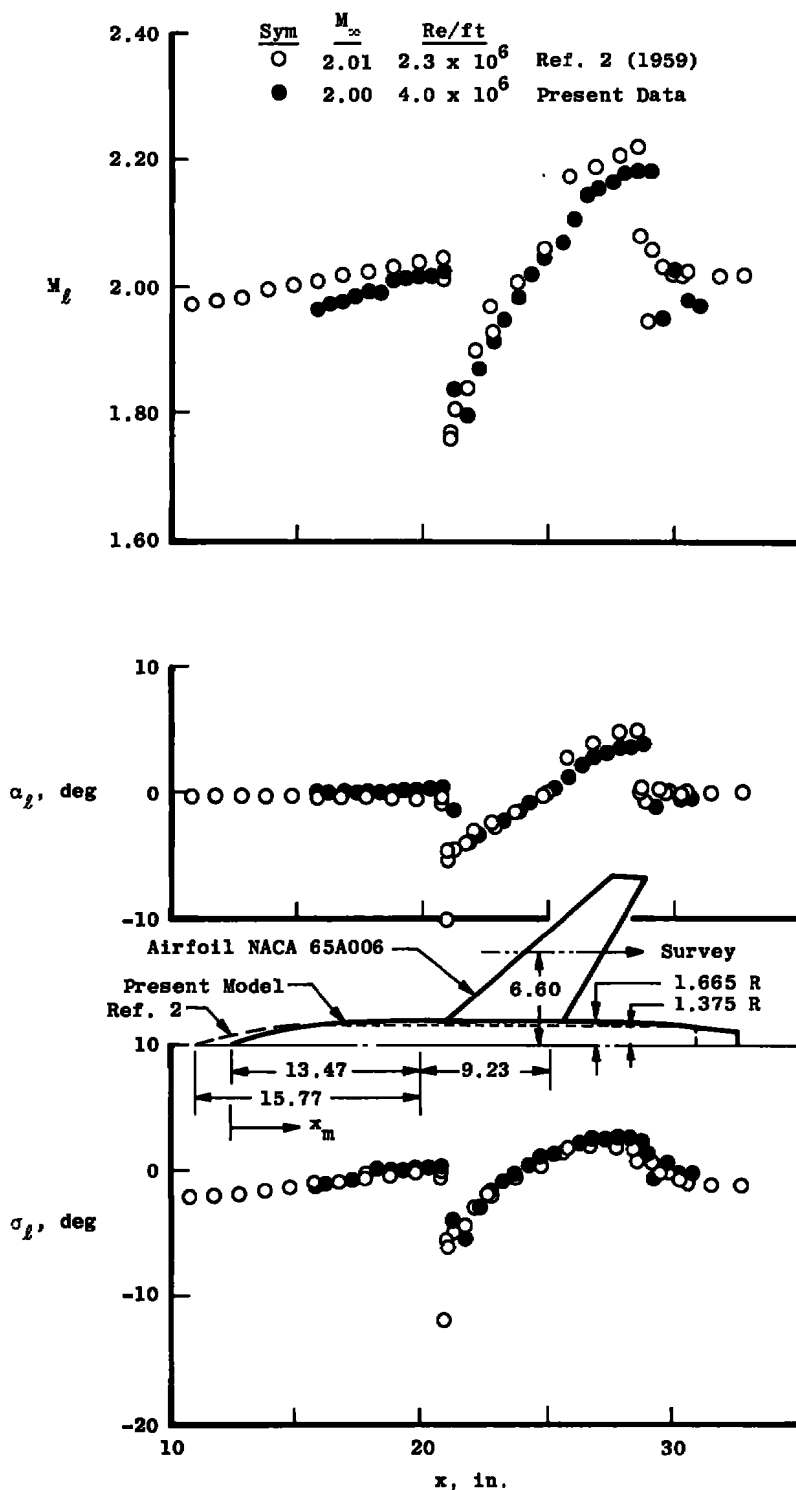
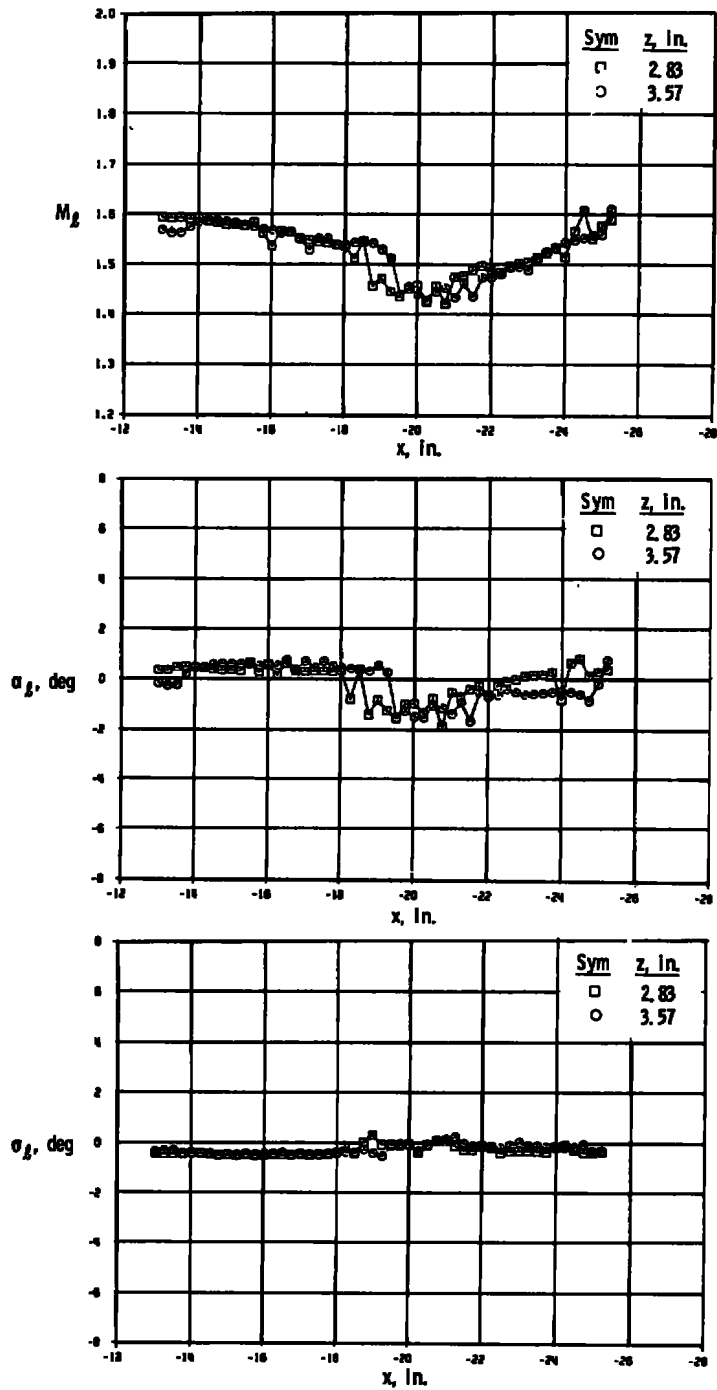
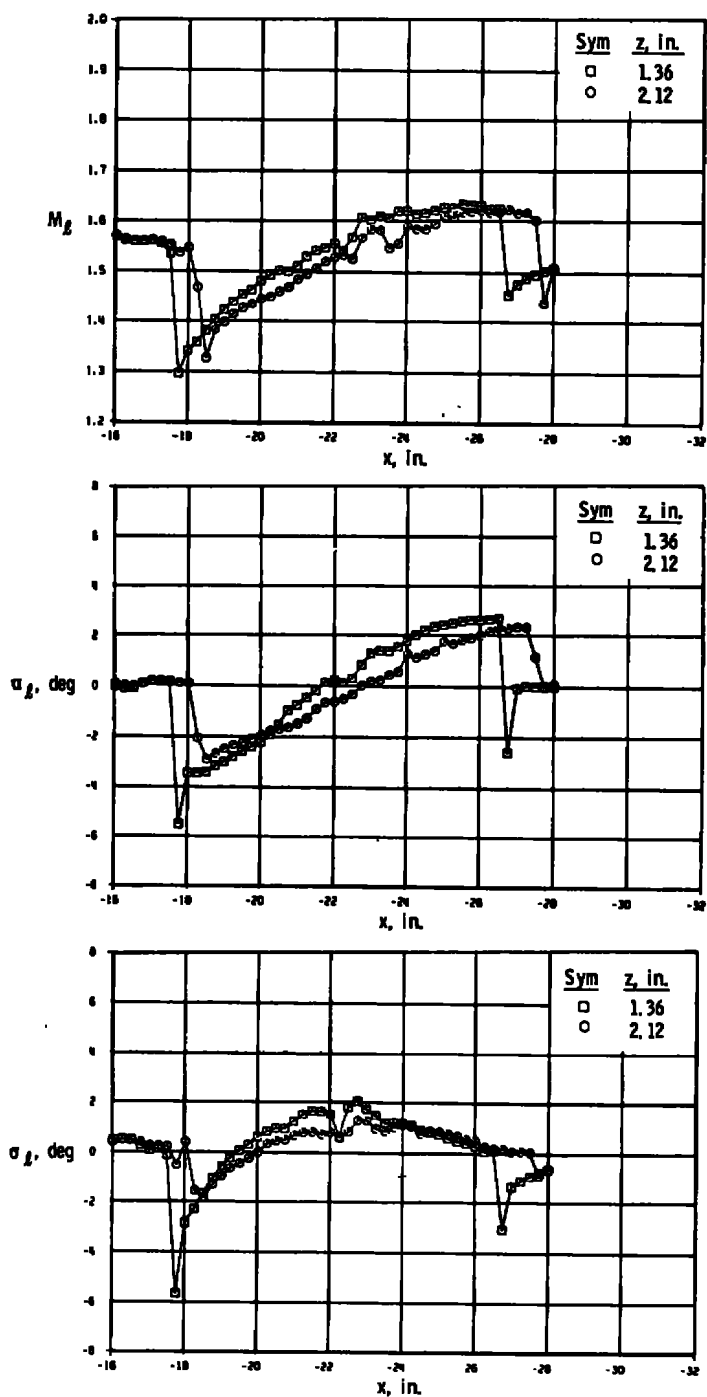


Figure 17. Comparison of flow-field survey data obtained at $M_\infty = 2$ over similar parent bodies.

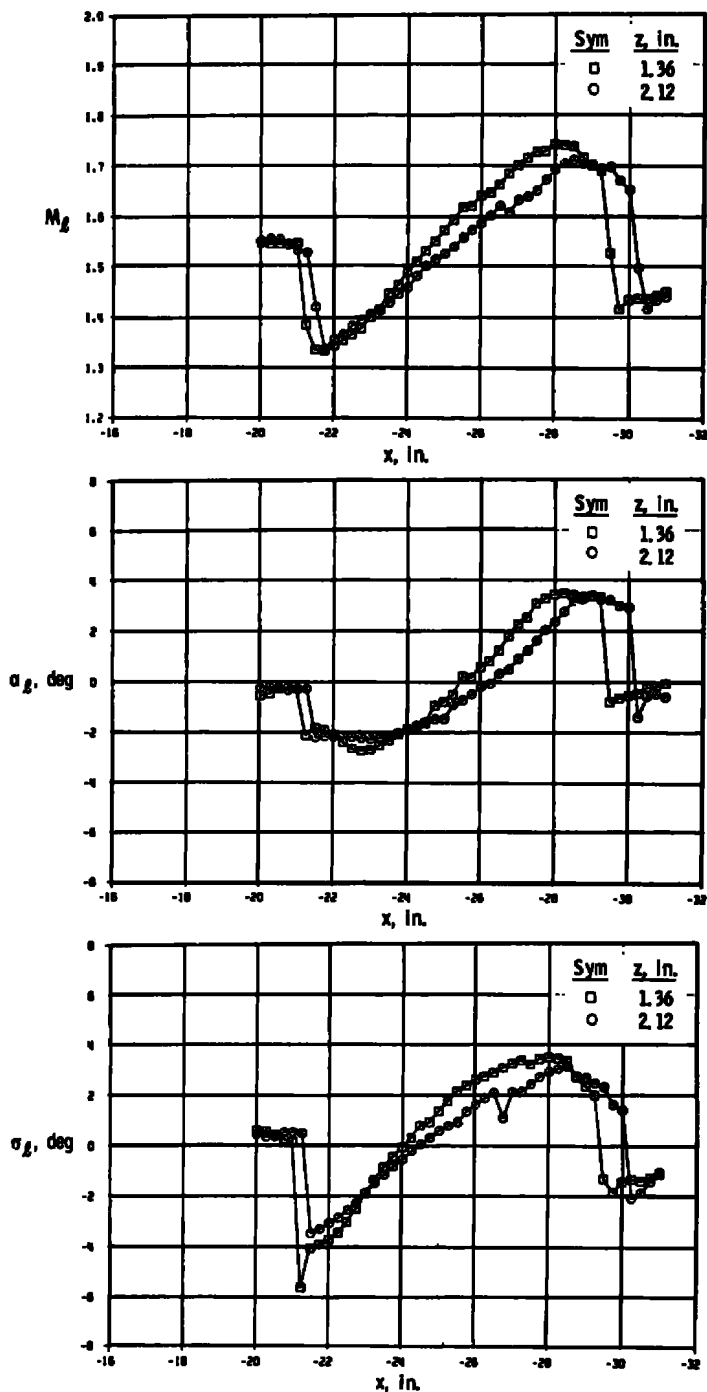


a. Centerbody pylon location, $y = 0$

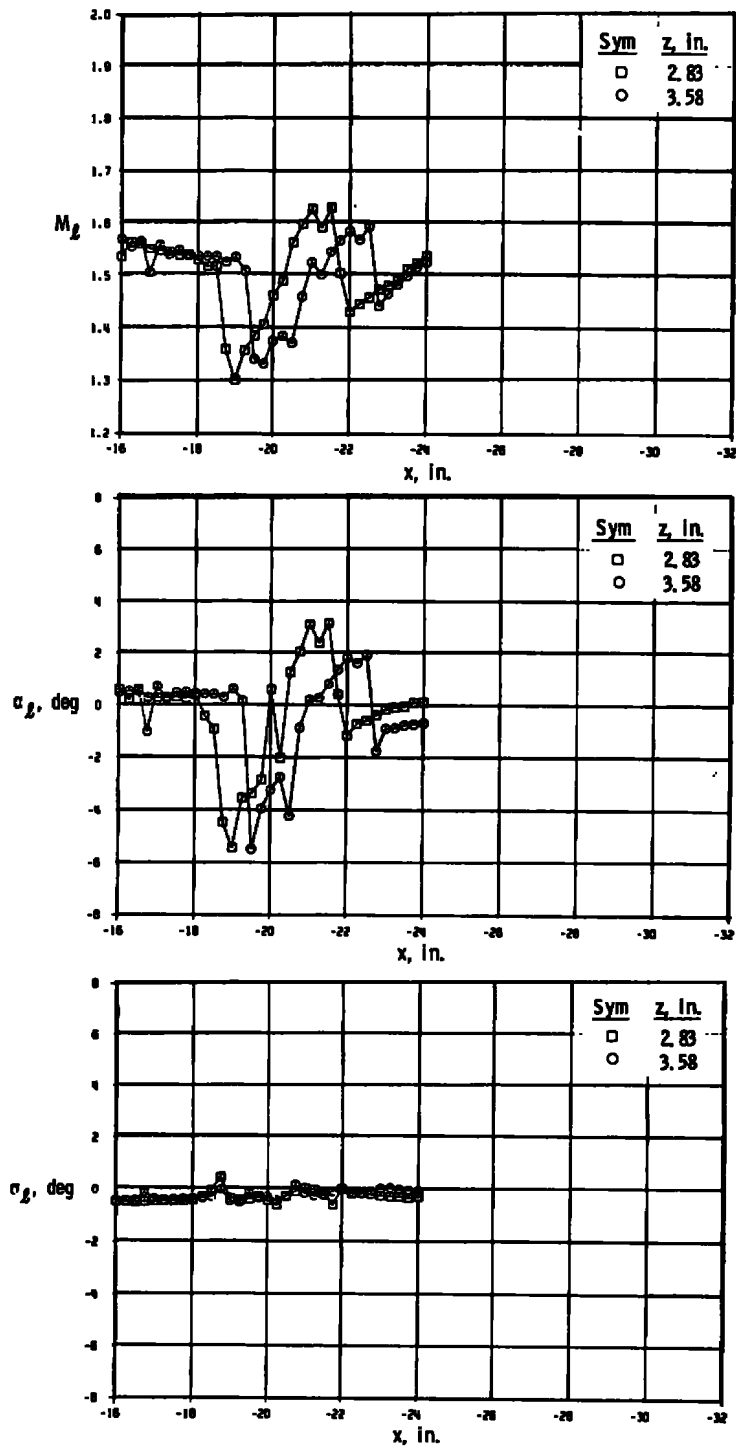
Figure 18. Local flow-field properties over the parent body without pylons, $\alpha = 0$, $M_\infty = 1.5$, $Re/ft = 4 \times 10^6$.



b. 1/3-wing pylon station, $y = -4.0$ in.
Figure 18. Continued.

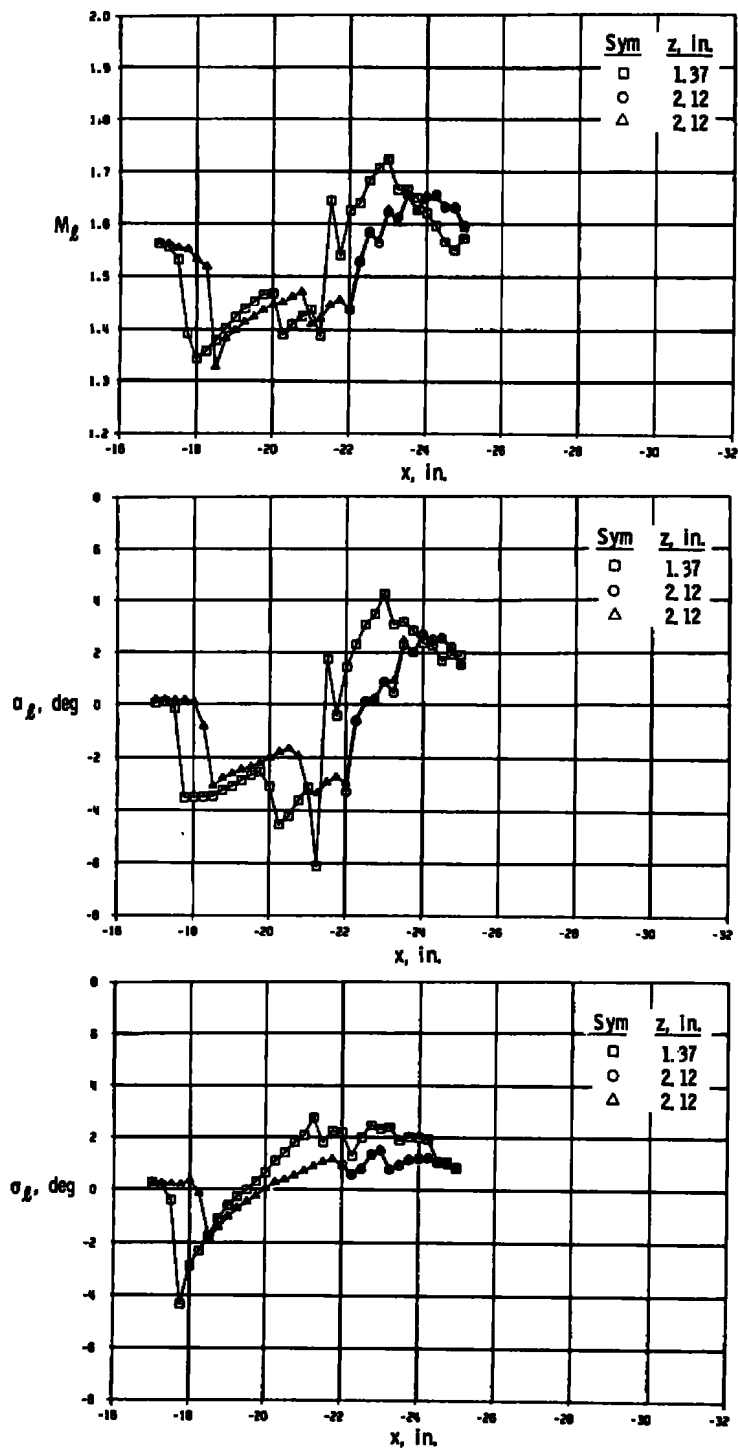


c. 2/3-wing pylon station, $y = -8.0$ in.
Figure 18. Concluded.

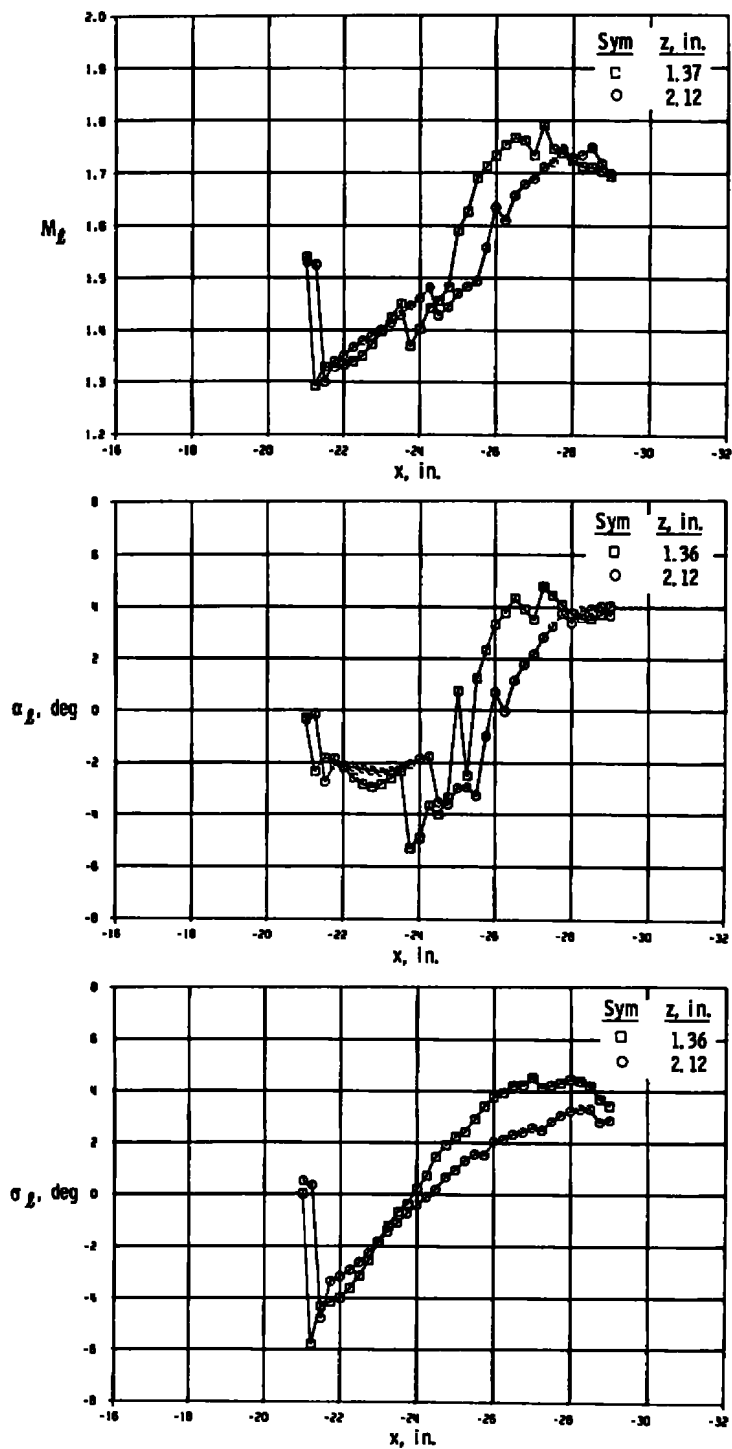


a. Centerbody pylon location, $y = 0$

Figure 19. Local flow-field properties over the parent body with the pylon attached, $\alpha = 0$, $M_\infty = 1.5$, $Re/ft = 4 \times 10^6$.

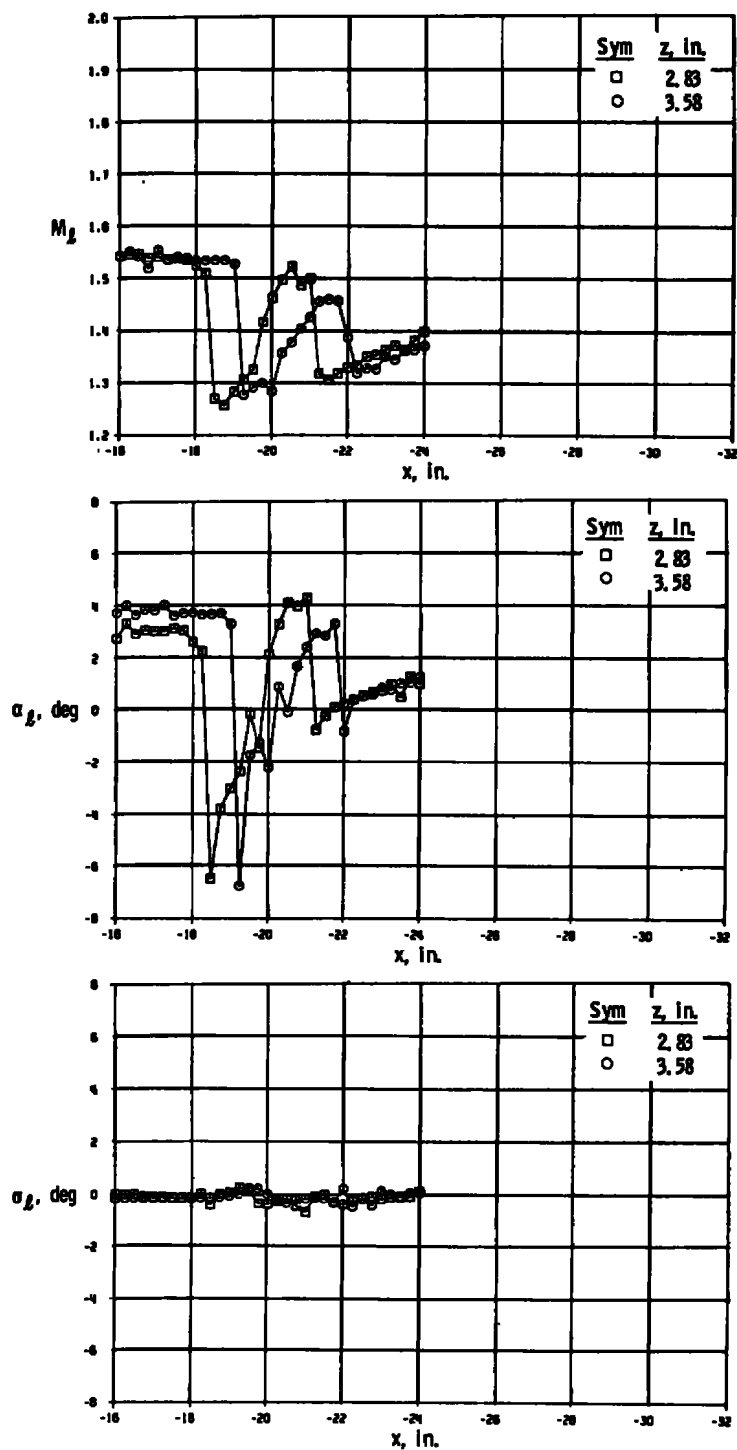


b. 1/3-wing pylon station, $y = -4.0$ in.
Figure 19. Continued.



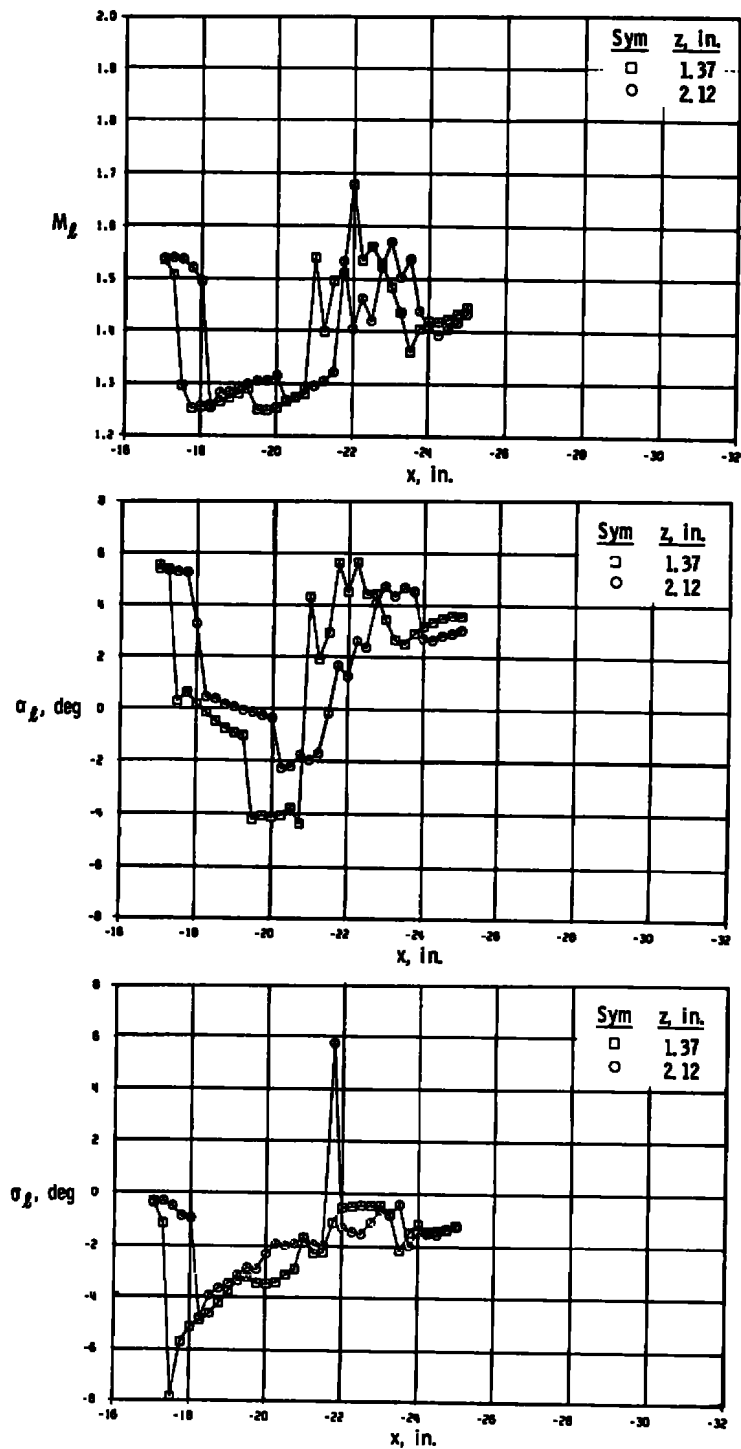
c. 2/3-wing pylon station, $y = -8.0$ in.

Figure 19. Concluded.

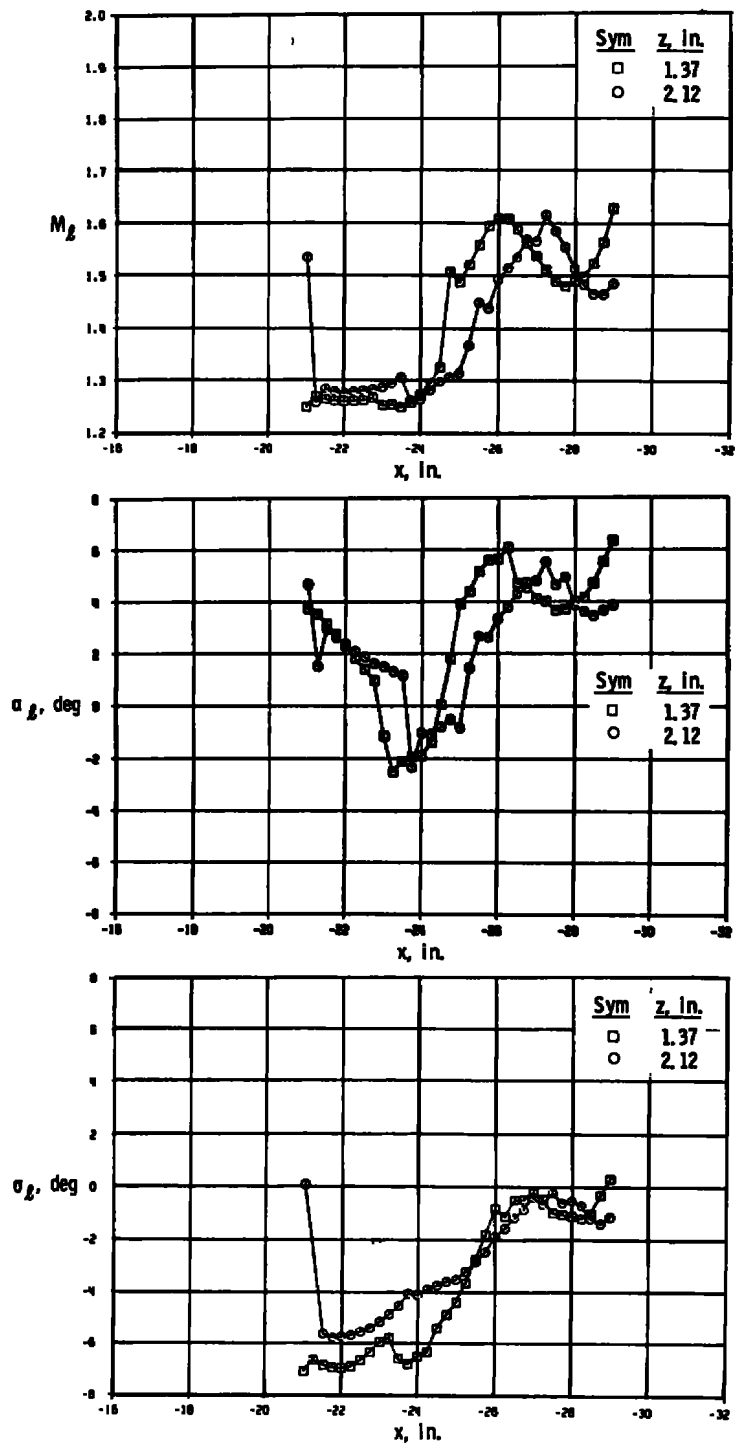


a. Centerbody pylon location, $y = 0$

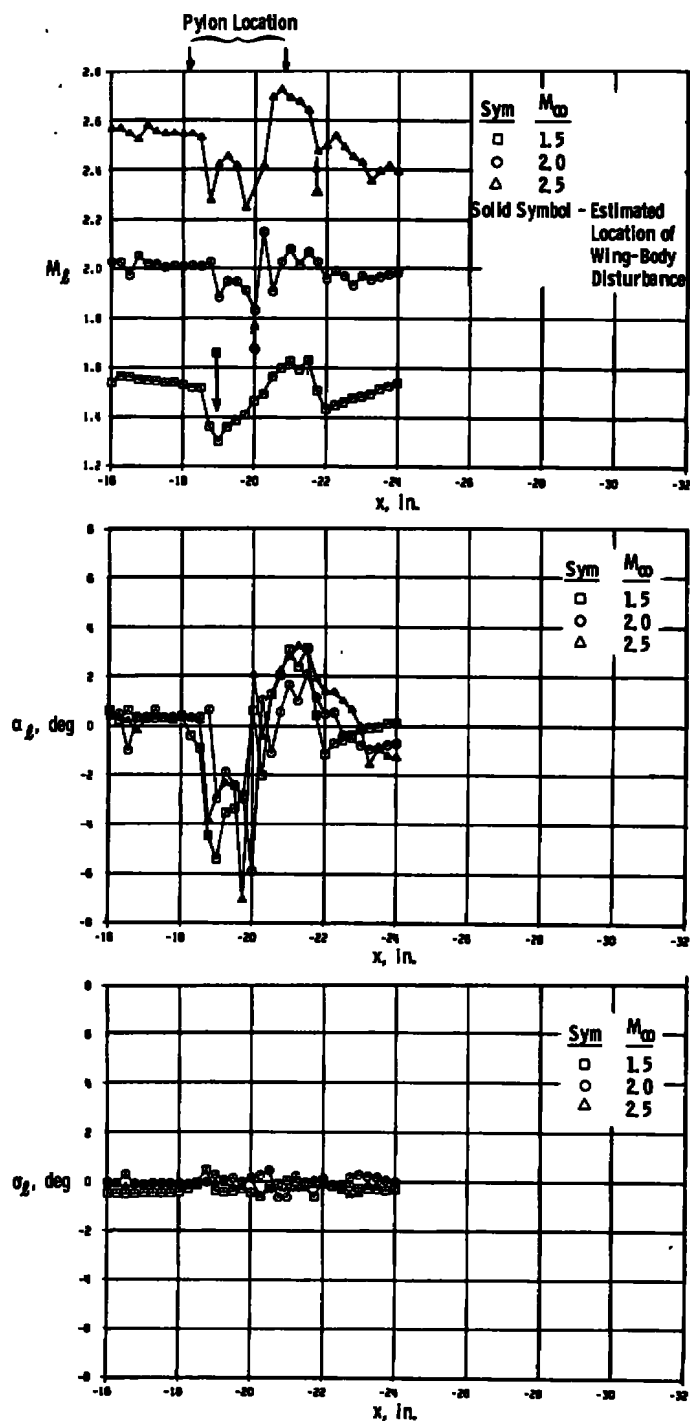
Figure 20. Local flow-field properties over the parent body with the pylon attached, $\alpha = 5$ deg, $M_\infty = 1.5$, $Re/ft = 4 \times 10^6$.



b. 1/3-wing pylon station, $y = -4.0$ in.
Figure 20. Continued.

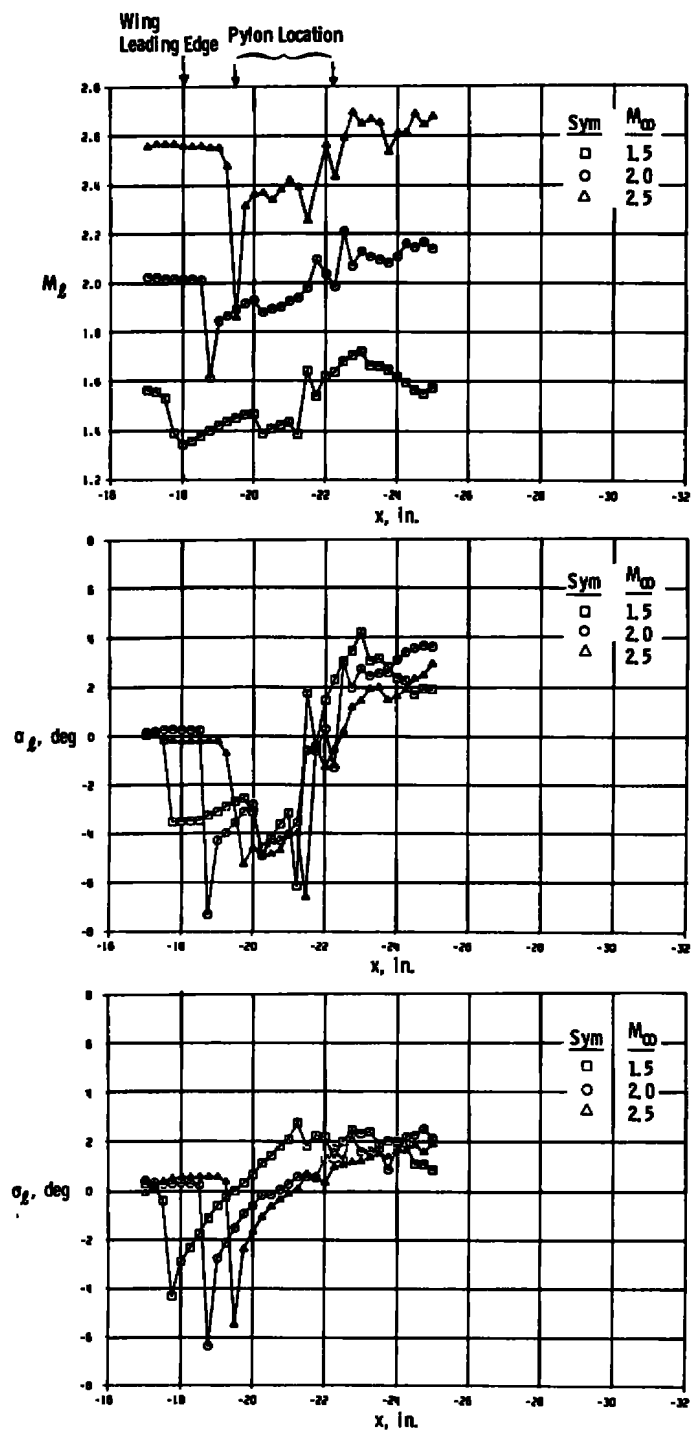


c. 2/3-wing pylon station, $y = -8.0$ in.
Figure 20. Concluded.

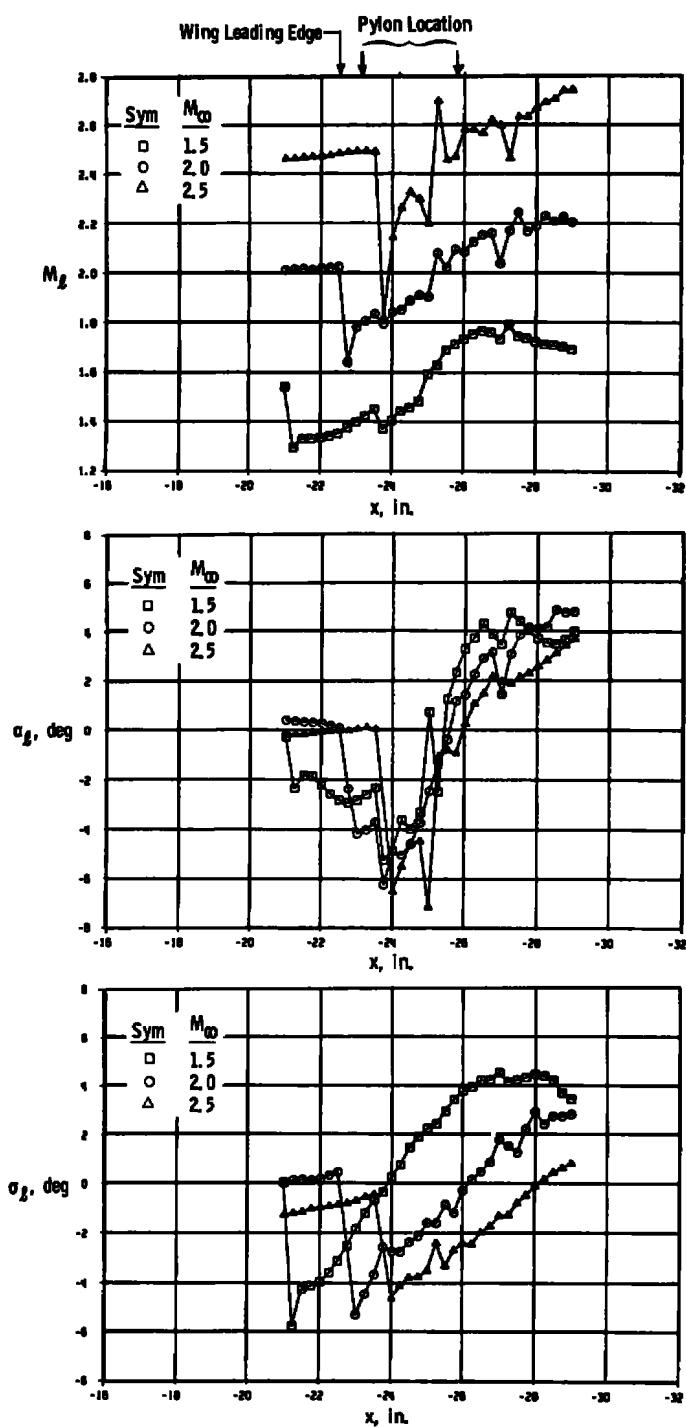


a. Centerbody pylon location, $y = 0$

Figure 21. Example of free-stream Mach number effects on the local flow-field properties over the parent body with the pylon attached, $\alpha = 0$, $\Delta z = 0$.



b. 1/3-wing pylon station, $y = -4.0 \text{ in.}$
Figure 21. Continued.



c. 2/3-wing pylon station, $y = -8.0$ in.
Figure 21. Concluded.

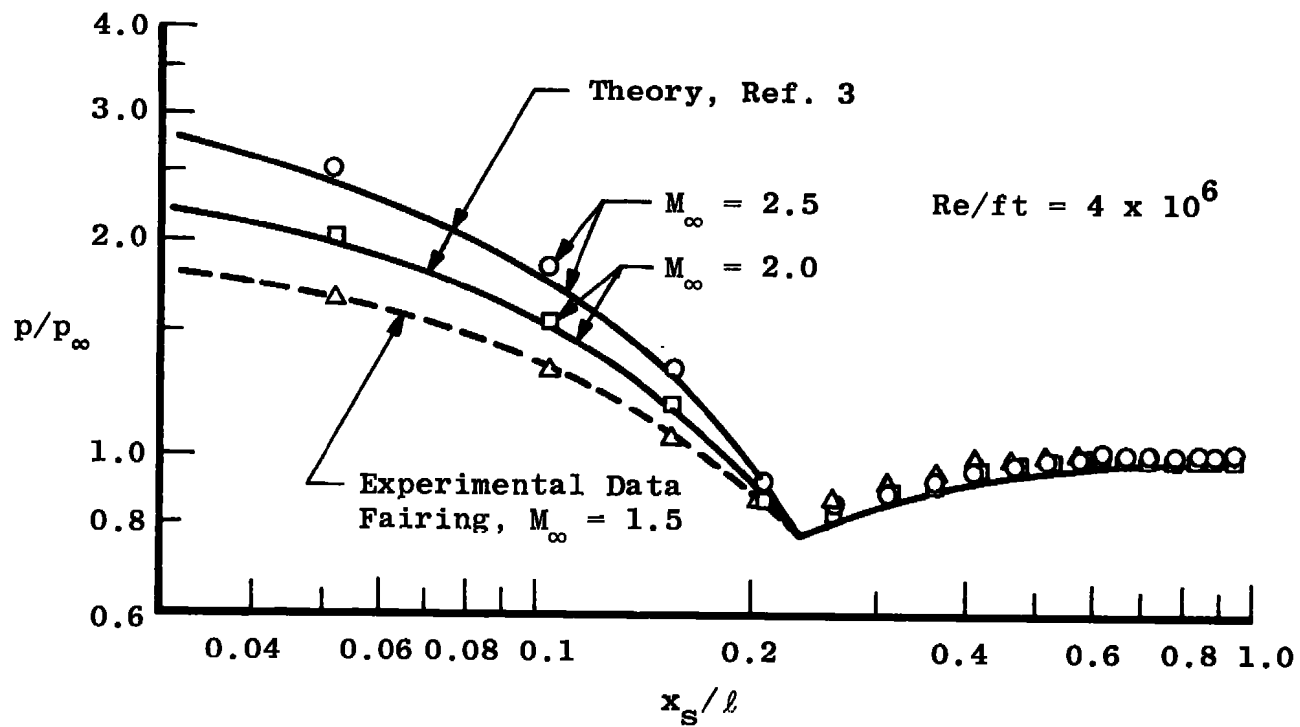


Figure 22. Store pressure distributions, $\alpha = 0$.

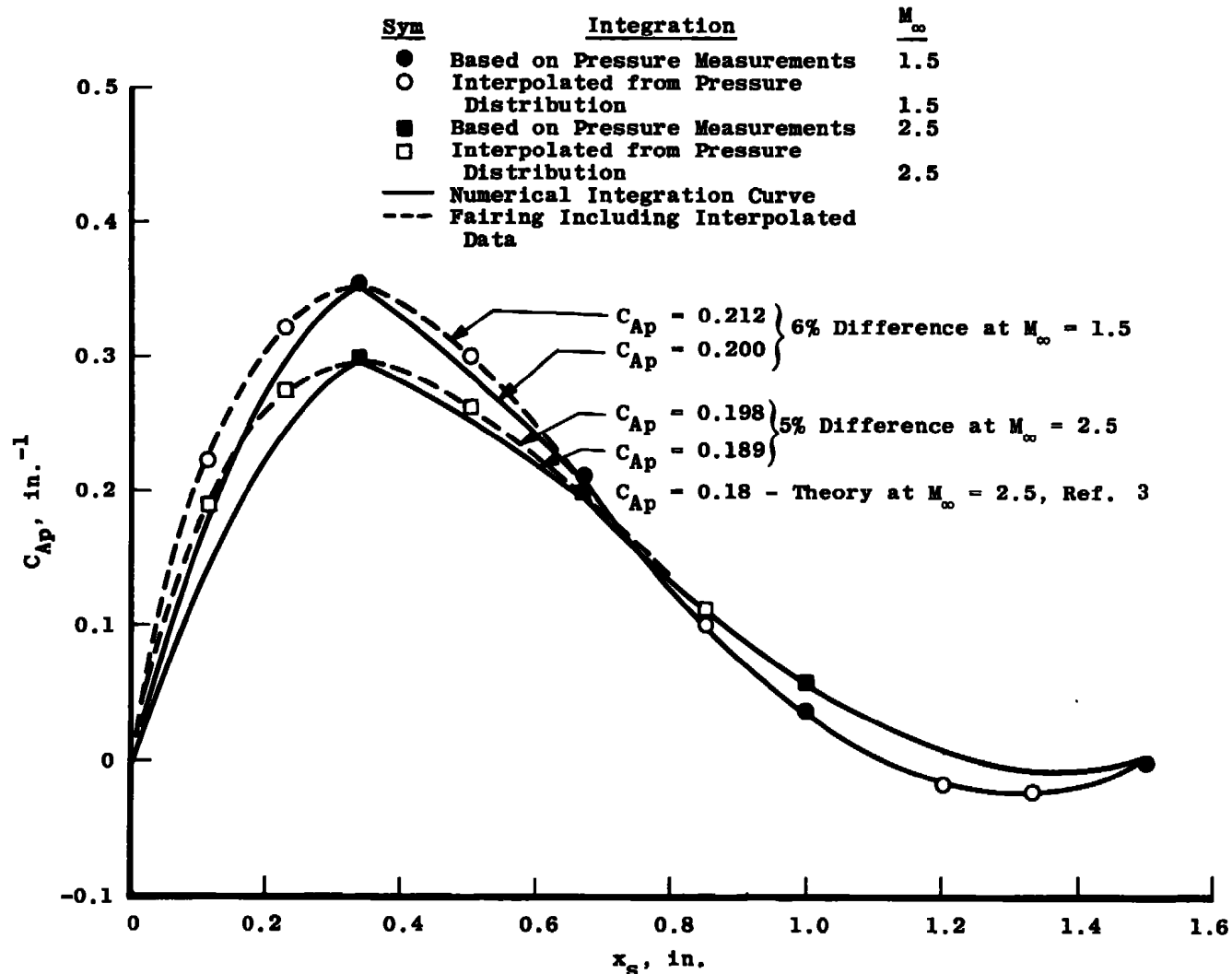
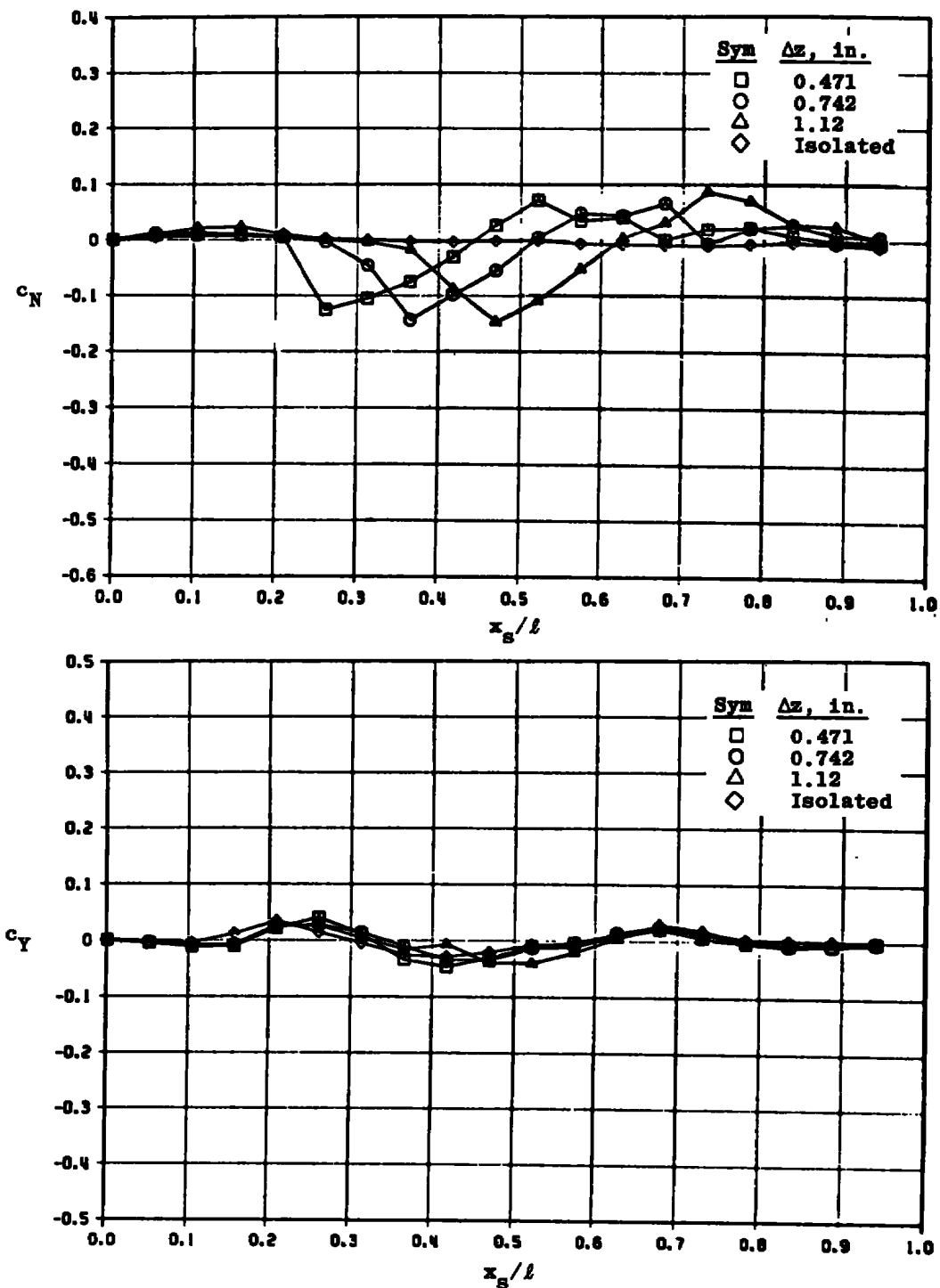
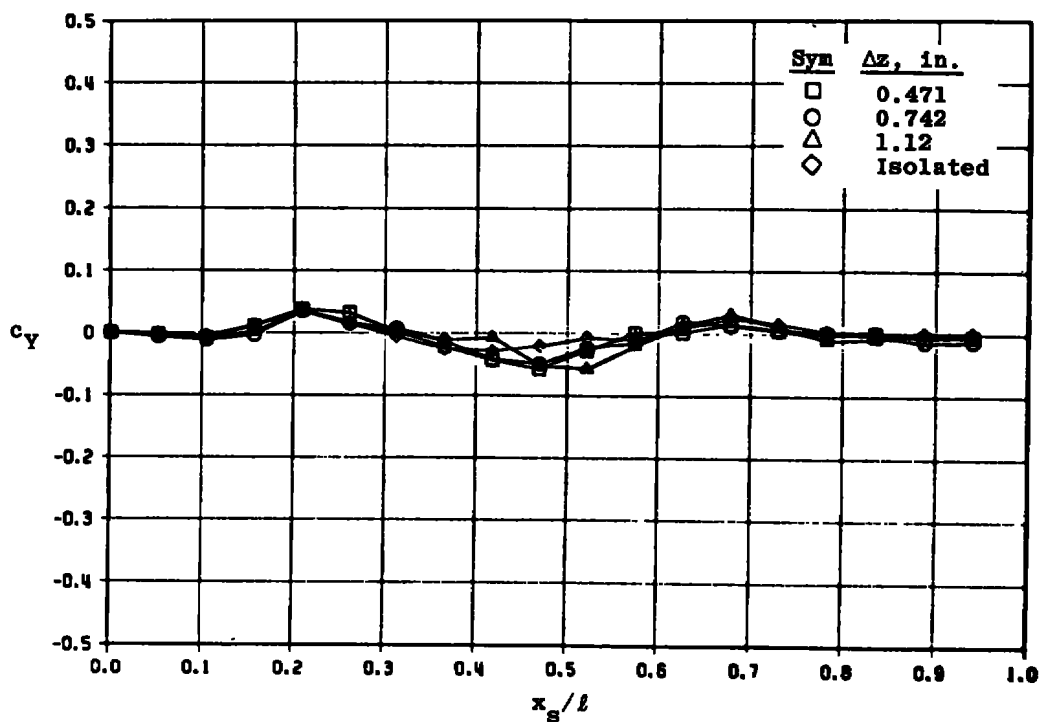
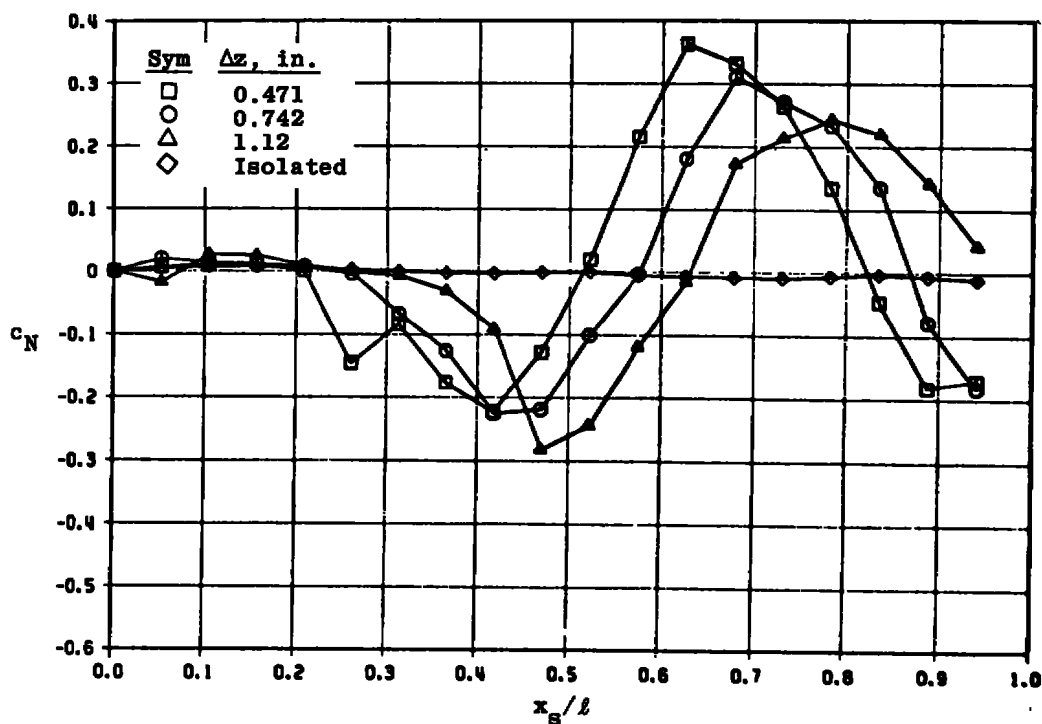


Figure 23. Uncertainties in the integrated forebody pressure drag coefficients (isolated storebody at $\alpha = 0$, $M_\infty = 1.5$ and 2.5).



a. Pylons off

Figure 24. Local aerodynamic loading on the store center pylon station, $\Delta y = 0$, $\alpha = 0$, $M_\infty = 1.5$, $Re/ft = 4 \times 10^6$.



b. Pylon on
Figure 24. Concluded.

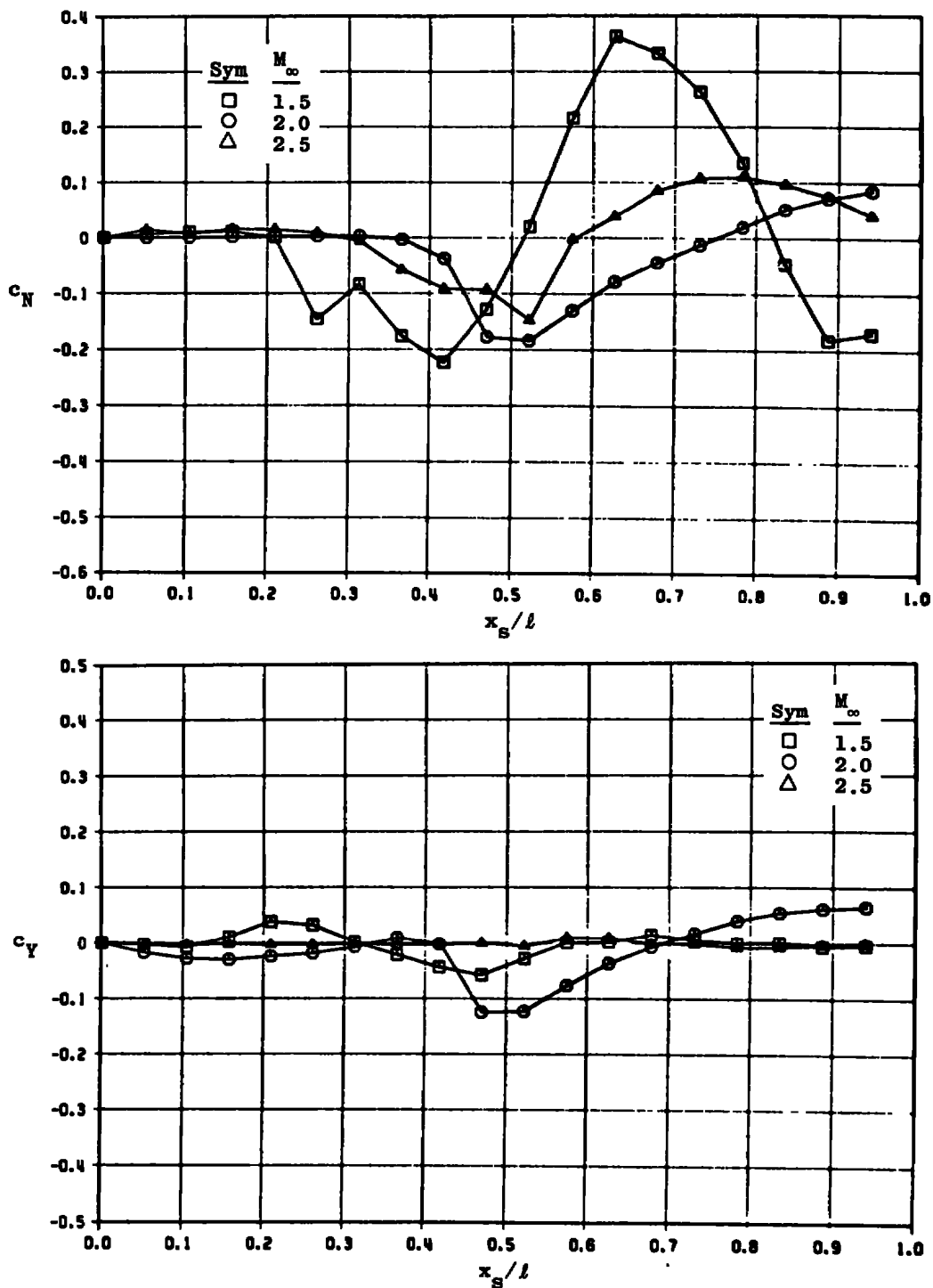
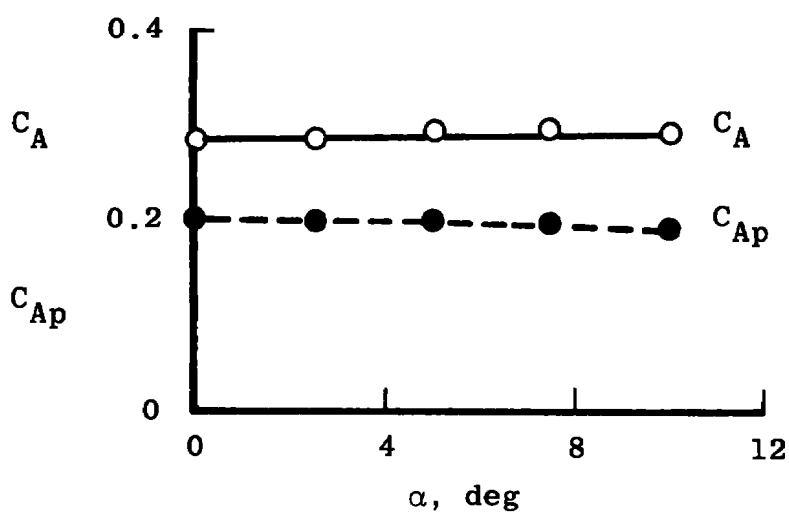
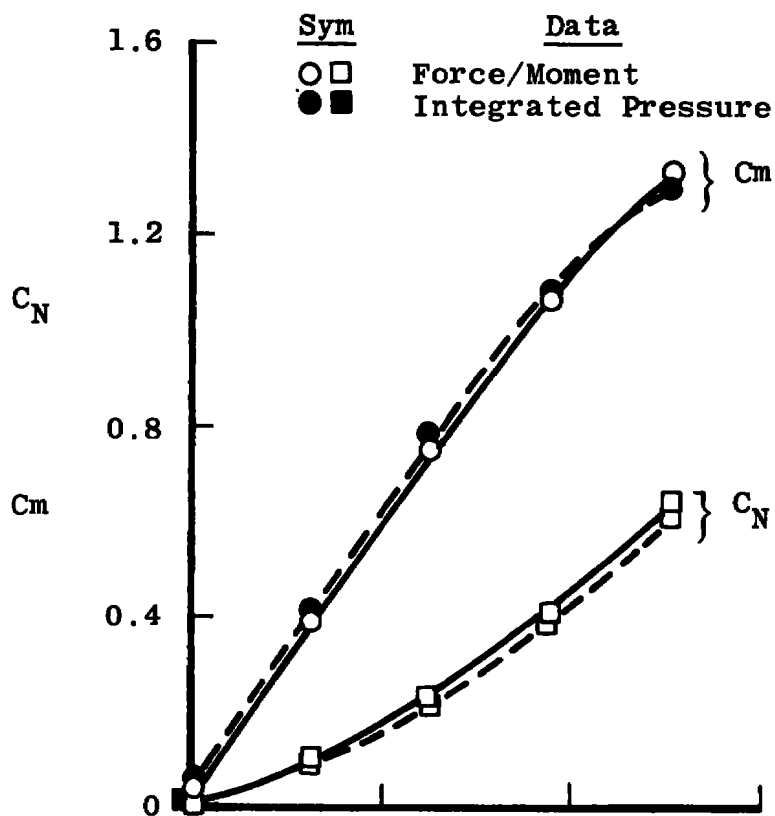
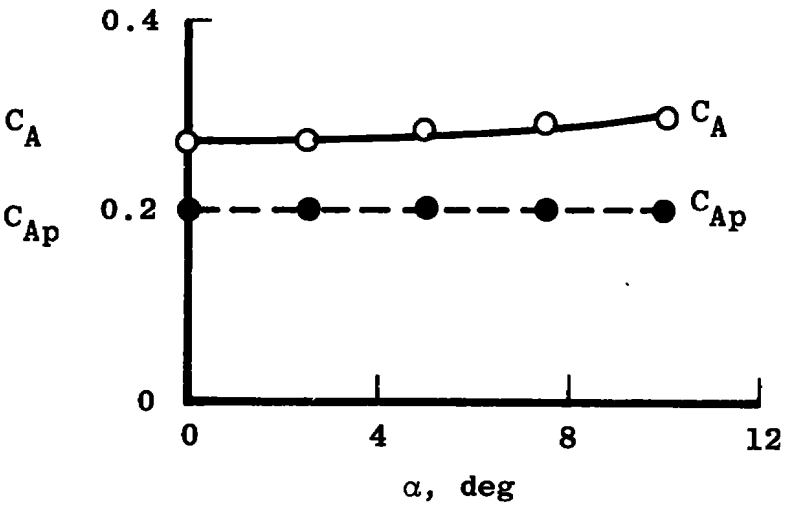
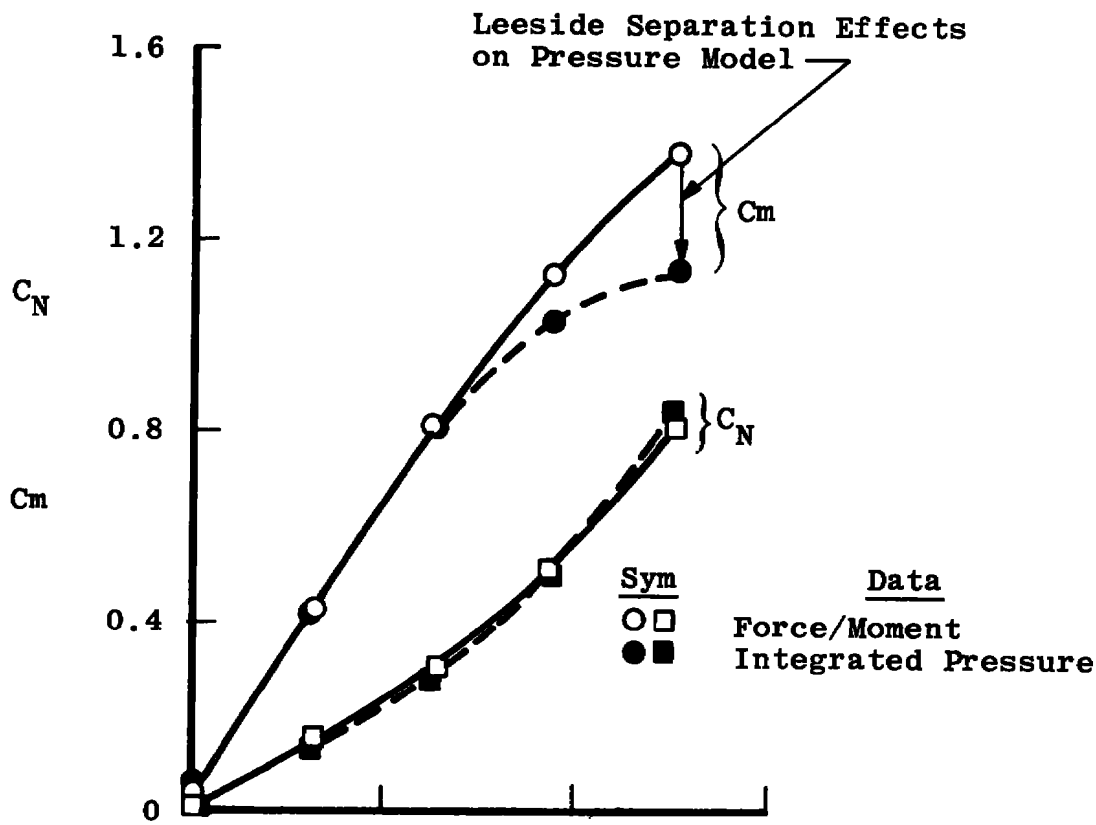


Figure 25. Free-stream Mach number effects on the local aerodynamic loading of the store in the presence of the parent body with the center pylon, $\alpha = 0$, $\Delta y = 0$, $\Delta z = 0.47$ in.

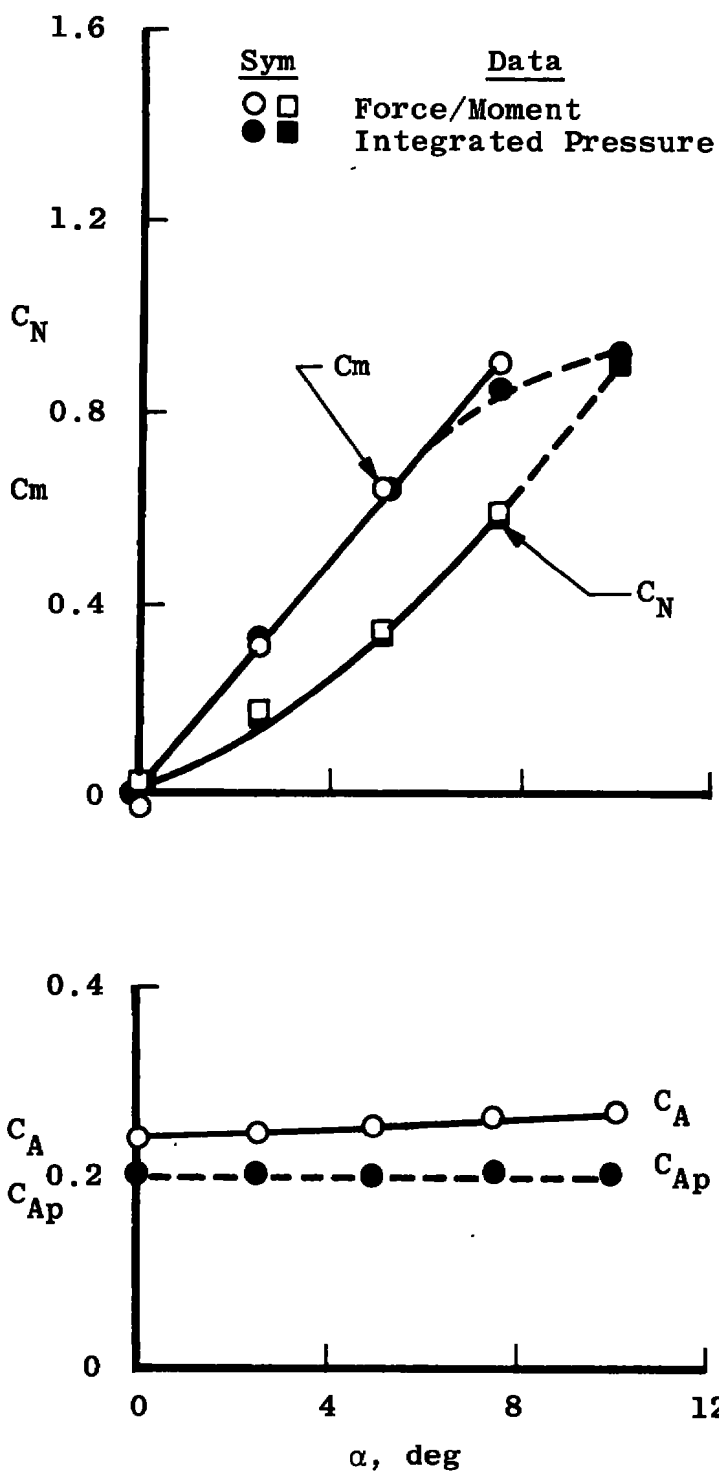


a. $M_\infty = 1.5$

Figure 26. Comparison of isolated storebody force and integrated pressure data ($Re/ft = 4 \times 10^6$).



b. $M_\infty = 2.0$
Figure 26. Continued.



c. $M_\infty = 2.50$
 Figure 26. Concluded.

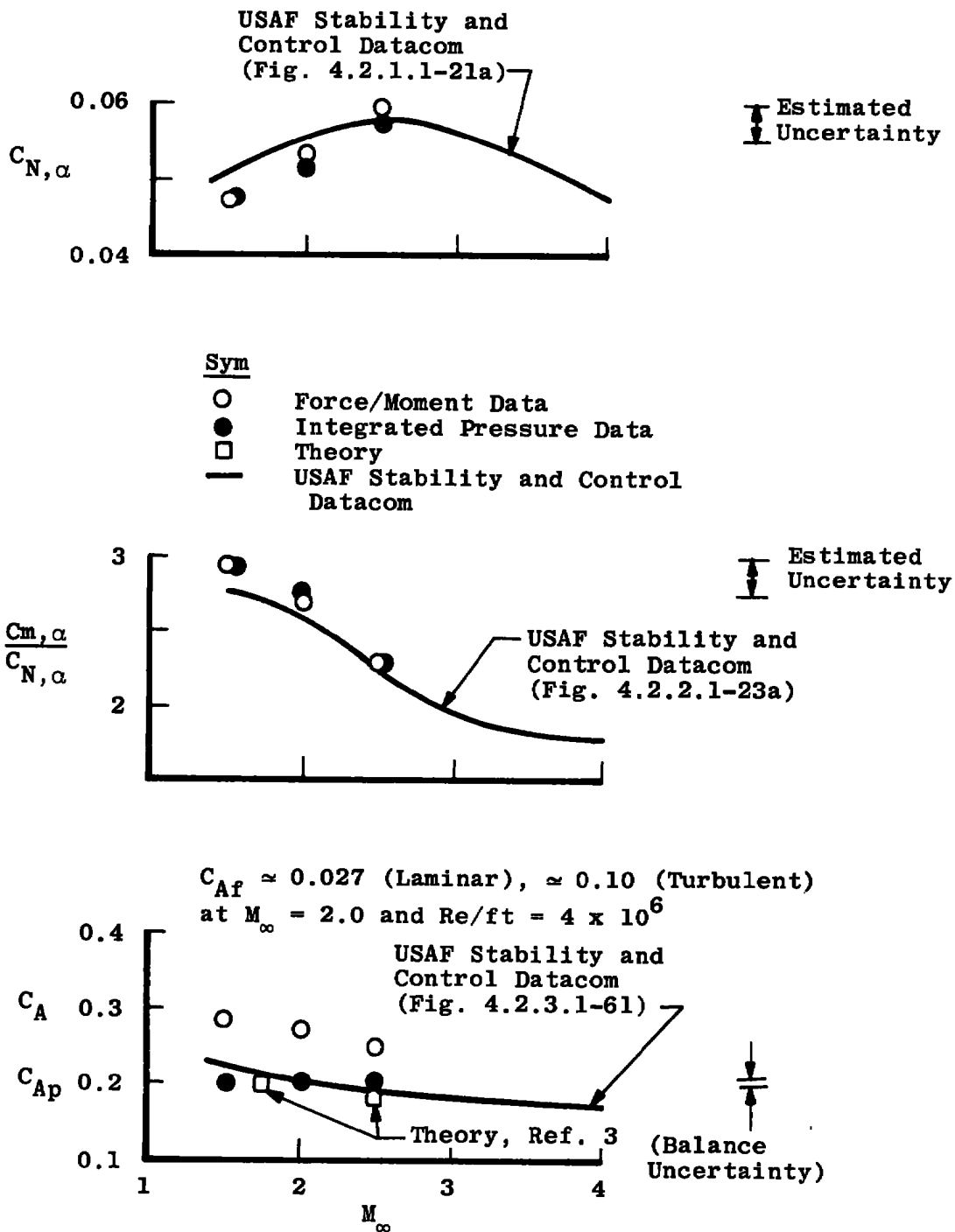
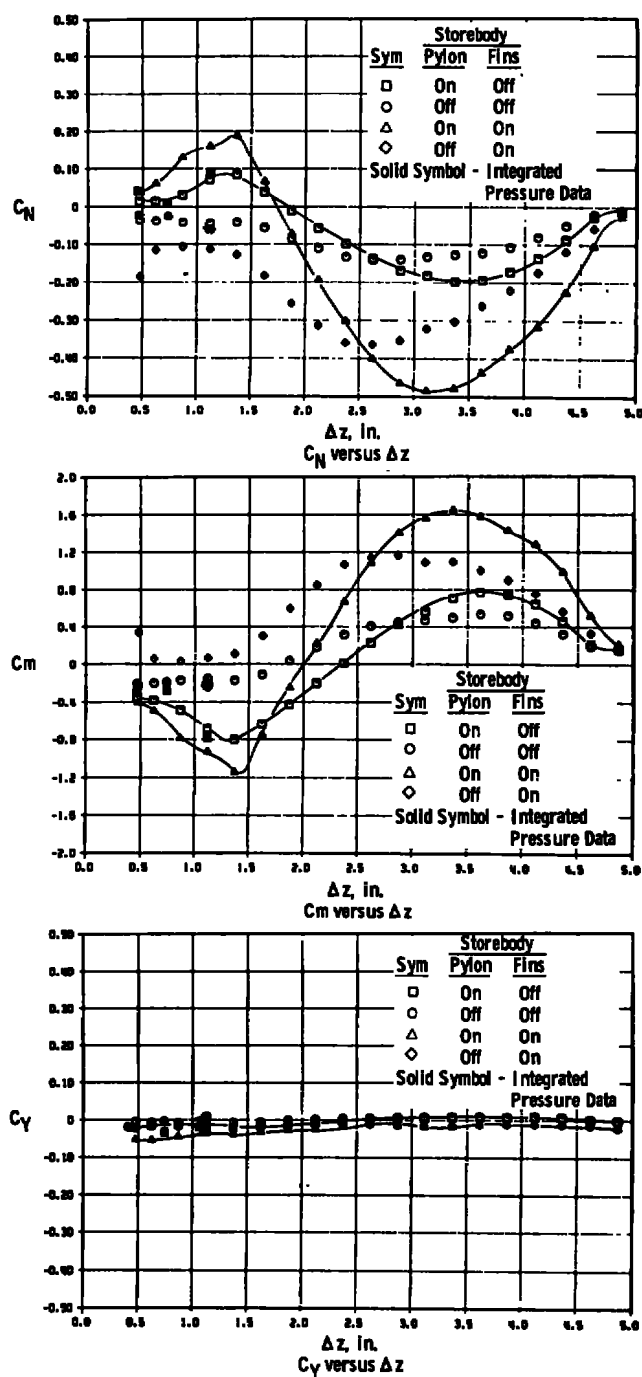
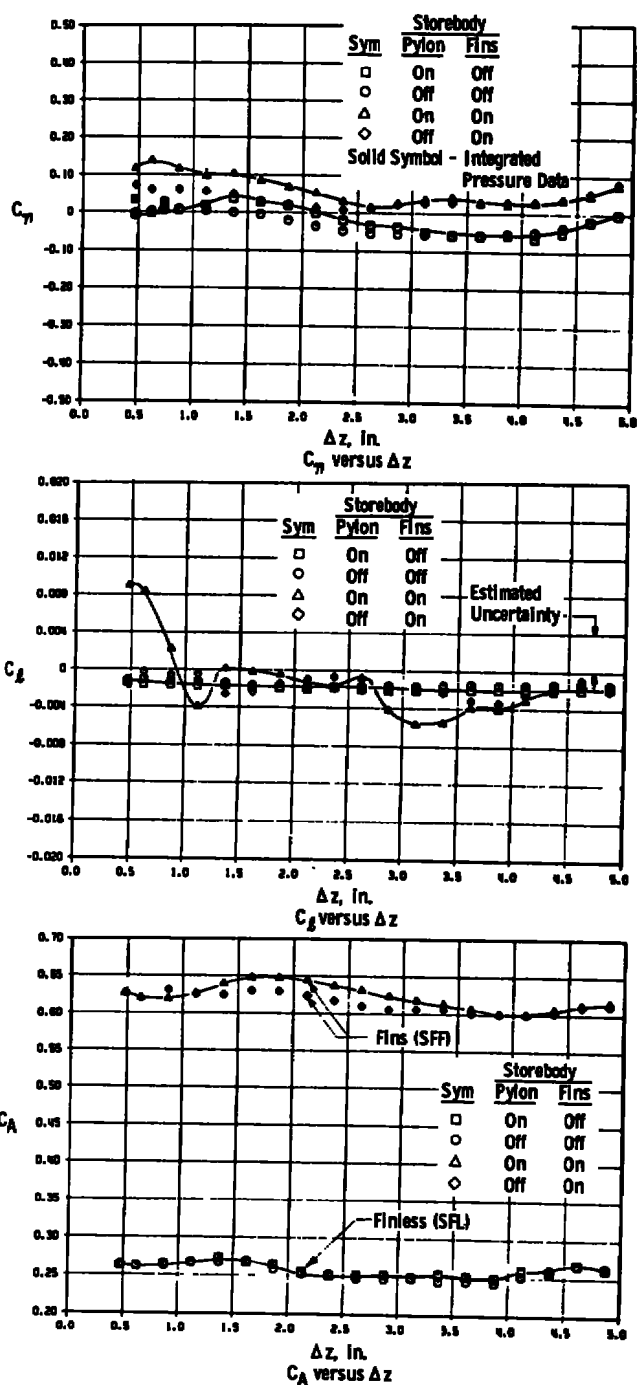


Figure 27. Comparison of force/moment data, integrated surface pressure data, and predicted static stability and axial-force coefficients of the isolated storebody.

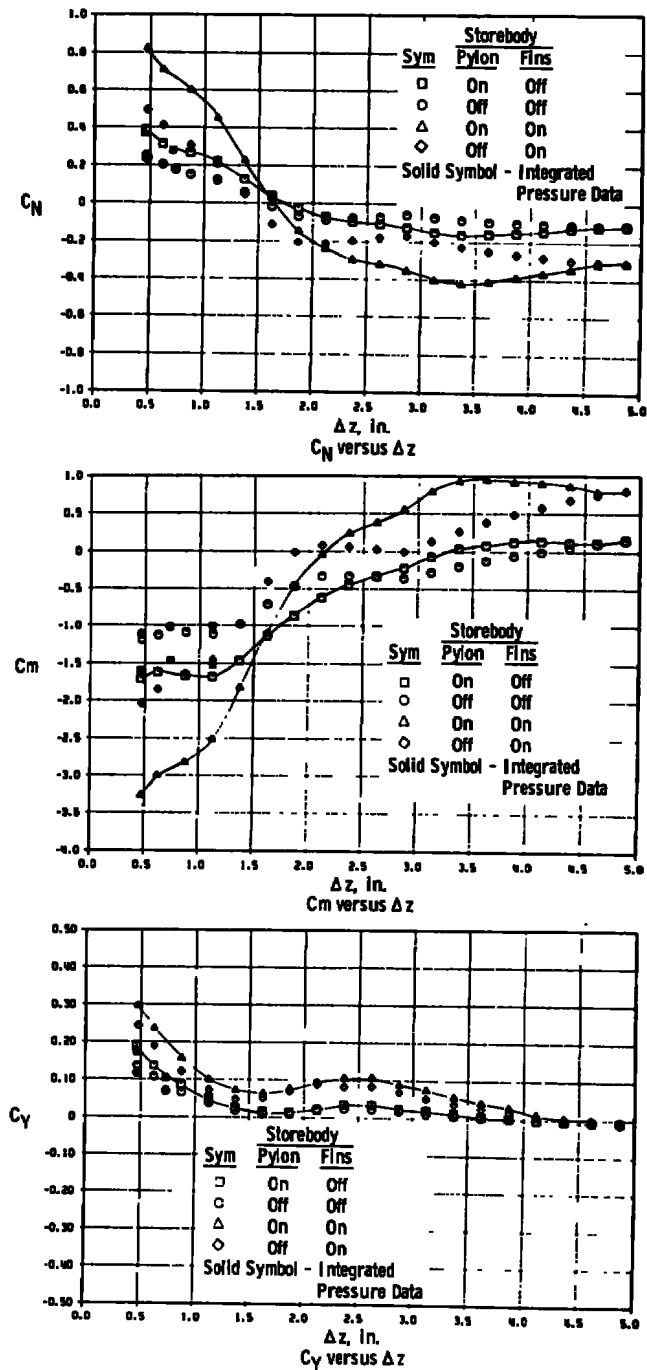


a. Center pylon location, $y = 0$

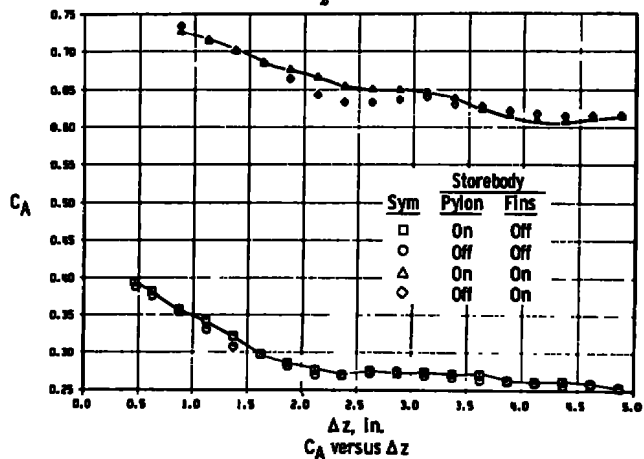
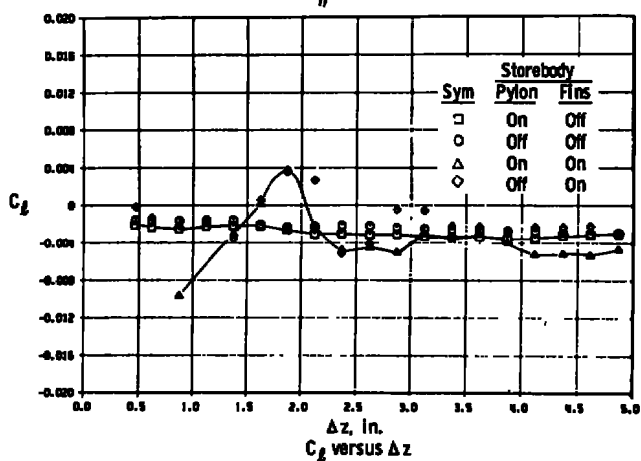
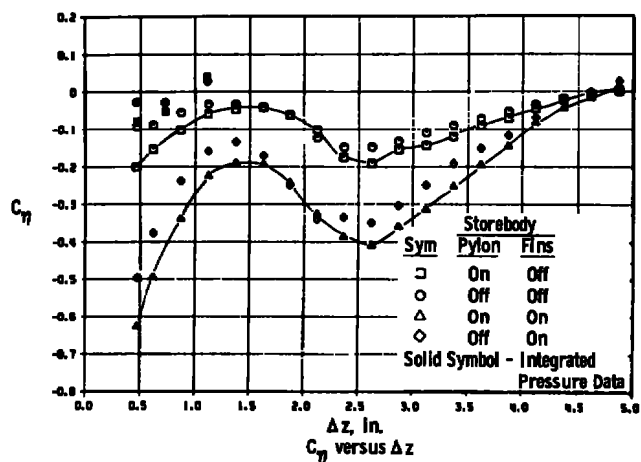
Figure 28. Variation of the storebody static stability coefficients with vertical displacement from the parent body with and without the pylon at $\alpha = 0$, $M_\infty = 1.5$, $Re/ft = 4 \times 10^6$.



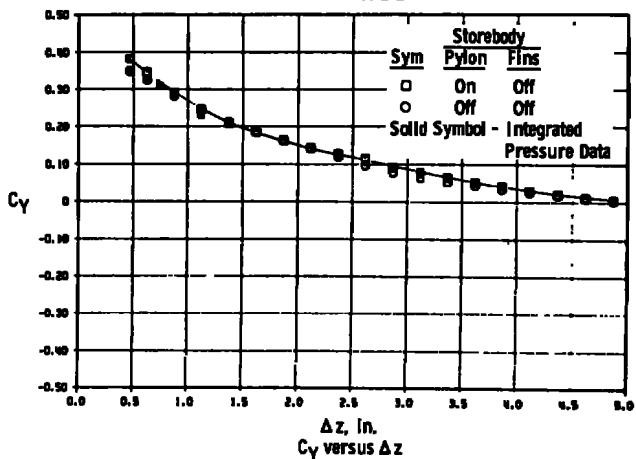
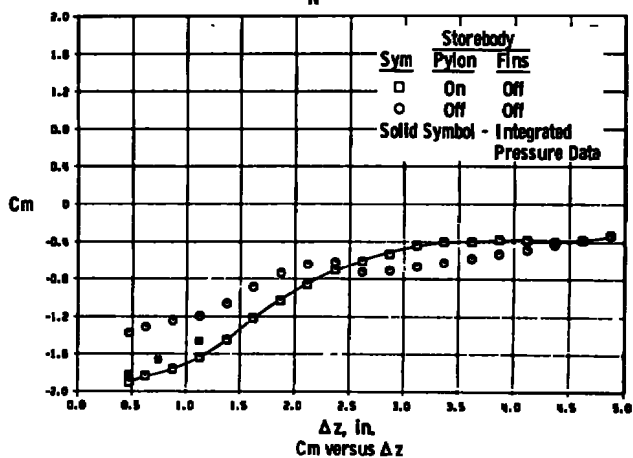
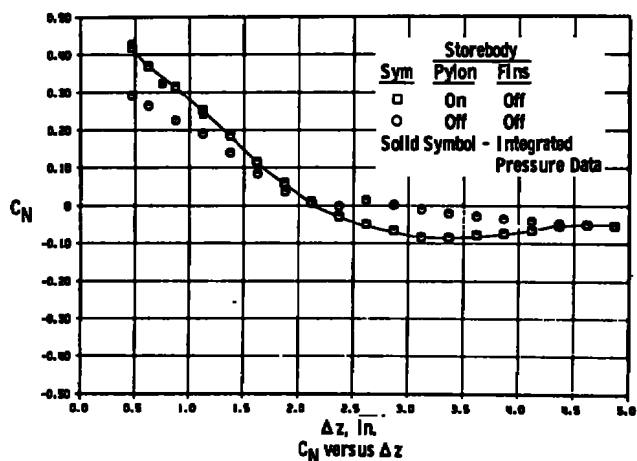
a. Concluded
 Figure 28. Continued.



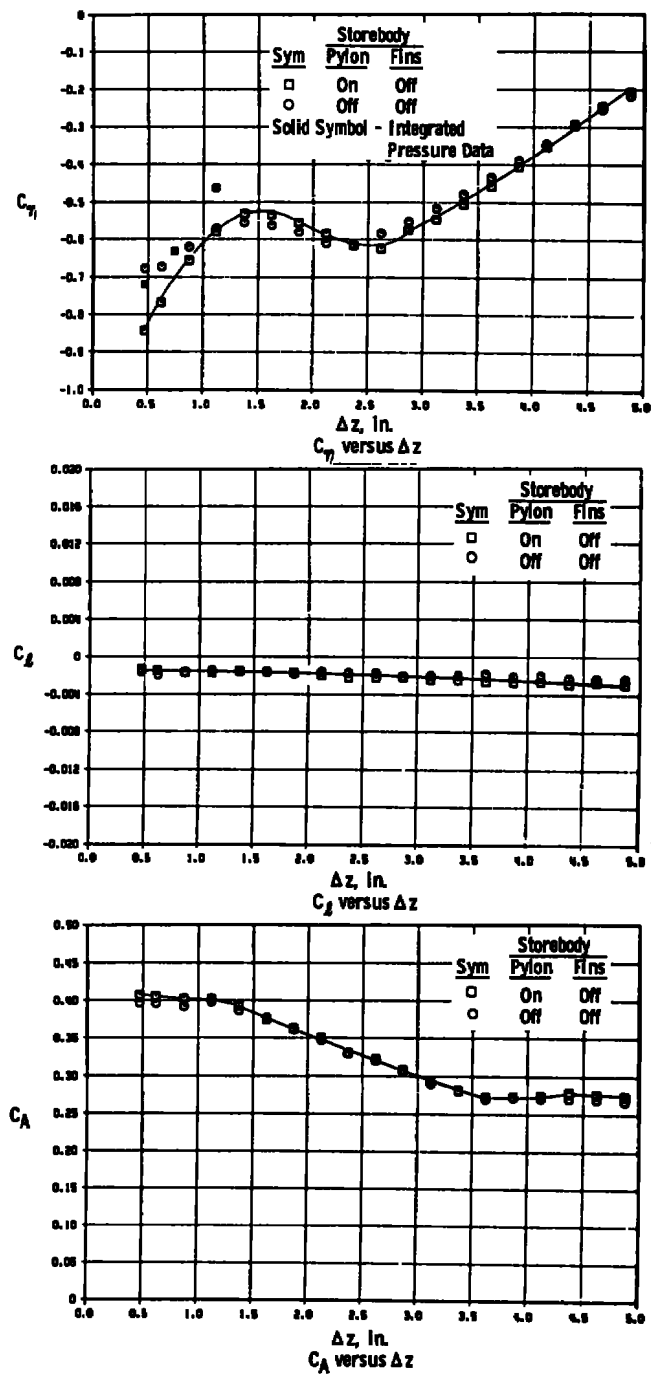
b. 1/3-wing station pylon location, $y = -4.0$ in.
 Figure 28. Continued.



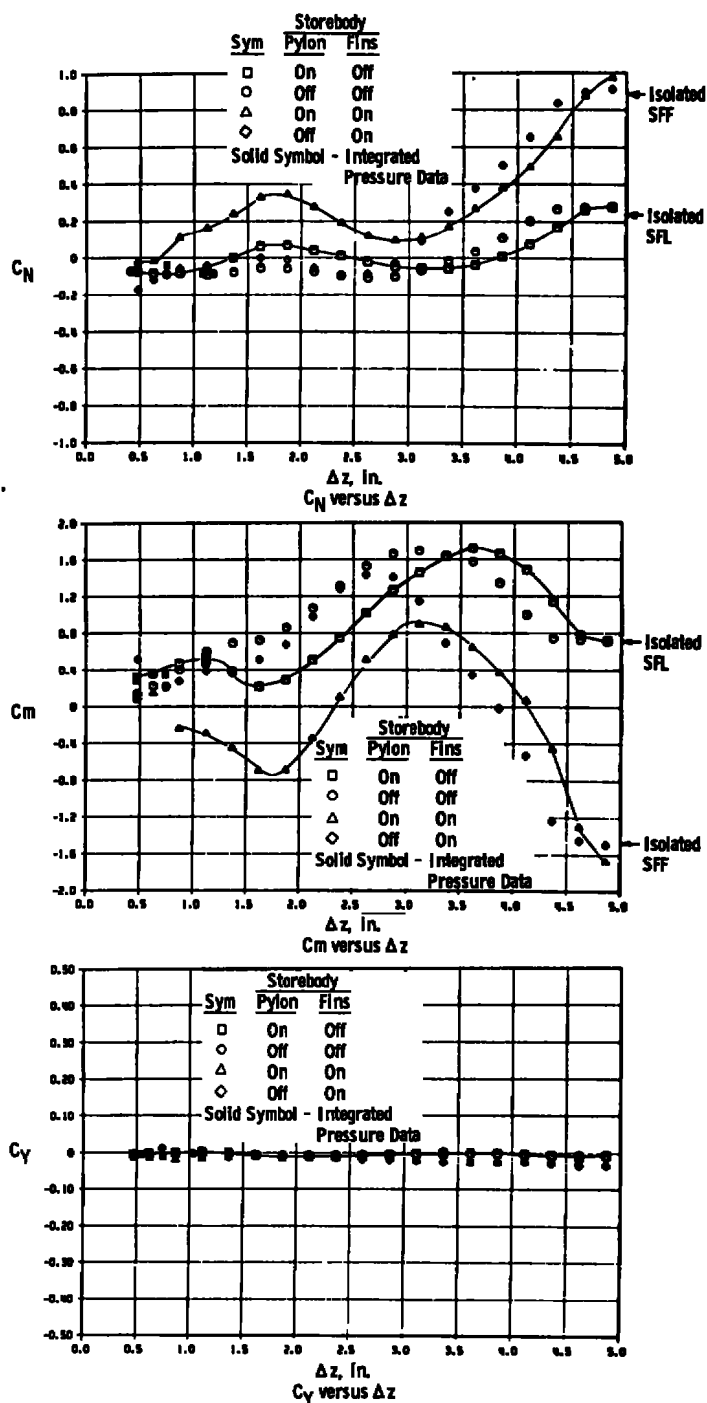
b. Concluded
Figure 28. Continued.



c. 2/3- wing station location, $y = -8.0$ in., $\alpha = 0$
Figure 28. Continued.

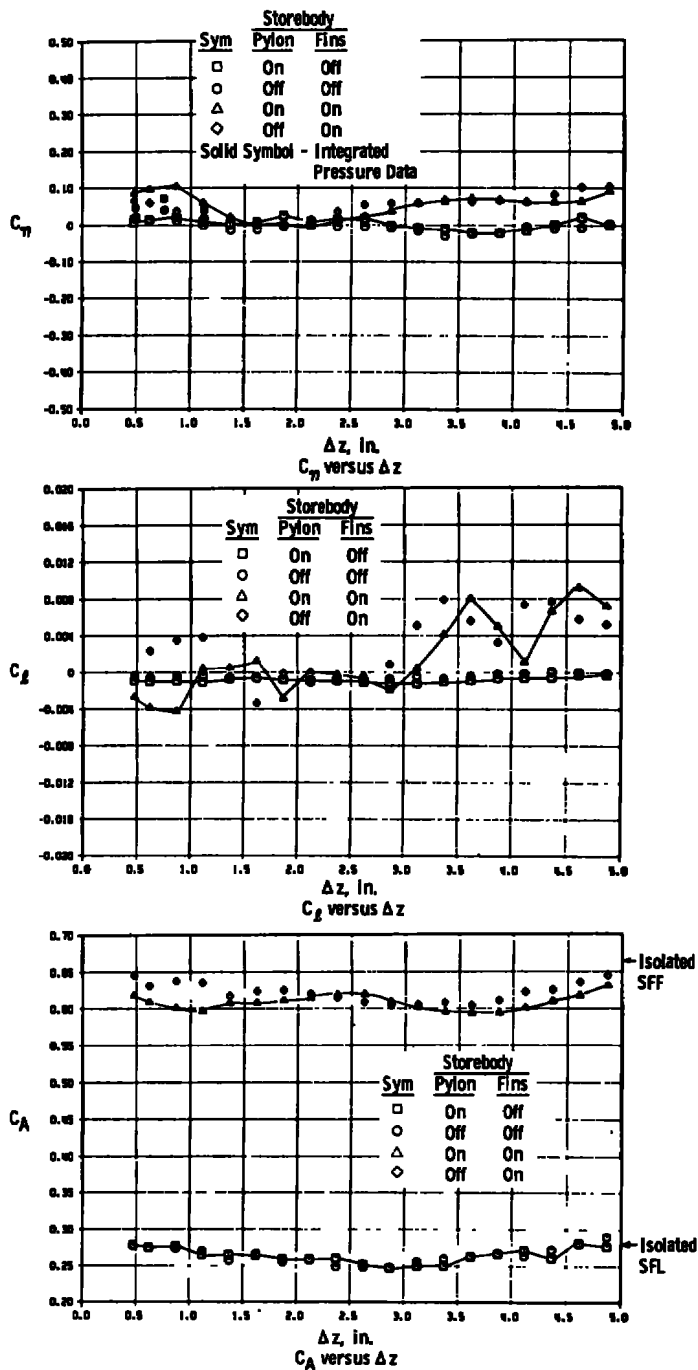


c. Concluded
Figure 28. Concluded.

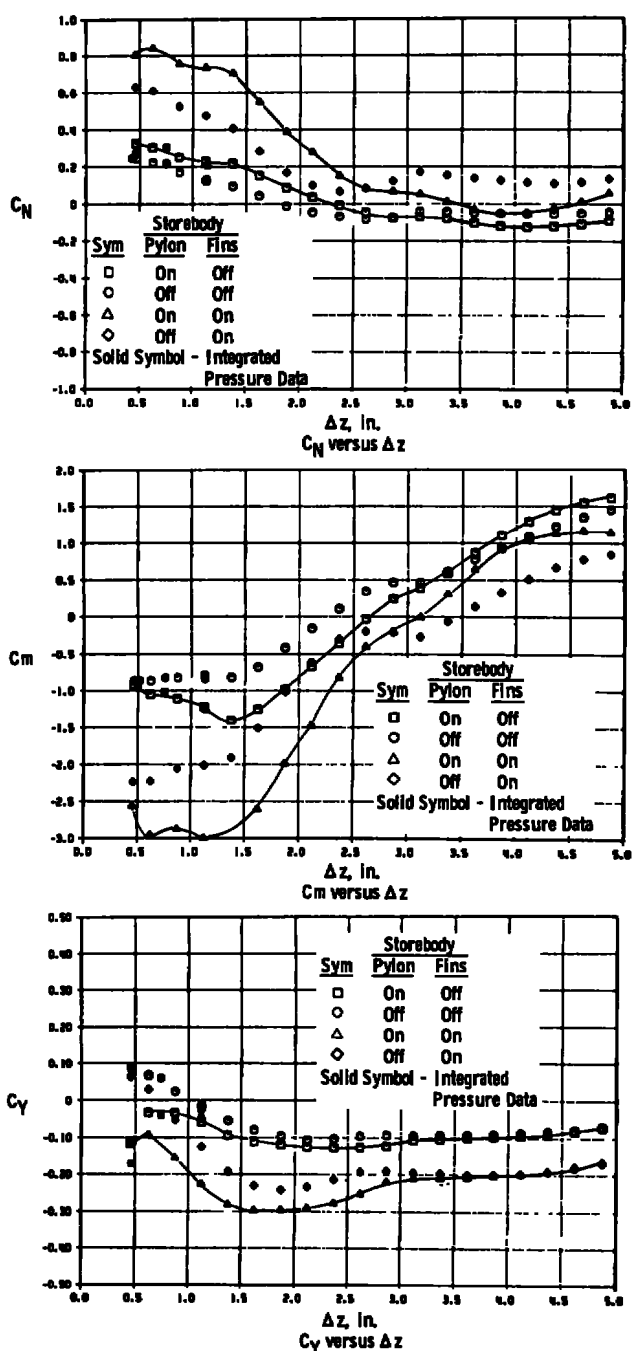


a. Center pylon location, $y = 0$

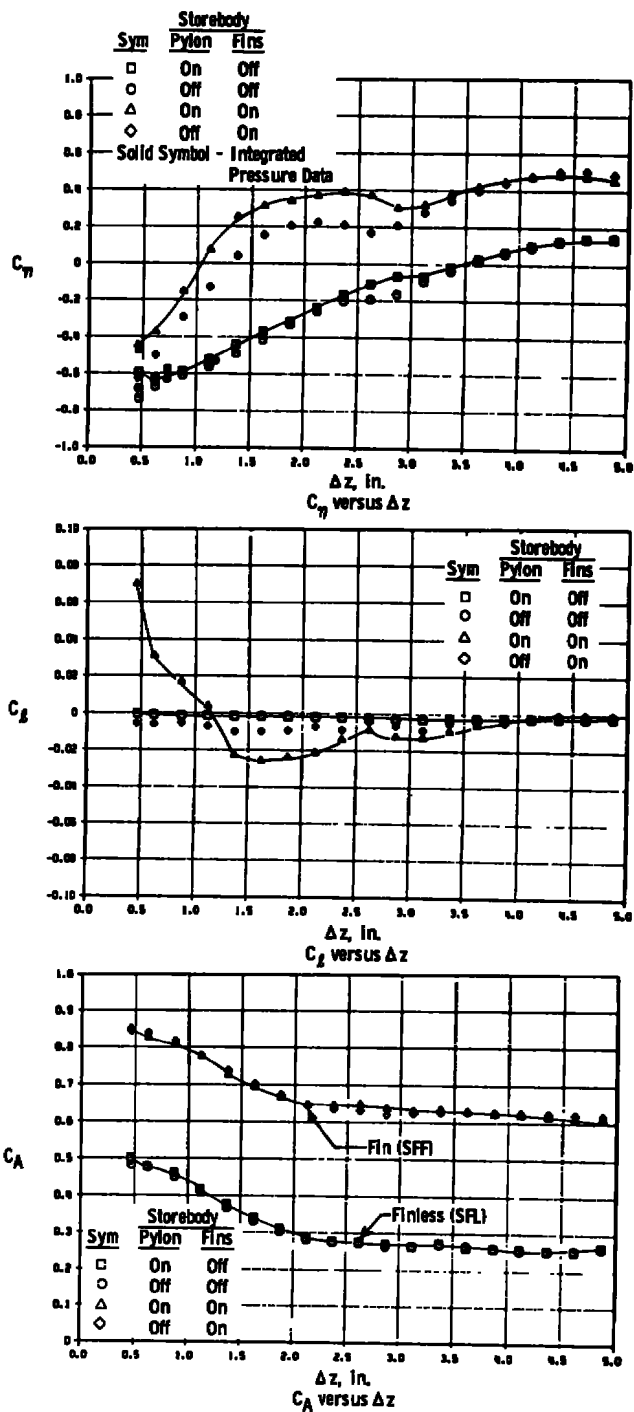
Figure 29. Variation of the storebody static stability coefficients with vertical displacement from the parent body with and without the pylon at $\alpha = 5$ deg, $M_\infty = 1.5$, $Re/ft = 4 \times 10^6$.



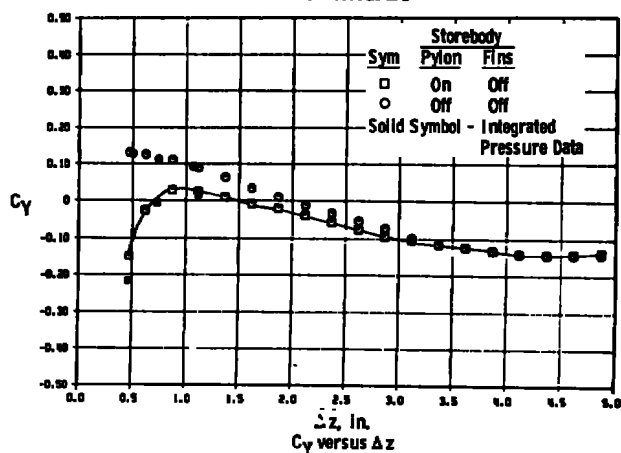
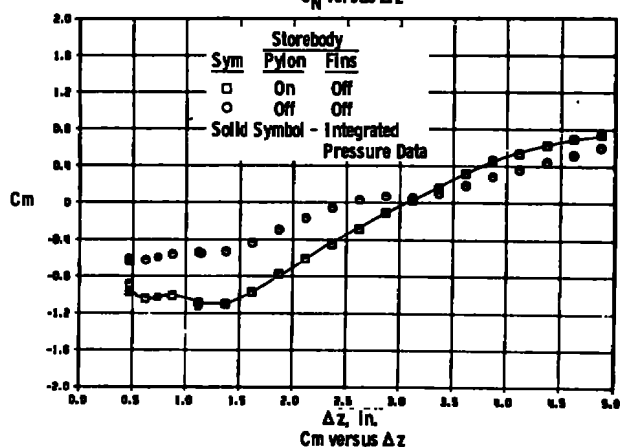
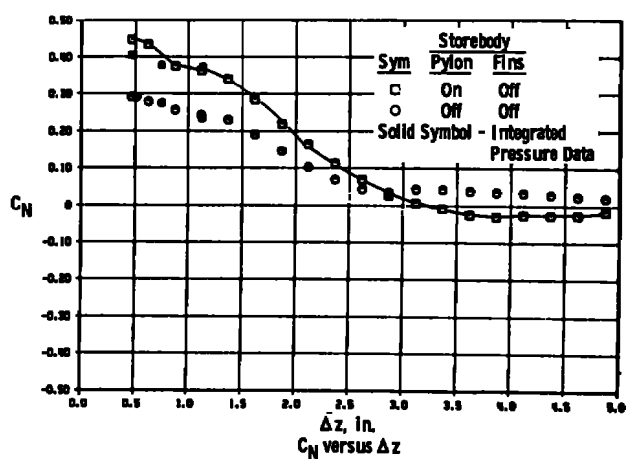
a. Concluded
Figure 29. Continued.



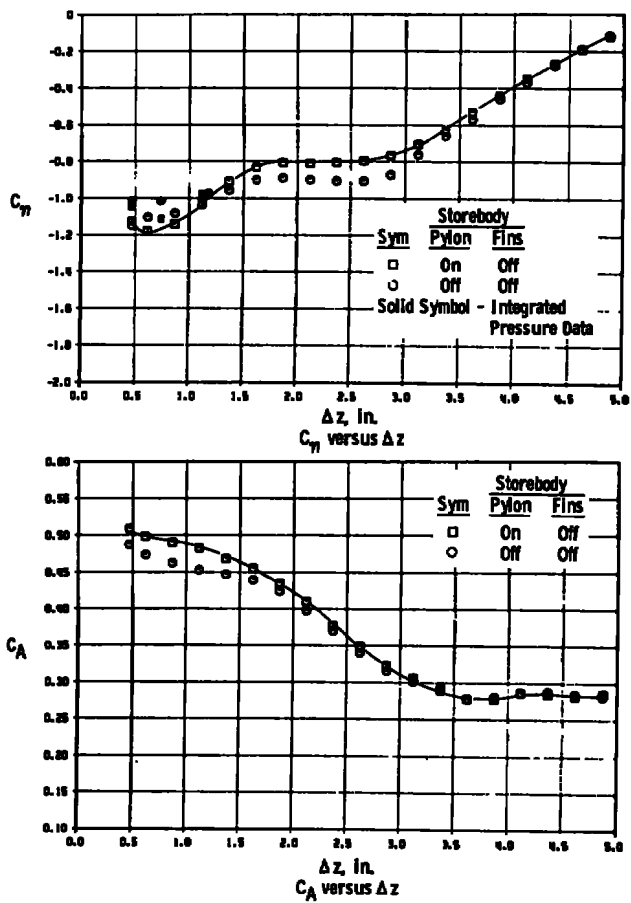
b. 1/3-wing station pylon location, $y = -4.0$ in., $\alpha = 5^\circ$
Figure 29. Continued.



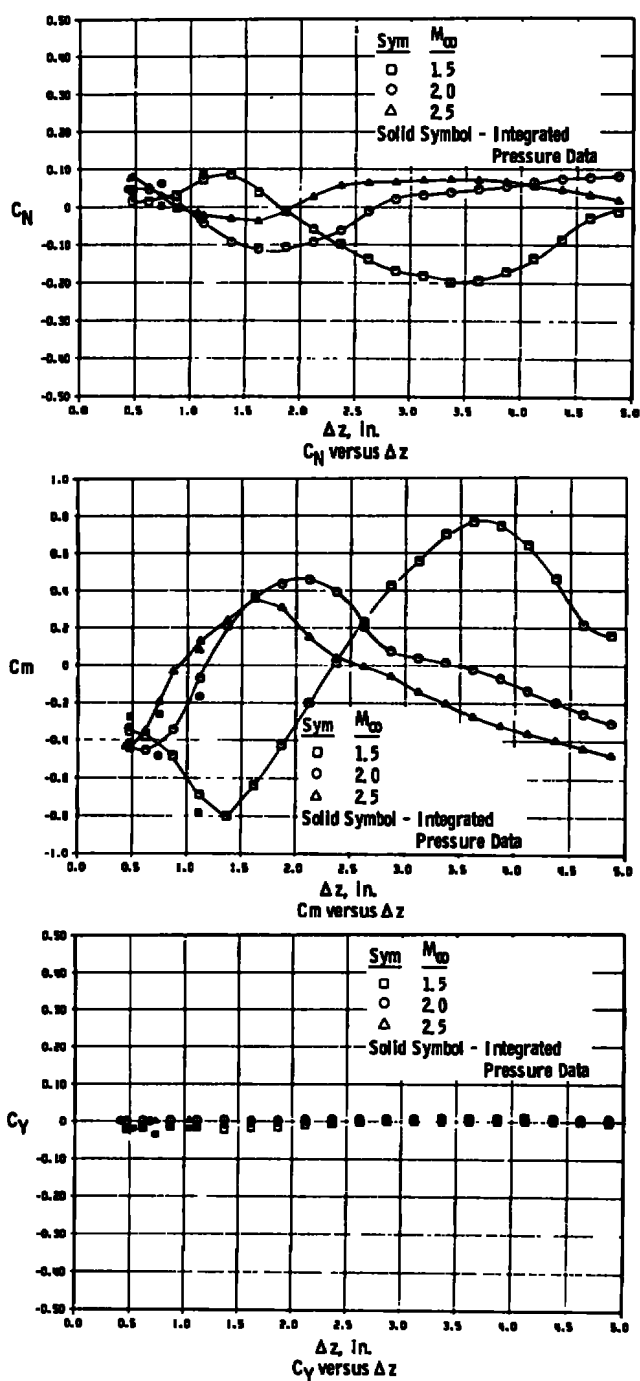
b. Concluded
Figure 29. Continued.



c. 2/3-wing station pylon location, $y = -8.0$ in., $\alpha = 5$ deg
Figure 29. Continued.

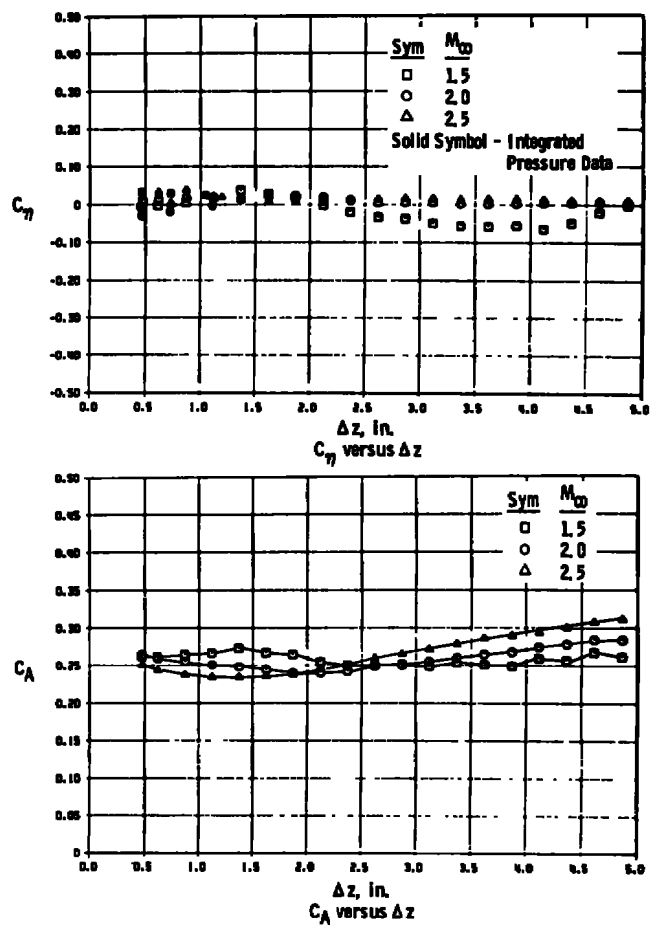


c. Concluded
Figure 29. Concluded.

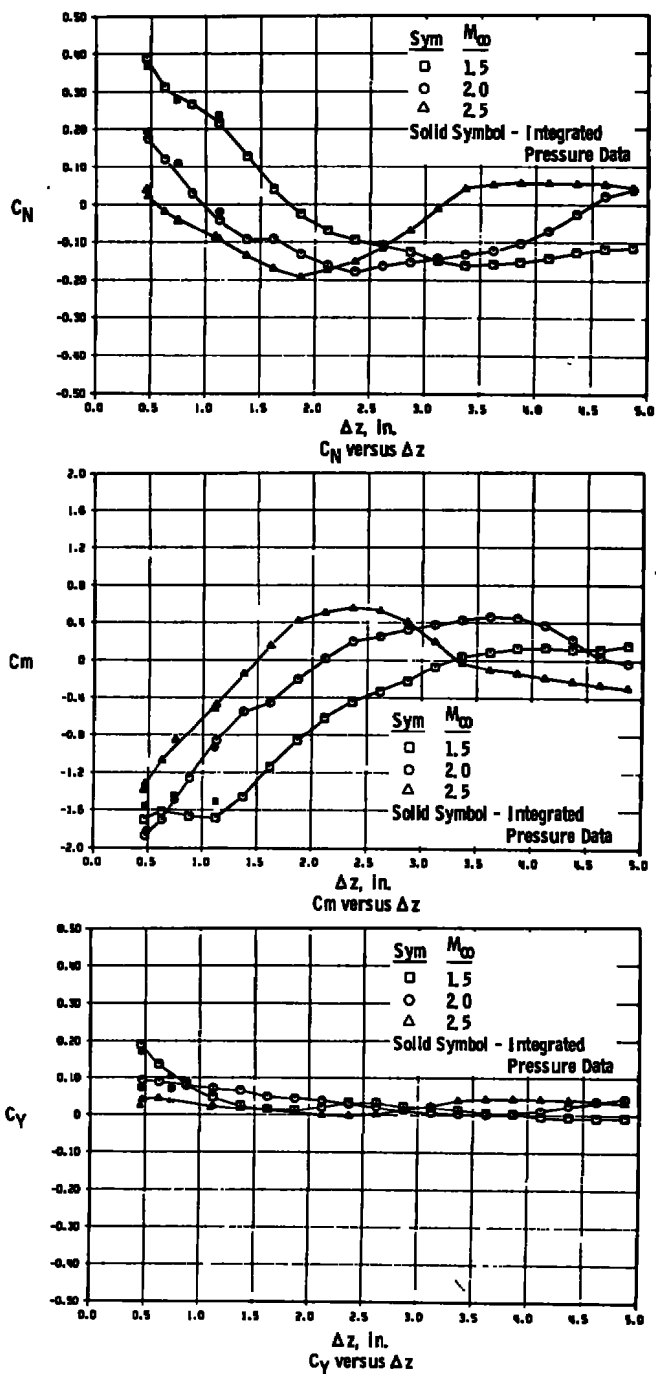


a. Center pylon location, $y = 0$

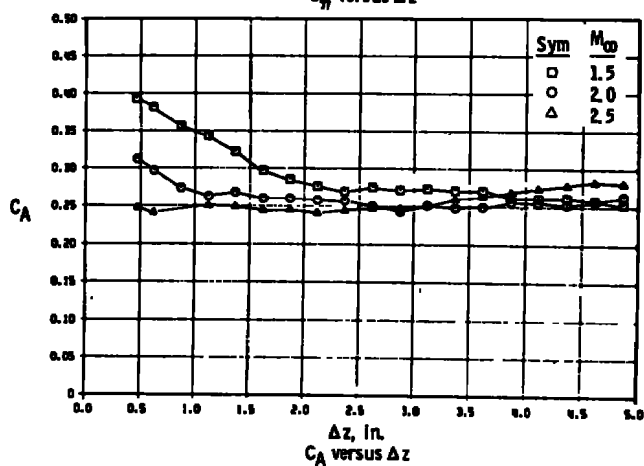
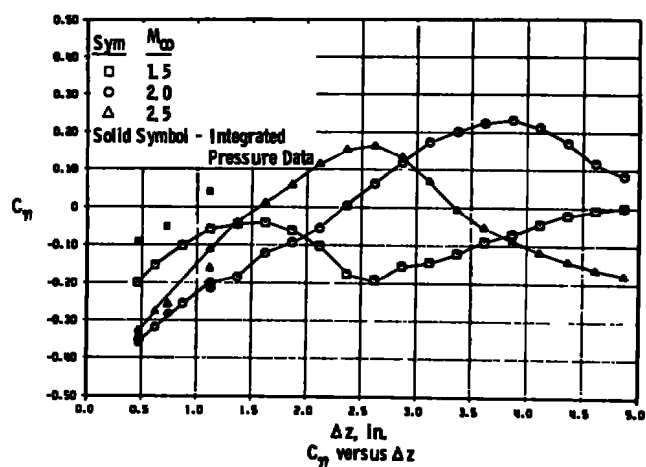
Figure 30. Mach number effects on the variation of the storebody (SLFN) static stability coefficients with vertical displacement from the parent body with the pylon, $a = 0$, $Re/ft = 4 \times 10^6$.



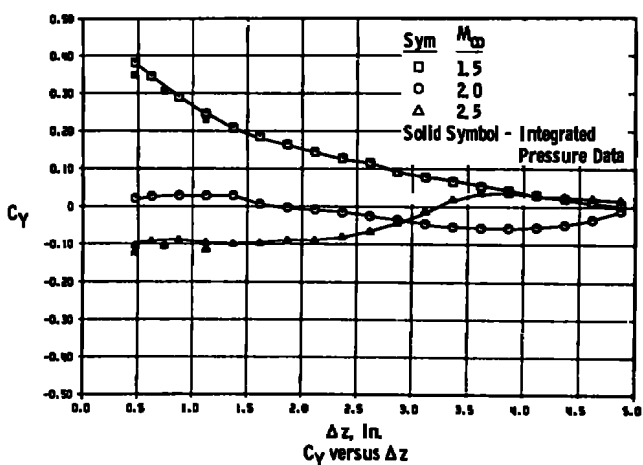
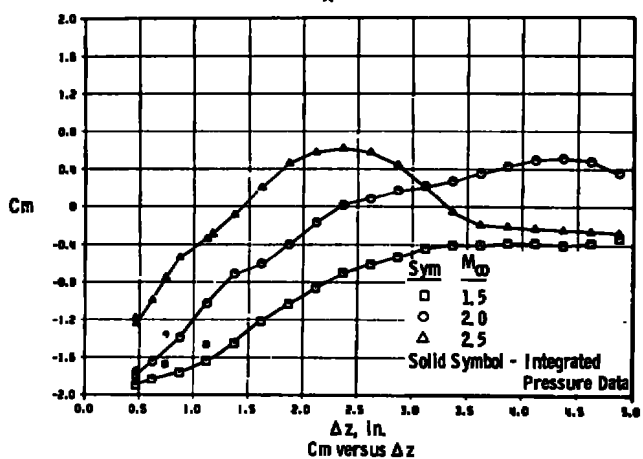
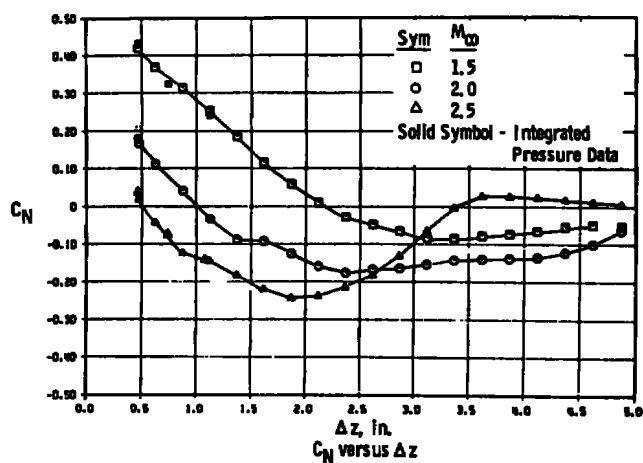
a. Concluded
Figure 30. Continued.



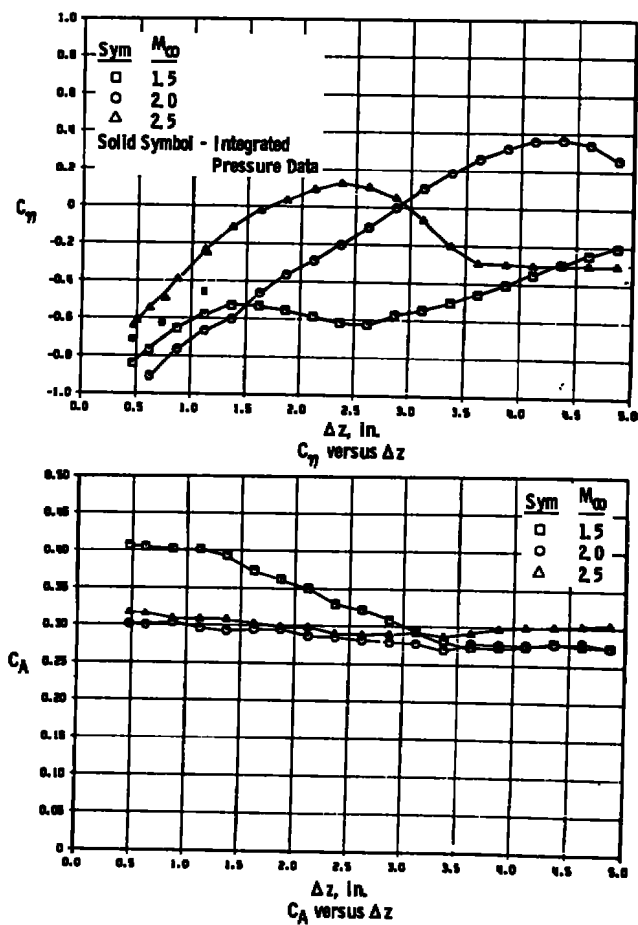
b. 1/3-wing station pylon location, $y = -4.0$ in.
 Figure 30. Continued.



b. Concluded
Figure 30. Continued.



c. 2/3-wing station pylon location, $y = -8.0$ in.
Figure 30. Continued.



c. Concluded
Figure 30. Concluded.

NOMENCLATURE

A_n	Coefficients in Eq. (14) for $M\ell = f(\bar{p}/p'_0)$
C_A	Forebody axial-force coefficient, $C_{AT} - C_{Ab}$
C_{Ab}	Base drag coefficient, $(p_\infty - p_b)/(q_\infty S)$
C_{Ap}	Integrated pressure drag coefficient
C_{AT}	Total (uncorrected) axial-force coefficient, axial force/ $q_\infty S$
C_ℓ	Rolling-moment coefficient about the storebody axis, rolling moment/ $(q_\infty Sd)$
C_m	Pitching-moment coefficient referenced to the midpoint of the storebody, pitching moment/ $(q_\infty Sd)$
$C_{m,a}$	Slope of the pitching-moment coefficient curve at $a = 0$, dC_m/da
C_N	Normal-force coefficient, normal force/ $(q_\infty S)$
$C_{N,a}$	Slope of the pitching-moment coefficient curve at $a = 0$, dC_N/da
C_n	Coefficients in Eq. (22) for $\Delta a = f(\phi)$
C_Y	Side-force coefficient, side force/ $(q_\infty S)$
C_η	Yawing-moment coefficient referenced to the midpoint of the storebody, yawing moment/ $(q_\infty Sd)$
c_A	Local axial-force coefficient per unit length, in.^{-1}
c_m	Local pitching-moment coefficient per unit length, in.^{-1}
c_N	Local normal-force coefficient per unit length, in.^{-1}
c_Y	Local side-force coefficient per unit length, in.^{-1}
c_η	Local yawing-moment coefficient per unit length, in.^{-1}
d	Store base diameter, reference length, 0.75 in.
DPSQ	Parameter, $\sqrt{(\Delta p_{1,3}/\bar{p})^2 + (\Delta p_{2,4}/\bar{p})^2}$

E_n	Coefficient in Eq. (20) for $\eta/\bar{p} = f(M\varrho)$
K	Function, $K = 2/(\gamma\pi M_\infty^2 r_b^2)$
ℓ	Storebody length, 6.375 in.
M	Mach number
p	Pressure, psia
\bar{p}	Average cone surface static pressure, psia
p'_o	Pitot pressure, psia
\bar{P}_o, \bar{P}_2	Second-order perturbation parameters in Eq. (11) for sharp cone surface pressure predictions
q_∞	Free-stream dynamic pressure, psia
Re/ft	Reynolds number per ft
r_b	Storebody base radius, 0.375 in.
r_n	Local storebody radius at "n" model station, in.
S	Storebody base area, reference area, 0.4418 in. ²
S_{LFN}	Finless storebody
S_{LFF}	Finned storebody
T_o	Total (or stilling chamber) temperature, °R
T	Static temperature, °R
U	Resultant velocity component, ft/sec
u, v, w	Velocity components in the x, y, z coordinate directions, respectively, ft/sec
x, y, z	Coordinate system referenced to the parent-body nose, in.
x_s	Storebody axial station referenced to the nose, in.
α	Angle of attack, deg

α_T	Total angle of attack, deg
α_l	Local downwash angle, deg
$\Delta p_{1,3}$	Pressure differential between taps 1 and 3 of the cone probe, $\Delta p_{1,3} = p_1 - p_3$, psia
$\Delta p_{2,4}$	Pressure differential between taps 2 and 4 of the cone probe, $\Delta p_{2,4} = p_2 - p_4$, psia
$\Delta x, \Delta y, \Delta z$	Displacement of the moment reference point of the storebody from the surface of the pylon, in.
$\Delta a_m, \Delta \psi_m$	Estimated misalignment in pitch and yaw respectively of cone probes, deg
$\Delta a(\text{DPSQ})$	Flow-field angle correction due to nonlinearity, deg
$\Delta a(\phi)$	Flow-field angle correction based on total roll angle sensed by cone probes, deg
δ_n	Local slope of storebody contour, deg
η	Linearity factor for flow-field angle evaluations, i.e., $\frac{\eta}{p} = (1/2)d(\text{DPSQ})/d\alpha_T$ per deg
γ	Specific heat ratio
σ_l	Local sidewash angle, deg
ϕ	Roll angle, deg
ϕ_n	Roll position of the n^{th} pressure tap on cone probes, deg
θ	Cone probe half angle, $\theta = 20$ deg
ψ	Yaw angle, deg

SUBSCRIPTS

l	Local stream property
n	n^{th} pressure tap
o	Stilling chamber or total stream property
∞	Free-stream property